X-ray Imaging Spectroscopy of the Galactic Center Region

Yoshitomo MAEDA

Department of Physics. Graduated School of Science,

Kyoto University, Sakyo-ku, Kyoto 606-8502, Japan

Submitted to the Department of Physics,

Kyoto University on January 5, 1998,

in partial fulfillment of the requirements for

the degree of Doctor of Philosophy

Abstract

We present the *ASCA* results of the first high quality X-ray images and spectra of the Galactic Center in the wide X-ray band of 0.7 - 10 keV. We found a new X-ray source AX J1745.6−2901 about $1'.3$ south-west from the nuclear supermassive black hole candidate Sgr A*. We discovered a type-I X-ray burst and eclipses from AX J1745.6−2901, hence established AX J1745.6−2901 to be an eclipsing low-mass X-ray binary. Excess soft X-rays during the eclipse were detected, which is well explained by the scattering process of interstellar dust-grains.

From the entire ∼1 square degree field near the Galactic Center, we found a diffuse emission with K-shell transition lines from highly ionized elements (silicon, sulfur, argon, calcium: here "the lighter elements"), in addition to that of highly ionized iron, which has been previously reported. The Kα flux from highly ionized iron is symmetrically extended along the Galactic plane, while those of the lighter elements are more irregularly distributed, both with the peaks at a few arcmin-radius region near Sgr A*.

Kα lines from neutral or low ionized iron are also found from molecular clouds. The morphology, spectrum and iron line flux are fully consistent with reflected X-rays from the cold molecular clouds, but we found no apparent bright source to irradiate the clouds.

The presence of the Kα line from highly ionized iron gives firm evidence for a diffuse high-temperature plasma of $kT \cong 10$ keV, while those of the lighter elements indicate the presence of much less temperature plasma of ∼1 keV.

The X-rays in the brightest region near Sgr A* would come from a hot gas filling the interstellar space with the thermal energy of about 2×10^{50} erg.

In the entire ∼1 square degree field, the lower temperature plasma is interpreted to be attributable to a superposition of 10^{1-2} supernova remnants, while the origin of the higher temperature plasma is more debatable.

The higher temperature plasma with the total kinetic energy as large as 10^{54} ergs, may come from a diffuse hot gas. We suggest that the Galactic center exhibited intermittent activities with a time-averaged energy generation rate ($\sim 10^{41-42}$ erg s^{-1}) comparable to the Seyfert nuclei, a class of active galactic nuclei. The intermittent activity is also one possibility to explain the reflected X-rays with no apparent irradiating sources; the clouds has been irradiated by X-rays from the Galactic center which was bright in the past but is dim at present.

A superposition of faint discrete sources such as 10^5 of cataclysmic variables (CV), would be another possibility. This requires an extremely high density of CVs near the center, and also predicts a high rate of type-Ia supernova explosion.

We also carried out the Chris-cross mapping up to 10 degree around the Galactic Center with *ASCA* and detected the Galactic bulge and ridge emissions around the Galactic Center but with much reduced flux level. The observed Galactic ridge spectra often show the Kα-lines from highly-ionized silicon, sulfur, argon, calcium, and iron. The bulge emission shows a high emissivity for the silicon Kα-line, which may be another remain of the past activities in the Galactic Center.

Contents

1 Introduction & Review **6**

1.1 Introduction 6

1.2 Review of the High Energy Phenomena near the Galactic Center . . 7

1.2.1 The Nuclear Supermassive Black Hole Candidate Sgr A* and its Close Vicinity 7

1.2.2 X-ray Emission near the Galactic Center 9

1.2.3 Large-Scale Diffuse X-ray Emission in the Galaxy 11

1.2.4 Galactic Diffuse γ-ray Emission 14

2 Instrument **23**

2.1 *ASCA* 23

2.1.1 XRT 24

2.1.2 GIS 28

2.1.3 SIS 34

3 Observations **42**

3.1 Operation Mode 42

3.1.1 GIS Modes 42

3.1.2 SIS Modes 43

3.2 Mapping of the Galactic Center Region 43

3.3 Large-Scale Mapping around the Galactic Center Region 43

3.3.1 On-Plane 43

3.3.2 Off-Plane 44

3.4 Monitoring Observations of the Galactic Center Sgr A 44

4 Mapping of the Galactic Center Region **52**

4.1 Introduction 52

4.2 Analysis & Results 53
4.2.1 Broad Energy-Band Maps 53
4.2.2 Averaged Diffuse X-ray Spectrum 54
4.2.3 Line Distributions 55
4.2.4 Narrow Energy-Band Maps 55
4.2.5 Sgr B2 56

5 Large-Scale Mapping around the Galactic Center 69
5.1 Introduction 69
5.2 GIS Images & Findings of Discrete Sources 70
5.3 Diffuse X-ray Spectra 71
5.4 Line Distributions 73
5.4.1 Iron-Broad-Line Model 74
5.4.2 Double Iron-Line Model 75
5.4.3 Kα-lines of Magnesium, Silicon, Sulphur, Argon and Calcium 76
5.5 Correlations of Flux-Ratios 93

6 Monitoring Observations of the Galactic Center Sgr A 98
6.1 Introduction 98
6.2 Data Screening and Correction 99
6.2.1 The GIS Data for the '93 Autumn & '94 Autumn Observations 99
6.2.2 The SIS Data for the '93 Autumn & '94 Autumn Observations 100
6.2.3 The GIS Data for the '97 Spring Observations 100
6.2.4 The SIS Data for the '97 Spring Observations 101
6.3 Images Near the Galactic Center 101
6.3.1 The GIS Images 101
6.3.2 The SIS Images 102
6.4 The Hard Source (AX J1745.6−2901) 107
6.4.1 Variability of the Hard Source 107
6.4.2 X-Ray Fluxes and Spectra 109
6.4.3 The Burst Spectrum 111
6.4.4 Discussion 111
6.5 The Soft Source (Bright Region around Sgr A*) 124
6.5.1 Time Variability 124

6.5.2 Flux and Spectra 124
6.5.3 The '93 Autumn SIS Spectrum 125
6.5.4 The Flux & Spectral Shape of the Three Observations . . . 126

7 Discussion **132**
7.1 Brief Summary of Observational Results 132
7.1.1 Classification of the Diffuse X-ray Emission 134
7.2 The Galactic Center Emission 134
7.2.1 The Galactic Center Plasma 134
7.2.2 The X-ray Reflection Nebula 142
7.3 Present Activities of the Galactic Center Sgr A* 145
7.4 The Galactic Ridge Emission 147
7.4.1 Origin of the Galactic Bulge Emission 149

A SIS Background Spectrum for the Diffuse X-ray Emission **150**

B GIS Background Spectrum for the Diffuse X-ray Emission **152**

C K-lines Obtained by GIS **154**

D Radiation Damage of SIS **161**
D.1 RDD Defect 161
D.2 Selection Criteria of the Frame Data 161
D.3 Result of the RDD Correction 162
D.3.1 Grade & Spectra 163
D.4 Systematic Errors of the Detection-Efficiency 163

E Radio Map of the Molecular Clouds **168**

Chapter 1

Introduction & Review

1.1 Introduction

The center of our Galaxy (here the Galactic Center, or GC in short) is the nearest center of all the galaxies[1]. In spite of its vicinity, the Galactic Center has been poorly understood, due mainly to a large optical extinction of $\sim$30 mag through the Galactic disk from the Sun to GC. The radio and infrared radiation with wavelength $\lambda \geq 2\ \mu m$ and X- and γ-rays with energy $E \geq 2$ keV can penetrate the interstellar medium. With these wavelengths, our understanding of the Galactic Center has largely developed in the last a few ten years.

The Galactic Center has been found to show high concentration of gas and stars, which may activate star formations and supernova explosions. The Galactic Center also has drawn much attention, particularly in connection with possible presence of a supermassive black hole. The radio and infrared observations have revealed highly complex features in the close vicinity of the Galactic center, and indicated a large mass concentration of the order of million solar masses within less than 0.2 pc from the Galactic center.

In spite of extensive observations at these wavelengths, only one or a few supernova remnants were directly detected in the Galactic Center region. Direct evidence for high-energy activities of the Galactic center, such observed in active galactic nuclei (AGN), is still lacking.

Supernova remnants and active galactic nuclei were found to radiate a large fraction of their energy in the X-ray band (e.q. [30]; [106] for *ASCA* results). The

[1]throughout this thesis, we assume that the distance to the Galactic center is 8.5 kpc.

Japanese X-ray satellite *ASCA* images high energy X-rays up to 10keV with superior energy resolution, hence can largely contribute to our understanding of high energy phenomena at the Galactic Center through the dusty interstellar medium.

We reviews the high energy phenomena in the Galactic Center region in the next session. In chapter 2, we report on the *ASCA* satellite and its instruments onboard *ASCA*. In chapter 3, we summarize a series of our *ASCA* observations of the Galactic Center region. In chapter 4–6, we report the results for the data-analysis of these observations. In chapter 7, We discussed these results.

1.2 Review of the High Energy Phenomena near the Galactic Center

The Galactic Center exhibits a wide variety of phenomena from the stellar to Galactic scales. Therefore, many review papers on the Galactic Center research are found: [81]; [12]; [25]; [10]; [24]; [74]. In this thesis, we concentrate on several topics closely related to the high energy phenomena near the Galactic Center. Other topics can be found in the six review papers and reference therein.

1.2.1 The Nuclear Supermassive Black Hole Candidate Sgr A* and its Close Vicinity

The Galactic center region "Sgr A", which lies in the innermost $\sim$1 pc radius region, is strong emitter at the radio wavelength. It consists of three parts; Sgr A East, Sgr A West and Sgr A* ([25] and reference therein). Sgr A East is a non-thermal, shell-like source and is considered to be a shock surface by, for example, a young supernova remnant. Sgr A West shows a mini-spiral morphology (figure 1.1) and has a thermal spectrum in the radio wavelength. Eckart et al. (1993 [18]) reported deep 1.6 and 2.2μm images of the central parsec of the Galactic Center with a high resolution of 0.15 arcsec. They found about 340 giants and a few tens of massive stars within 0.1 pc. Sgr A West is then believed to be a giant HII region ionized by these stars. The non-thermal radio compact source Sgr A* at the center of Sgr A West is believed to a dynamical center of our Galaxy, hence is the Galactic Center.

Circumnuclear Cold and Warm Materials (Disk/Torus?)

The molecular medium extends only to within about 1.5 pc of the center (circumnuclear disk: CND). We show a HCN $J = 1 \rightarrow 0$ map at $3''$ resolution ([116]) in figure 1.1. The inner edge of CND presents a rather sharply defined ionized boundary layer, produced by the radiation from the encircled stellar cluster. The CND shows velocities as high as ± 100 km s^{-1} (figure 1.2). Circular rotation ($V_{\rm rot} \sim$ 130 km s^{-1} at the radius of ~ 6 pc) provides kinematics of the CND. Most of the kinematic models yield two values of radial velocities, more likely value of ($\leq$ 20 km s^{-1}) , and less plausible, but is not rejected, value of ($\leq$ 50 km s^{-1}).

In order for the photons from the GC to propagate outward to the inner boundary of CND, the inner region of CND (the central cavity near GC) must be comparatively transparent ([9]).

In the innermost 1.5 pc radius region, the distribution of ionized gas is complicated as is evidenced by the Ne^+ 12.8 μm image in figure 1.3. The ionized gas shows velocities as high as ± 300 km s^{-1}, with pronounced velocity gradients in the central 10 arcsec. For several of the inner filaments, eccentric orbits in the field of a point mass reproduce the gas velocities well under the assumption of the gas flow along the filaments. However, the Eastern Arm and a portion of the innermost Bar feature (figure 1.3) have velocity patterns consistent with orbital trajectories transiting the central 0.5 pc. Both of these filaments are likely to be the result of dense gas plunging into the central cavity from the CND or beyond.

Enclosed Dark Mass (Central Engine?)

Mass distribution in the central 100 pc was systematically studied through the three approach by Genzel & Townes (1987 [25]). First, they converted the stellar surface brightness distribution to a mass distribution assuming a constant mass-to-luminosity ratio. Second, they converted the velocities of interstellar gas clouds to the mass distribution assuming the simple orbits of the gas clouds. Third, they determined the mass distribution from statistics of the stellar velocities assuming that the stellar distribution has a relatively simple symmetry (such as spherical or spheroidal). The enclosed mass distribution derived with these three approaches is shown in figure 1.4. The deviation from the dashed lines inside a radius of 1 pc in figure 1.4 indicates the presence of a dark mass of 1 to 3×10^6 $M_\odot$.

Recently Eckart & Genzel (1997 [19]) determined proper motions for 39 stars between 0.03 and 0.3 pc from the compact radio source Sgr A*. They found that proper motion and radial velocity dispersions are in very good agreement, indicating that the stellar velocity field on average is close to isotropic. Taking radial and proper motion data together the dynamic evidence, they derived the central dark mass of a $2.45(\pm 0.4) \times 10^6$ $M_\odot$ located within 0.015 pc of Sgr A* at the distance of 8 kpc. Its mass density is then at least 6.5×10^9 $M_\odot$ pc^{-3}, excluding the fact that the central mass concentration is in form of a compact white dwarf or neutron star cluster. In addition, they detected significant changes in the structure of the innermost complex of stars in the immediate vicinity of Sgr A*, implying in at least one case stellar motions of ≥ 1500 km s^{-1} within $\sim$0.01 pc of the compact radio source. Including this preliminary evidence, they inferred that the density of the central dark mass would then have to be in excess of 10^{12} $M_\odot$ pc^{-3}, implying that the central mass concentration is probably a single supermassive black hole.

1.2.2 X-ray Emission near the Galactic Center

X-ray observations of the Galactic Center region were carried out with very early rocket and balloon instruments, but detailed observations started with the *Uhuru* satellite in 1971. The *Uhuru* satellite performed scanning observations with an angular resolution of $0.5^\circ \times 5^\circ$. It was detected the extended X-rays of about 2° extent centered on the Galactic center, which was named as U 1743−29 or GC X ([46]). This X-rays were consistent with either an extended source or a complex of at least three sources.

Subsequent satellite and rocket experiments with somewhat better angular resolution established the presence of a number of point sources within the *Uhuru* source region ([21]; [114]; [55]; [15]; [87]). For example, the *Ariel* 5 has detected a point source A 1742−294 ($L_{2-10\mathrm{keV}} = 2.5 \times 10^{36}$ erg s^{-1} at 8.5 kpc). Syunyaev et al. (1991 [100]) observed A 1742−294 with ART-P/*Granat*. They detected type-I X-ray bursts from A 1742−294. A 1742−294 was then identified with the neutron star binary. Eyles et al. (1975 [21]) detected the X-ray outburst from the transient source A 1742−289 about $2'$ far from the Galactic center. The spectrum shape of A 1742−289 was the power-law whose index was about -3, with large absorption N_H approximately 2×10^{23} H cm^{-2}. Eyles et al. (1975 [21]) estimated $L_{3-10\mathrm{keV}}$

$= 4 \times 10^{38}$ erg s^{-1} corrected at 8.5kpc. The *Ariel* 5 and the *SL* 1501 detected the transient source GX +0.2 −0.2.([87]; [15])

In 1979, Watson et al. (1981 [112]) carried out the pointing observations using the *Einstein* IPC placed on the first imaging instrument, the soft X-ray mirror ($0.5 - 4.5$ keV), which had the angular resolution about $1'$. In the radius $30'$ near Sgr A, twelve point-like X-ray sources were detected, for example 1E 1743.1−2843. The local extended structure ($25' \times 15'$ centered about 5 to $10'$ north-east of Sgr A*) and the large extended emission ($33' \times 18'$) were detected. The point source 1E 1742.5−2859 lied at Sgr A West. The luminosity of 1E 1742.5−2859 is 1.1×10^{35} erg s^{-1} (0.5–4.5 keV) assuming $kT = 5$ keV and $N_{\rm H} = 6 \times 10^{22}$ H cm^{-2} at 8.5 kpc.

The *SPARTAN*-1 mission observed the Galactic Center region with collimated proportional counters ($5' \times 3^\circ$) by scanning in six directions ([45]). The images are constructed by a maximum entropy method in the 2–10 keV energy band. The new faint sources GC NE and GC SE were discovered, while 1E 1742.5−2859 was not detected. The upper limit of the luminosity of 1E 1742.5−2859 was 3×10^{34} erg s^{-1} (2–10 keV) at 8.5 kpc. Kawai et al. (1988 [45]) estimated that 1E 1742.5−2859 was at least 4 times weaker during the 1985 *SPARTAN*-1 observations than it was during the 1979 *Einstein* observations. *SPARTAN*-1 detected hard X-ray emission, centered near the Galactic center, with $\sim 1^\circ$ in extent along an axis aligned to within 20° of the Galactic equator. The maximum (2–10keV) surface intensity is 1×10^{-6} erg cm^{-2} sr^{-1}. The total luminosity of the region $60' \times 30'$ centered Sgr A West is 3×10^{36} erg s^{-1} at 8.5 kpc.

Six weeks after the *SPARTAN*-1 mission, the *Spacelab* 2 mission carried a pair of coded-mask telescopes which images the Galactic Center region with $3' \times 3'$ and $12' \times 12'$ resolution ([94]). The energy range extended up to 30 keV. The *Spacelab* 2 detected the several hard X-ray sources and the extended emission about 1° from the Galactic center ([94]). The luminosity $L_{4.25-15{\rm keV}}$ of extended emission was estimated to be 1.1×10^{37} erg s^{-1} at 8.5kpc. Skinner et al. (1987 [94]) reported that the flux from the Galactic center was 7 times greater than that expected based on the *Einstein* observations. This result indicates strong variability during the 6 weeks interval between the *SPARTAN*-1 mission and the *Spacelab* 2 mission.

Using the *Ginga* satellite, Koyama et al. (1989 [51]) and Yamauchi et al. (1990 [108]) carried out the survey along the Galactic plane with a field-of-view $1^\circ.0 \times 2^\circ.0$.

They found that the iron 6.7-keV emission line concentrates in the Galactic Center $1.8^\circ \times 1.0^\circ$ (FWHM) tilted 21° with respect to the Galactic plane. The total energy of thin thermal plasma is 10^{54} erg s^{-1} and the typical temperature is about 10 keV. They proposed that multiple supernova explosions (about 10^3 SN) or, alternatively, an energetic explosion of about 10^{54} erg took place in the Galactic Center region during the last 10^5 yr.

Sunyaev et al. (1993 [101]) and Markevitch et al. (1993 [65]) observed the Galactic Center region with the ART-P telescope onboard *Granat*. The ART-P is a coded mask imaging telescope with $5'$ angular resolution and a $3^\circ.6 \times 3^\circ.6$ fully coded field-of-view in the energy band of 2.5–35 keV. They confirmed the extended emission ($\sim 1.5^\circ$) in the energy bands 2.5–5 keV, 5–8.5keV, and found in the harder 8.5–22 keV interval with the $15'$ angular resolution. The image at energies greater than 8 keV extended much more elongated parallel to the Galactic plane and has some features in common with the map of the molecular gas clouds ([101]; [65]). Sunyaev et al. (1993 [101]) proposed that the clouds Thomson-scatter a few tens of per cent of the hard X-ray continuum of the 5 point sources because the distribution of the emission correlates with that of the dense Galactic Center molecular clouds.

The PSPC/*ROSAT* with the soft X-ray mirror (0.1–2.5 keV) which have the angular resolution about $3''$, has observed the Galactic Center in 1992 ([85]). A point source was detected in the local extended structure at Sgr A West. The position coincides with that of Sgr A* less than $10''$. The luminosity is 7.4×10^{35} erg s^{-1} (0.8–2.5 keV) at 8.5 kpc assuming $kT = 5$ keV and $N_{\rm H} = 1.5 \times 10^{23}$ H cm^{-2}.

1.2.3 Large-Scale Diffuse X-ray Emission in the Galaxy

The X-ray sky along the Galactic plane exhibits many bright point sources, consisting mainly of neutron star binaries (e.q. [111]). In addition to these bright sources, fainter and unresolved X-ray emission was also observed ([115]). Since this emission concentrates near the Galactic inner disk (within $\sim 60^\circ$ of longitude), this is referred to as the Galactic ridge emission ([115]).

Warwick et al. (1985 [111]) carried out the scanning observation of the Galactic plane with *EXOSAT*. *EXOSAT* has a collimated field-of-view of $0^\circ.75 \times 0^\circ.75$. They

detected the diffuse X-ray emission apart from many resolved point sources, thus confirming the *HEAO*-1 results ([115]). This emission region extends up to far $\pm 45^\circ$ in longitude from the Galactic Center.

Koyama et al. (1986 [50]) performed the observations of selected source-free regions along the Galactic ridge with the GSPC onboard *Tenma*. GSPC/*Tenma* is the gas scintillation proportional counters with a field-of-view of a radius $3^\circ.1$ (FWHM). They found an iron K emission line in the Galactic ridge emission, thus revealing that the ridge emission is undoubtly due to thermal emission from optically thin hot plasmas. The ridge spectra obtained with GSPC/*Tenma* are well represented by a thermal bremsstrahlung model with temperature of 4–13 keV, and some of them revealed a hint of Si K and S K emission lines.

Using the *Ginga* satellite, Yamauchi & Koyama (1993 [109]) carried out the iron-line survey along the Galactic plane. The 6.7-keV line is associated with the extended high temperature($\sim$10keV) plasma. The 6.7-keV iron line emission was also found to largely extend along the Galactic plane (figure 1.5). The scale height is determined to be 100 ± 20 pc. The total iron line luminosity from the Galactic ridge is estimated to be $(6.5\pm1.3)\times10^{36}$ erg s^{-1}. Yamauchi & Koyama (1995 [110]) reported on the energy and equivalent width of the iron line as a function of the plasma temperature of the Galactic ridge emission with *Ginga*. The line energies and equivalent widths are systematically lower than those expected from a collisional ionization equilibrium plasma with cosmic abundance. They proposed the possibility that the optically thin hot plasma is in a non-equilibrium ionization state with an ionization parameter ($n_e t$) of 10^{10-11} cm^{-3} s.

Yamauchi & Koyama (1993 [109]) also discovered another diffuse emission feature near the Galactic bulge with luminosity about $(2.8\pm0.8)\times10^{36}$ erg s^{-1}. They suggested that this emission extends to a higher Galactic latitude of more than 750 pc over the Galactic Center.

Although the ridge emission is thus considered to be primarily of thermal origin, Yamasaki et al. (1997 [107]) pointed out, using the *Ginga* data, that there is a possible contribution from non-thermal components, which can be well extrapolated to the ridge emission in the soft γ-ray band with a single power-law model.

With *ASCA*, Kaneda et al. (1997 [44]) obtained the fine ridge spectra in the Scutum arm. They found that the observed spectra are basically of thermal emis-

sion from thin hot plasmas and individual K emission lines from helium-like Mg, Si, S, and Fe ions are confirmed, which means that at least two plasma components of $kT \sim 0.8$ (soft component) and ~ 7 keV (hard component). The soft component was found to be in an extremely low ionization state, with $n_e t \sim 10^9$ cm^{-3} s, while the harder component is in a relatively high ionization state, though not yet in a full equilibrium. They found that the surface brightness of the soft component extends towards significantly higher ($\sim 2^\circ$) Galactic latitudes than the hard component, although their actual scale heights may be similar at ~ 100 pc if the differences in their observable depths are taken into account. Spectral properties of the two components were seen to depend on the latitude; the most noticeable effect is a rapid decrease in the Fe K line equivalent width seen in the hard component, which is possibly related to the non-thermal component suggested by *Ginga* ([107]). They concluded that the soft and hard components originate supernova remnants and diffuse hot plasmas filling the interstellar space, respectively, where the Galactic magnetic fields may play an important role.

Maps of the soft X-ray background in the 0.1–2.0 keV range derived from the *ROSAT* all-sky survey (RASS) data were presented in Snowden et al. ([95] for the first maps & [96] for the second maps). These maps were produced in six energy bands, which were performed point-source masks using the RASS-I survey source catalog with the constant count-rate thresholds. They discussed the color of the $\frac{1}{4}$ keV radiation, and its implications for the location of the emitting material. They confirmed the existence of a spatially variable Galactic halo at $\frac{1}{4}$ keV (e.q. [29]) in addition to the extragalactic origin. They found evidence for a large-scale variation in the hardness, with the Galactic Center direction in general being harder and the Galactic anticenter direction softer.

They ([96]) also consider the bright 0.5–2.0 keV enhancement in the general direction of the Galactic center. Some have argued that the enhancement is due to emission associated with Loop I ([28]). Other suggests that much of it originates as far away as the Galactic center ([23]). They used the latitude dependence of the excess and the absorption trough in the Galactic plane to argue that the southern hemisphere part of the enhancement is almost entirely due to the emission from the Galactic X-ray bulge, while the northern part is a superposition of bulge and Loop I emission. They made the assumption of the cylindical bulge emission with an exponential fall-off of density with height above plane. The cylinder has a

radial extent of ∼5.6 kpc. The X-ray emitting gas has a scale height of 1.9 kpc, an in-plane electron density of $\sim 3.5 \times 10^{-3}$ cm^{-3}, a temperature of $\sim 10^{6.6}$ K(=0.34 keV), a thermal pressure of ∼28,000 cm^{-3} K($= 3.9 \times 10^{-12}$ erg cm^{-3}), and a total luminosity of $\sim 2 \times 10^{39}$ erg s^{-1} assuming a collisional ionization equilibrium (CIE) plasma emission model.

Park et al. [83] performed a mosaic of seven *ROSAT* PSPC pointed observations in the direction of ($l_{\rm II}$, $b_{\rm II}$) = (10°, 0°), which revealed deep X-ray shadows in the 0.5–2.0 keV band cast by dense molecular gas. The comparison between the observed on-cloud and off-cloud X-ray fluxes indicates that ∼ 43% of the diffuse X-ray background in this direction in both the 0.75 and 1.5 keV bands originates behind the molecular gas, which is indicated at 2–4 kpc from the Sun. Given the short mean free path of X-rays in the 0.75 keV band in the Galactic plane, they derived that this large percentage of the observed flux that originates beyond the molecular gas, most likely indicates a strong enhancement in the direction of X-ray-emitting gas near the Galactic center region.

1.2.4 Galactic Diffuse γ-ray Emission

γ-ray observations of the Galactic Center region in the early 1970s provided the first evidence of the Galactic positron annihilation radiation (e.q. [42]). Until the late 1970s, the 511 keV line from positron annihilation was unambiguously identified and evidence for the detection of positron continuum was reported (e.q. [56]). Purcell et al. (1993 [88]) and Purcell et al. (1997 [89]) carried out numerous observations of the Galactic plane and Galactic Center region with the Oriented Scintillation Spectrometer Experiment (OSSE). They revealed the good qualitative spectra in the 0.05–4.0 MeV band and confirmed the 511 keV line from positron annihilation and the positron continuum (figure 1.6). Purcell et al. (1997 [89]) combined the OSSE data with scanning observations by the Transient Gamma-Ray Spectrometer (TGRS) and Solar Maximum Mission (SMM) instruments to produce maps of the Galactic narrow 511 keV positron annihilation line radiation. They found evidence for three distinct features in the maps: (1) a central bulge, (2) emission in the Galactic plane, and (3) an enhancement or extension of emission at positive latitudes above the Galactic Center (figure 1.6). Although there are various possible production mechanisms for the observed positrons, including the

positive-latitude enhancement, they found that enhanced supernovae activity in the Galactic Center are capable of producing positrons at the required rate to account for the intensity and morphology of the observed 511 keV line emission.

Another remarkable γ-ray result was a 1.8 MeV line caused by the decay of ^{26}Al into ^{26}Mg. As the half life of ^{26}Al is only about 10^6 years, the 1.809 MeV line samples the most recent episodes of energetic nucleosynthesis in the Galaxy. Schöenfelder (1997 [93]) have recently reported detailed map of the 1.809 MeV ^{26}Al line taken with the COMPTEL spectrometer onboard the Compton Gamma-Ray Observatory. The line emission mainly concentrates along the Galactic plane. The brightest peak is near the Galactic Center, but shifted a few degrees to positive Galactic latitude. There are bright spots and empty regions along the plane. The reason for the clumps may be that nearby sources contribute significantly. Probable source candidates are Vela, Carina, the Cygnus region and tangential projections to the spiral arms. These findings all support the understanding that ^{26}Al is produced in massive stars, possibly Wolf-Rayet stars. Although the β decay of the ^{26}Al nuclei emitting the 1.8 MeV emission also lead to emission of positrons, the different distribution of these two γlines would require the different origin for each component.

The high energy diffuse γ-ray emission above 30 MeV from the Galactic plane was also detected. Hunter et al. (1997 [34]) have recently reported observations of the Galactic plane ($|b| \leq 10^\circ$) using the Energetic Gamma-Ray Experiment Telescope (EGRET) on the Compton Gamma-Ray Observatory. The flux in the 30MeV–50GeV band showed the overall enhancement toward the inner Galaxy, while the peak of the diffuse emission was not seen at the Galactic Center except for a point-like source 2EG J1746−2852 near the Galactic center. At latitudes $|b| > 2$, corresponding to γ-rays emitted within about 3 kpc of the Sun, there was no significant variation in the spectra with Galactic longitude. Comparison of the spectra from the Galactic plane ($|b| < 2$) revealed no significant variation with Galactic longitude below about 4 GeV, which suggests that the cosmic-ray electron to proton ratio does not vary significantly throughout the Galaxy. Above 4 GeV, however, there was weak (about 3 σ) evidence for variation of the Galactic plane ($|b| < 2$) spectrum with longitude. The spectrum was softer in the direction of the outer Galaxy compared to the spectrum from the inner Galaxy. They pointed out that this variation of the diffuse γ-ray emission hints at a variation

of the cosmic-ray proton spectrum with Galactic radius, which might be expected if cosmic rays are accelerated primarily in the inner Galaxy and then propagate to the outer Galaxy or if the high-energy cosmic rays are confined less well in the outer Galaxy.

The extremely high energy diffuse γ-ray emission above 1 TeV has been not detected near the Galactic Center, yet. Only the point source search near the Galactic center were carried out two telescopes: the Whipple 10-m γ-ray telescope covering above 2 TeV energy band ([13]) and the JANZOS (Japan Australia New-Zealand Observation of Supernova 1987A) scintillator array covering the 100-3000 TeV energy band ([2]). No significant emission was detected from the Galactic center both by the two telescopes.

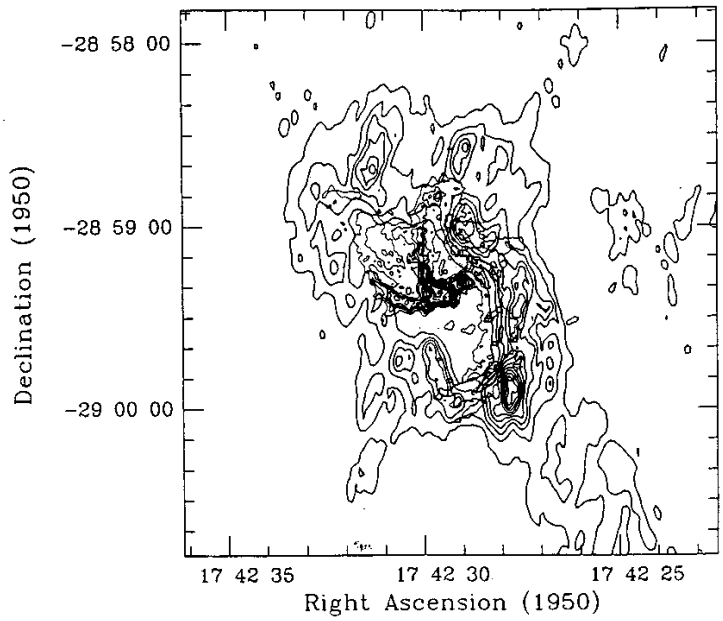

Figure 1.1: A 3-mm HCN $J = 1 \rightarrow 0$ aperture synthesis map at $3''$ resolution (CND: Wright et al. 1987 [116]) combined with the 6cm radio continuum map at $1''$ resolution (the mini spiral: Lo et al. 1983 [59]).

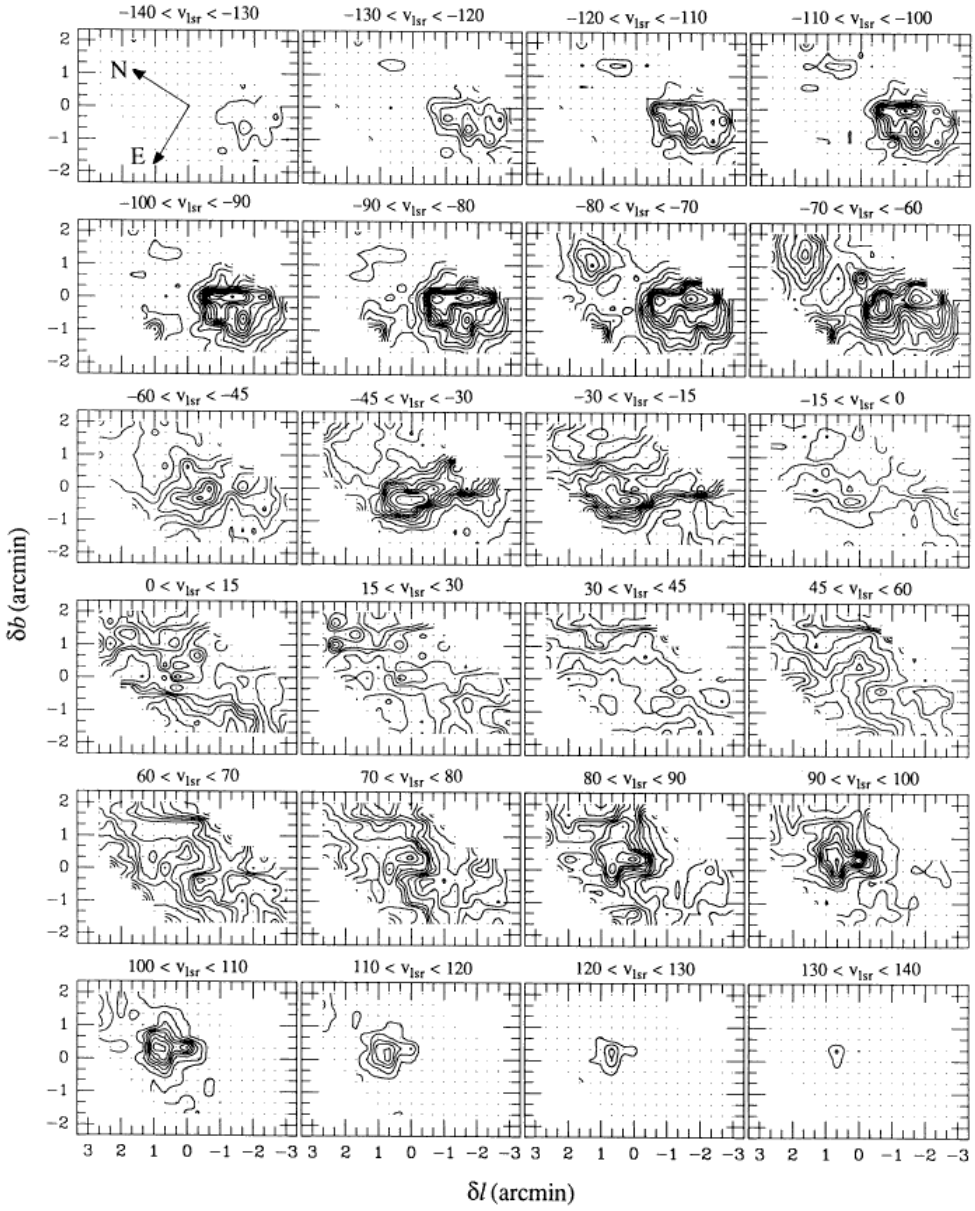

Figure 1.2: Velocity-averaged maps CO $J = 3 \rightarrow 2$ emission from Sgr A West (Sutton et al. 1990 [99]). For $|v_{lsr}| > 60$ km s^{-1}, the averages are taken over 10 km s^{-1} bins; For $|v_{lsr}| < 60$ km s^{-1}, the bins are 15 km s^{-1} wide. In all maps, the lowest contour level is 1 K with contours every 1 K through 10 K and every 2 K thereafter

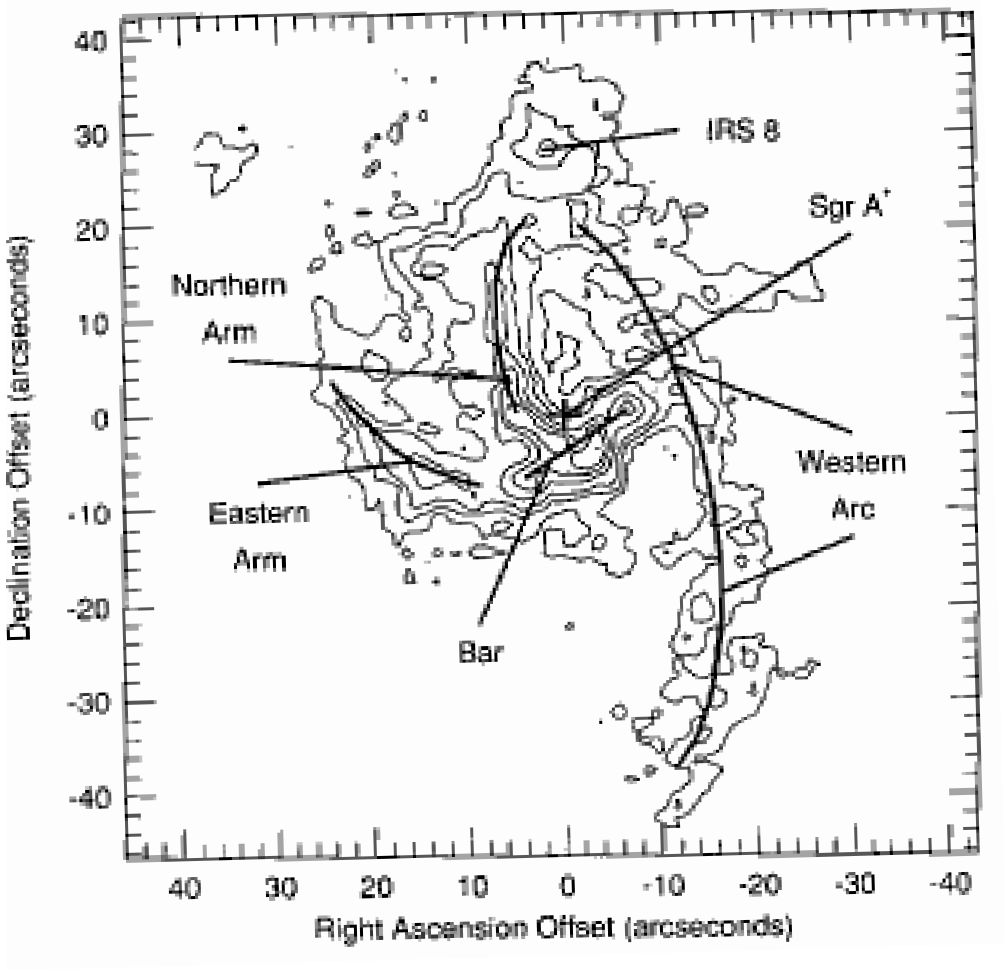

Figure 1.3: Contour map of $Ne_{II}(12.8\mu m)$ emission from Sgr A West (Lacy et al. 1991 [54]). Contour levels are (3, 6, 10, 20, 30, 40, 60) $\times$ 10^{-2} erg s^{-1} cm^{-2} sr^{-1}. Noise level (1σ) is 0.7 $\times$ 10^{-2} erg s^{-1} cm^{-2} sr^{-1}. The Western Arc is the diffuse, slightly curved filament crossing the frame from top to bottom to the right(west) of center; the Northern and Eastern Arms are the well-defined filaments extending from the vicinity of the center of the image to the north and east, respectively; and the Bar is the bright, clumpy east-west structure near the center of the image.

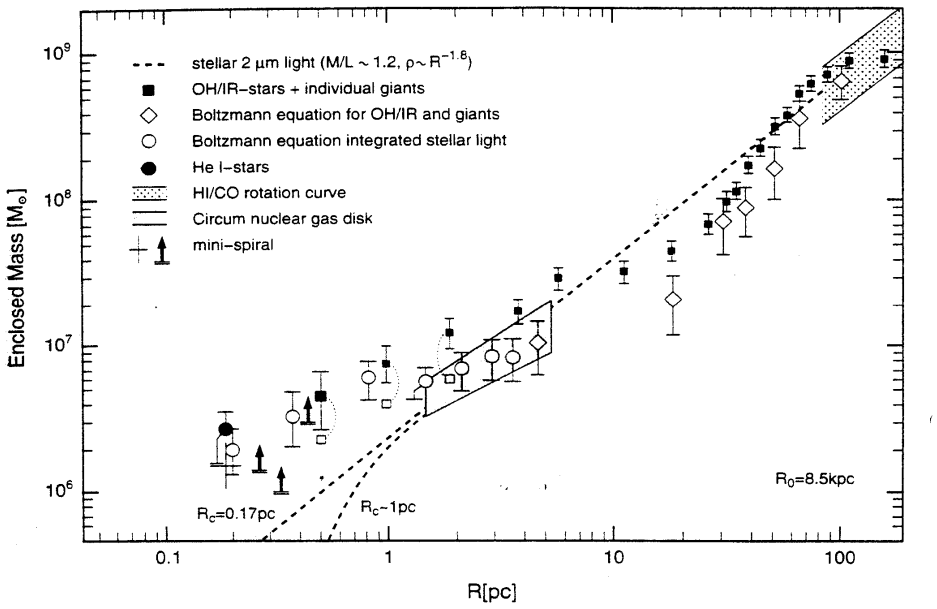

Figure 1.4: Mass distribution in the central 100 pc (Genzel et al. 1994 [24]). Stellar cluster models with core radius 0.17 pc and 1 pc and M/L = 1.2 $M_\odot/L_\odot$ (spherical distribution) are indicated by dashed lines. The data appear to require a dark mass central mass of 1 to 3×10^6 $M_\odot$.

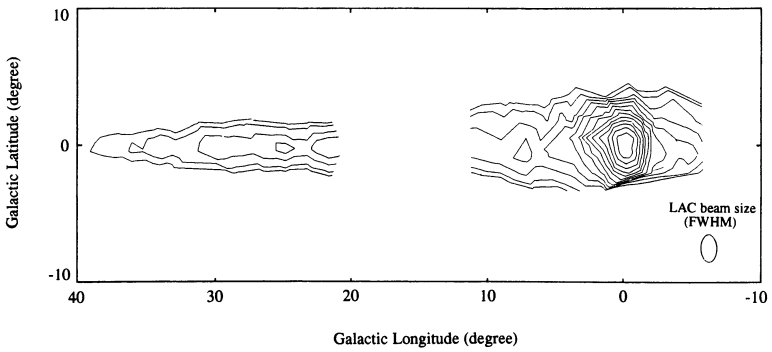

Figure 1.5: Two dimensional distribution of 6.7-keV iron line emission in $-6^\circ \leq l \leq 11^\circ$ and $20^\circ \leq l \leq 40^\circ$ regions obtained with *Ginga* (Yamauchi *et al.* 1993 [109]). The contour levels are 1.0, 1.2, 1.6, 2.0, 2.5, 3.2, 4.0, 5.0, 6.3, 7.9, 10.0, 12.6, and 15.8 photons s^{-1} $detector^{-1}$.

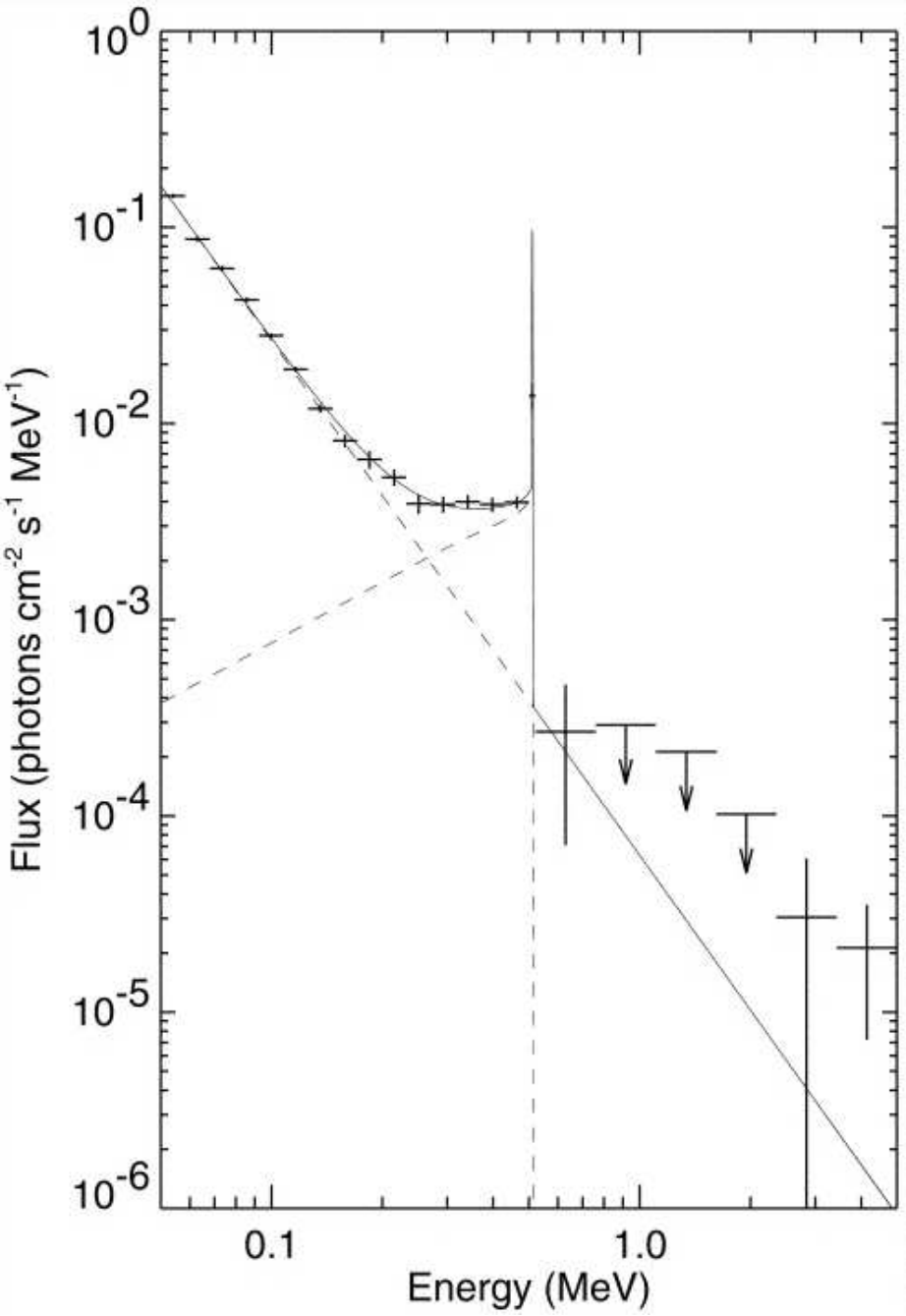

Figure 1.6: The OSSE Galactic Center spectrum from the 1991 December observation (viewing period 16) (Purcell et al. 1997 [89]). The spectrum represents the sum of all four detectors. The data were fitted over the energy range 0.05–4.0 MeV with a function consisting of a single power law, a photopeak line fixed in energy and width at 511 keV and 2.5 keV, respectively, and a positronium continuum component. The dashed lines show the contribution of each of these components.

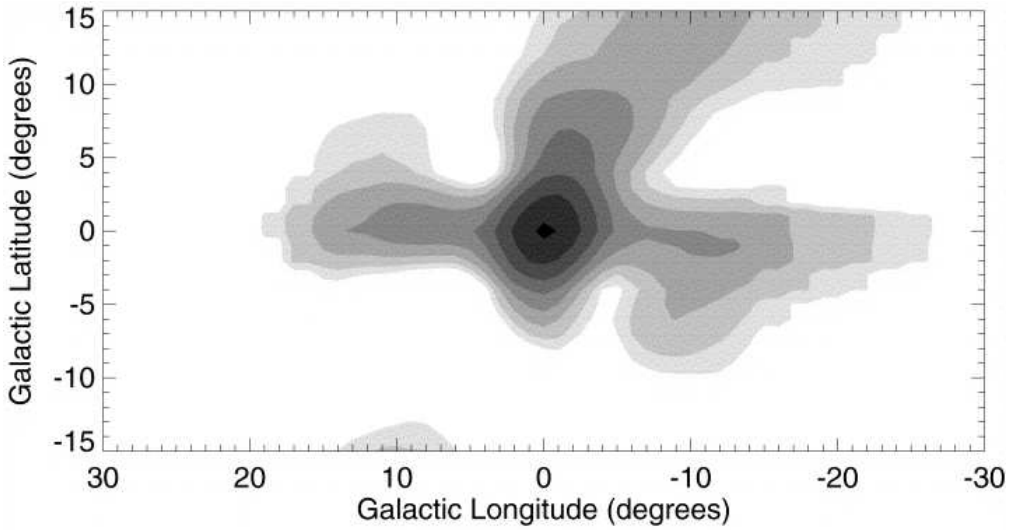

Figure 1.7: Map of the Galactic 511 keV positron annihilation line using the SVD method (Purcell et al. 1997 [89]). Contours are exponentially spaced.

Chapter 2

Instrument

In this chapter, we report on the *ASCA* satellite and its instruments onboard *ASCA*.

2.1 *ASCA*

ASCA is the 4th Japanese X-ray observation satellite launched on 20 February 1993, by the M–3SII–7 rocket from Kagoshima Space Center(KSC)([102]). The satellite orbit is semi-circular with the perigee of 520 km, the apogee of 620 km. It weights 417 kg and is 4.7 m long along the telescope axis and 3.5 m wide across the solar paddles. Figure 2.1 shows the schematic view of *ASCA* in orbit.

ASCA can contact KSC only for about 10 minutes each in 5 (or 6) consecutive orbits out of the 15. These orbits are usually called "contact orbits", and the other ten "remote orbits". During the remote orbits, *ASCA* can do down-link, or receive

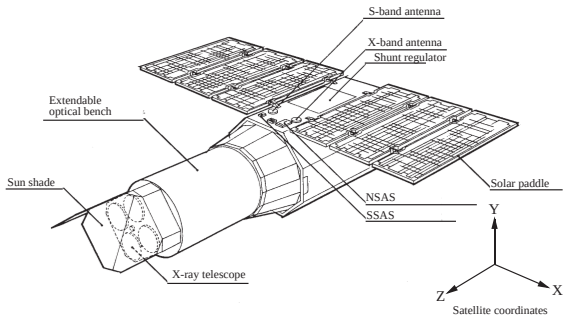

Figure 2.1: The schematic view of the *ASCA* satellite.

the stored data to the NASA DSN stations of Madrid, Canberra, Goldstone, Wallapse and San Diego. These reproduction is pre-programmed in the KSC contact pass.

ASCA has four observation instruments; two Gas Imaging Spectrometers (GIS:[79]; [63]) and two Solid state Imaging Spectrometers (SIS:[14]). As these instruments have imaging capabilities, each has X-ray telescope(XRT:[92]) of a 3.5 m focal length. Since M–3SII type rocket has no space to include the optical bench with the long focal length, the telescopes are mounted on the top plate of an extendable optical bench.

The satellite attitude is controlled in three-axis with the stability of better than $10''$ and absolute pointing accuracy about $\simeq 30''$. To achieve them, *ASCA* is equipped with 4 gyros with additional back-up one, four reaction wheels, two CCD star cameras and 3 magnetic torques each with control electronics. The satellite attitude is limited to keep the direction of the solar paddle within 30° from the sun. A biased and sun-direction angular momentum is always given in the 4 wheels, hence, in emergency, the satellite can automatically go into a safe-hold mode, which is a spinning mode around the sun vector. The maneuver is performed by changing the angular momentum balance among the reaction wheels with the slew rate of $\simeq 0^\circ.2\ \mathrm{s}^{-1}$.

As the telemeter channel, *ASCA* uses X-band (down-link at KSC, 8.5 GHz) and S-band (up-link 2.1 GHz, down-link 2.3 GHz). The orbital elements are measured twice a day. The data from the detectors and on-board instruments are compiled by the data processor (DP), then stored in the bubble data recorder (BDR) of 134 Mbits capacity. The telemeter has three bit-rates, HIGH of 32 Kbits s^{-1}, MEDIUM of 4 Kbits s^{-1} and LOW of 1 Kbits s^{-1}; thus the recording time is 68, 545 and 2185 minutes, respectively. HIGH-bit-rate is mainly used in the contact orbits, and MEDIUM-bit-rate is in the remote orbits. LOW-bit-rate is used to save the BDR capacity in case that the detectors cannot observe the target, i.e., the satellite is in the South Atlantic Anomaly (SAA) or the target is behind the earth.

2.1.1 XRT

ASCA has four identical conical foil X-ray mirrors which are weight saved versions of similar mirrors flown earlier on the Broad Band X-Ray Telescope experiment

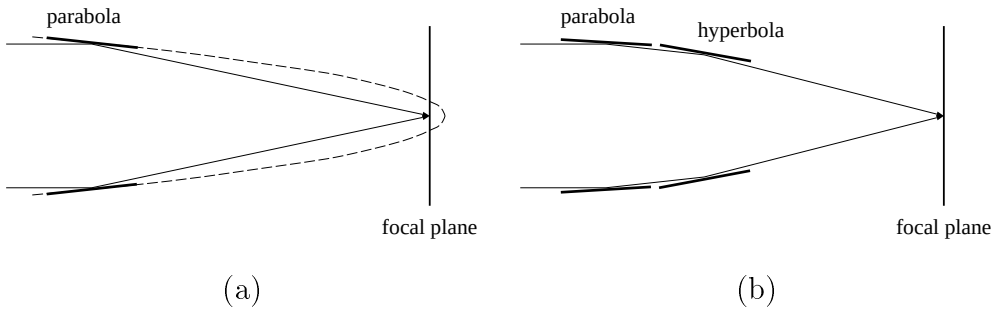

Figure 2.2: The schematic figure of the X-ray telescope. (a) The primitive model. (b) Wolter type I geometry, which is used in *ASCA* XRT.

(*BBXRT*) aboard Astro-1, which is one of the space shuttle mission developed by NASA. Since the X-ray photon of a few keV is reflected only in a grazing incident angle, or the light pass is almost parallel to the mirror surface, the effective area of the X-ray reflector is largely limited; see in the case of paraboloid (figure 2.2a), for example. To gain reflection area and to compensate aberrations, the X-ray mirror consists of multi-nesting tandem with aligned and co-focusing paraboloids and hyperboloids (Wolter type I geometry; figure 2.2b). *ASCA* XRT approximates this concept with a flat conical surfaces instead the parabolic and hyperbolic surface. This simplification is crucially practical, allowing us to construct the multiple-nesting of 119 thin foils for one XRT. Nearly flat pieces of the aluminum foil of 125μm thickness are first shaped into flexible conical segments having approximately the required curvature, then dipped in an acrylic bath to smooth the surface, deposited a $\sim$ 500 Å gold layer to increase X-ray reflectivity, then finally placed into a housing, constrained by supporting lags to fit the X-ray optics. One XRT with 119 foils aligned by $\sim$ 1 mm pitch has a 558 cm^2 effective area, more than 50% of the geometric open area. A trade-off of this large effective area by the thin foil mirrors is found in less spatial resolution than the ideal Wolter type 1 optics. The half-power diameter of XRT is about 3 arcmin. Table 2.1 gives the design parameters of XRT.

To maintain the best-performance of the mirror in orbit (i.e., to keep the reflecting surfaces free from contaminations and to minimize the mirror deformation by thermal stress), heaters and thin (0.22 and 0.54μm for the SIS and GIS, respectively) aluminized mylar covers were placed near and on the entire mirror aperture. Since X-ray reflectivity depends on the grazing angle and photon energy, the efficiency and point spread function (PSF) of XRT also depend on the source position

Table 2.1: XRT design and performance parameters.

Design Parameters	
Mirror Substrate	0.125 mm aluminum foil
Surface	10μm Acrylic Lacquer + 500 ÅAu
Number of Nested Cones	120 (back-to-back layers)
Outer/Inner Diameter	345/120 mm
Focal Length	3500 mm
Grazing Angle Range	0.24–0.70 deg.
Geometric Area	558 cm^2 (each)
Field of View	24/16 arcmin (@1/7 keV)
Number of Telescopes	4
Mirror Weight	10 kg (each)
Performance Parameters	
Effective Area	$\simeq$ 300/$\simeq$ 150 cm^2@1.5/7 keV (each)
Size of Blur (Encircled Energy)	$\simeq$ 3 arcmin Half Power Diameter (no energy dependence)
Reflector Surface Roughness	$\simeq$ 3 Å

and energy. The efficiency and PSF are calibrated on ground in several points (in energy, mirror position, and incident angle), but overall features are simulated with the ray-tracing with appropriate optical constant (complex refractive index) of the mirror foils, including the real XRT structures. The final response is supplied by the *ASCA* team with fine tunings to fit the standard sources: Crab for spectrum and Cyg X-1 for imaging. Figure 2.3 shows the energy dependence of the XRT effective area. The values used to plot the graph is an integrated flux within the 6 arcmin radius circular area from the image center.

The effective area decreases rapidly as the off-axis angle increases. At higher incident energy, since the grazing angle should be smaller, only inner foils remain effective. Accordingly, effective area decreases as incident photon energy increases. Figure 2.4 shows the effective area for each off-axis angle as a function of energy.

Possible residual deformation of the foils worsens the angular resolution. While the half power diameter (HPD) of XRT is expected to be about 0.3 arcmin in the ideal case, the real value is about 3 arcmin. Figure 2.5 shows the radial profile of the PSF. It can be approximated as a Gaussian in the central core of ($r <$

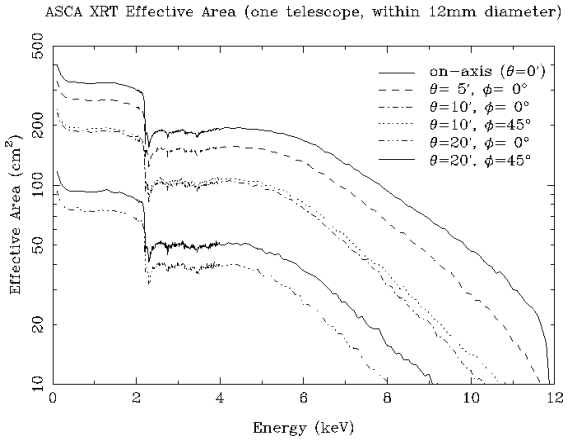

Figure 2.3: The energy dependence of the XRT effective area on-board *ASCA*.

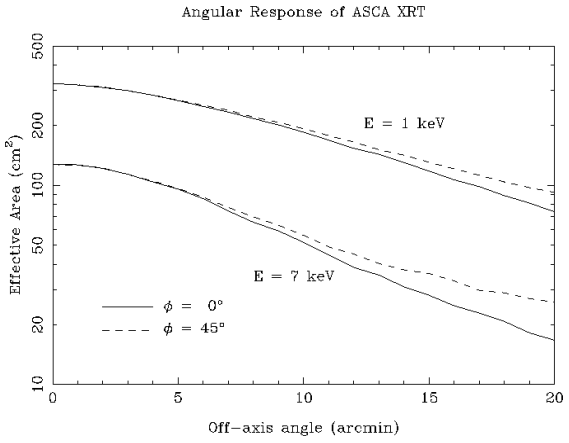

Figure 2.4: The off-axis angle dependence of the XRT effective area on-board *ASCA*.

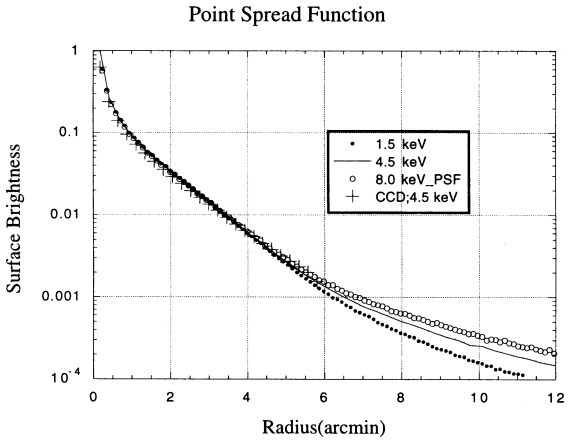

Figure 2.5: The point spread function of the *ASCA* XRT.

1′), followed by an exponential function outside. The quadrant mirror structure make the PSF to be the Maltese-cross shape (figure 2.6). As the off-axis angle increases, the PSF is largely distorted. For the evaluation of the contamination of a bright source to the surrounding regions, the encircled energy function (EEF) which is defined as the ratio of photons flux in a circle with given radius from a point source is useful. Figure 2.7 shows the EEF for different energies. It shows that the 80% of the flux drops within the circle of a 2 arcmin diameter. The difference of the encircled fraction between high and low energy become large as the increasing angular radius. Therefore, the apparent spectrum becomes harder as the accumulation radius increases.

Another practical problem of the XRT is stray light from outside of the field of view (FOV). The XRT geometry does not allow photons reaching the focal plane without being intercepted by the foils; however, the photons scattered due to the surface roughness, single or more than 3 reflection, or back-side reflected photon may come in the focal plane. We call these photons as the stray light. Figure 2.8 shows the image of the stray light when the Crab nebula is 1° offset from the detector center. The stray light, if strong source is nearby, is crucial for a weak source or extended emission, like the cosmic X-ray background (CXB).

2.1.2 GIS

The GIS (Gas Imaging Spectrometer), which has been developed mainly by University of Tokyo, ISAS and Meisei Electric Co., Ltd., consists of two imaging scintillation proportional counters (GIS2 and 3) and a signal processing part (GIS-E).

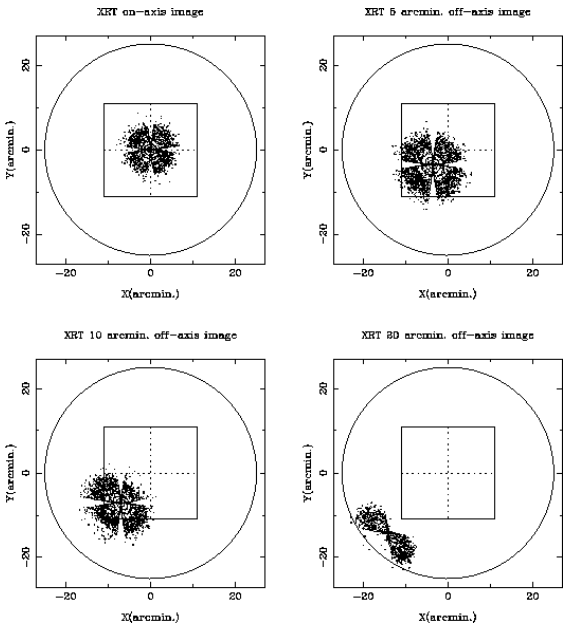

Figure 2.6: Point spread function of the *ASCA* XRT for four different off-axis angles. Approximate field of view is shown for GIS (circle) and SIS (square).

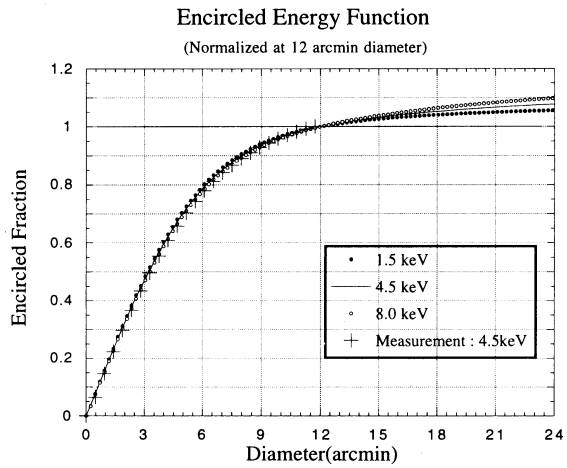

Figure 2.7: The encircled energy function of the XRT.

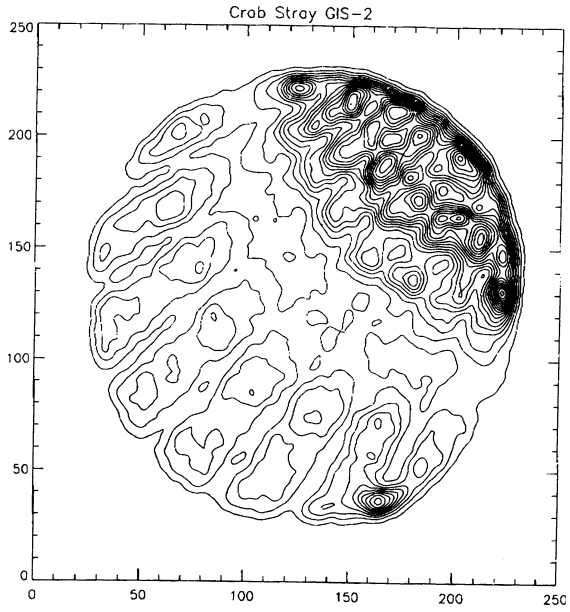

Figure 2.8: The stray light image of the Crab nebula at 1° offset from the detector center.

Also the radiation belt monitor (RBM) is equipped.

Compared with the SIS (see next subsection), the GIS has larger efficiency (by a factor of 2 at 7 keV) at high energy, higher temporal resolution, larger dynamic range in the source intensity and a four-times wider FOV; however, it has a lower soft X-ray efficiency, a somewhat worse position resolution and a factor 2–4 poor energy resolution.

Each GIS-S consists of a gas cell, a position-sensitive phototube and high-voltage suppliers. Figure 2.9 shows the cross section of the GIS-S. The X-rays from the XRT are detected by the 25 mm-depth gas cell, which is filled with 96% of Xe and 4% of He to 1.20 atm pressure (at 0°C). The gas is sealed by a beryllium foil of a 10μm thickness and a 52 mm diameter, supported by a stainless grid and fine mesh. The gas cell is divided into two, the drift region just inside the Be window and the following scintillation region. Each region is biased by 1 kV cm^{-1} and 4 kV cm^{-1} electric fields. To intercept the non-X-ray backgrounds, the GIS has the hood coated by a 0.2–0.5 mm thickness tin foil and partially by a 0.1 mm thickness molybdenum foil.

The X-ray photon is photo-absorbed in the drift region and creates free electrons. The electrons drift into the scintillation region guided by the bias field, then accelerated by the stronger field. The electrons excite the Xe atoms, then the

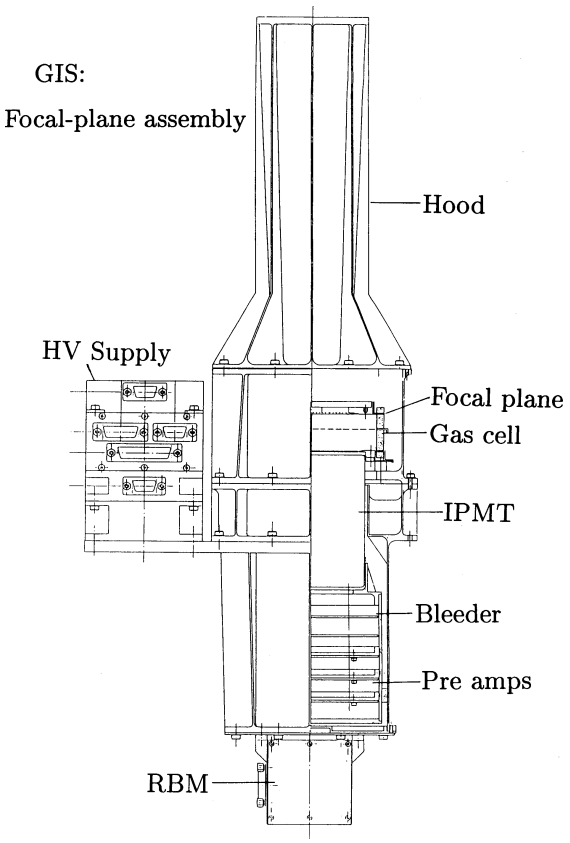

Figure 2.9: The cross section of the GIS-S.

excited Xe atoms emit UV photons of wavelength of $\simeq$ 170 nm. This excitation and relaxation processes occur as the electrons pass the scintillation region in 2–3μs; thus, makes a scintillating light column. The number of UV photons becomes $\simeq 1.5 \times 10^5$ for a 6 keV X-ray photon. Since these process is not accompanied by secondary-electron multiplication, the energy resolution is kept 2-3 times better than the proportional counter. The scintillation UV photons are detected by a position-sensitive phototube set below the gas cell.

The energy information is obtained from the final dinode signal. The energy resolution is about 8.0% (FWHM) at 5.9 keV, which scales as inverse square root of the energy. X and Y positions of a detected photon are calculated using outputs from 32 (16 for X and 16 for Y) multi-wire anodes. The position resolution is about 0.5 mm (FWHM), which corresponds to about 30 arcsec, at 5.9 keV, and scales as inverse square root of the energy. The signals from the phototube are processed by GIS-E.

To eliminate non-X-ray backgrounds, only signals with the pulse shape (rise time) of limited band is out to the on-board CPU. With this process, about 90% of backgrounds within the 2–10 keV band are eliminated. In addition, on-board CPU eliminates the event of which position is outer than the certain radius or the spatial distribution of multi-anode output is larger than the certain length. This discrimination method is called SPRD. Without SPRD, it is known that the strong source near the edge of the GIS, such as the calibration source, makes a ghost image at the inner area if the event position is determined with the Fast Lorentzian Fitting, used for the usual data processing. With these discriminations, 99% of non-X-ray background is eliminated and the residual non-X-ray background in the 17 arcmin radius is 5×10^{-4} counts s^{-1} cm^{-2} keV^{-1} in the 2–10 keV band.

Since the telemetry capacity is limited, the GIS has four different telemetry modes:

PH (Pulse Height) For nominal observations, this mode is usually used. One event consists of the pulse-height, position, rise-time, event-spread and timing information packed to 31 bits. The commandable bit-share are 10, 8, 5, 8 and 10 bits in normal operation. In this mode, all the data are processed by on-board CPU.

PH PCAL (Position Calibration) This mode is prepared for the calibration

Table 2.2: The temporal resolutions and the maximum source intensities of the GIS.

mode	Bit rate	Temporal resolution Timing bits 0 bit	Timing bits 10 bits	Maximum Source Intensity [count s^{-1}]
PH	H	62.5 ms	61μs	256
	M	500 ms	488μs	32
	L	2 s	1.95 ms	8
PCAL	H	31.25 ms		32
	M	250 ms		4
	L	1 s		1
MPC	H	0.5 s	1.95 ms	128 Crab†
	M	4 s	15.6 ms	16 Crab
	L	16 s	62.5 ms	4 Crab

†: 1 mCrab $\sim$ 1 event s^{-1}

of the position calculation done by on-board CPU. All information including 32 anode signals are transmitted. Thus the maximum source intensity and the temporal resolution are reduced much from the PH-mode. PCAL data, however, can be processed on ground in failure mode of on-board CPU.

MPC (Multi-channel Pulse Count) This mode transmits only the pulse-height and timing information. The pulse-height converted data are accumulated in on-board memory in DP. The maximum number of spectral bin is 256, which can be reduced to increase time resolution. This mode can be used for an extremely strong source or in a failure made of on-board CPU.

Memory Check This mode dumps the RAM image (32 KB$\times$2) of on-board CPU. Usually, this mode is carried out once a day during the KSC contact to check whether on-board memory is correct or not.

Table 2.2 gives the temporal resolution and maximum source intensity of the GIS in each telemetry mode.

The gain of the GIS differs from position to position, hence the gain calibration by pointing Cas A in various positions has been performed. In addition, the gain changes with the pressure and the impurity of the counter gas and the phototube temperature. To correct these effects, the gain of the GIS is monitored by ^{55}Fe

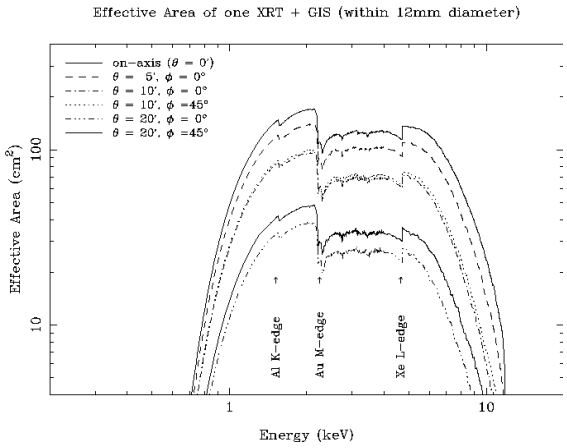

Figure 2.10: The effective area of the combination of XRT and GIS.

isotopes at the edges of the entrance windows of the each gas cell. These calibration data are accumulated by the *ASCA* team and distributed to the end users.

Figure 2.10 shows the effective area of the combination of XRT and GIS.

2.1.3 SIS

The SIS (Solid state Imaging Spectrometer) consists of three components — two cameras (SIS0 and SIS1), each with four CCD chips, the analog electronics (SIS-AE) and the digital electronics (SIS-DE). SIS-DE is equipped in the DP body. The DP also has responsibility of a part of the SIS data processing. Figure 2.11 shows the signal block diagram of the SIS subsystem.

The CCD detector can be regarded as a cluster of solid state detectors (SSD) with a large number of square-aligned microscopic ($27 \times 27 \mu\mathrm{m}^2$ in case of SIS) electrodes called 'pixels'. The electron cloud induced by the X-ray photon are absorbed by the nearest pixels, then are carried by the driving external clock from pixel to pixel to the readout gate.

Since the charge is thus transferred from pixel to pixel, which have very small electric capacitance, the floating electric capacitance at the readout gate also very small. This extremely small capacitance makes a higher readout voltage than normal SSD, hence the readout noise can be very small. On the other hand, the temporal resolution is much lower than the normal single detector such as GIS, because the charges are read sequentially. In the case of SIS, the readout cycle of one chip is 4, 8 or 16 sec in 1-, 2- or 4-CCD-mode, respectively.

Figure 2.12 shows the cross section of the SIS camera, and figure 2.13 shows

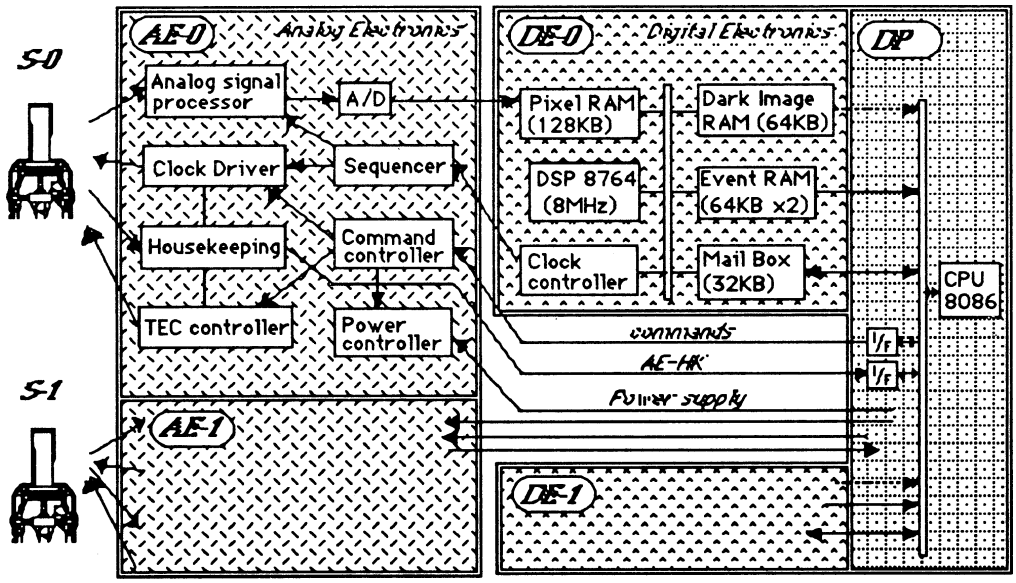

Figure 2.11: The signal block diagram of SIS.

the chip configuration of the SIS. In the normal operation, the CCD chip is cooled down to about $-60°$C by a Peltier device (TEC, thermal electric cooler) to reduce the dark current. The TEC dissipates the heat into the housing, which is cooled to -30–$40°$C with the radiator coupled to the heat pipe. The chip in the housing is covered by a multi-layer insulator and supported by Lexan columns in order to reduce the heat inflow. In front of the chip, a Lexan film of a 1000Å thickness coated with aluminum of a 400Å thickness at each side is placed to cut off the optical light.

The SIS-AE generates the chip driving clock, controls the TEC and converts the video signal from the SIS-S to the digital data (PH data). In contrast to GIS, SIS has no hardwired logic.

The SIS-DE receives the PH data from the SIS-AE and extracts the X-ray events. The X-ray photon of a 10 keV energy induces a primary electron cloud of a 1μm size by the photo-absorption process, with the size scaling as $E^{1.75}$ ([41]). After drifting to the electrode of each pixel, the size is grown to be $\sim 5\mu$m. Since this size still smaller than the that of pixel, the electron cloud does not separate into larger than four pixels (figure 2.14). On the other hand, charged particle events leave long tracks (long cloud). Using this difference of the cloud size, SIS-DE can eliminate the non-X-ray backgrounds. The energy of the X-ray event is calculated from 3×3 pixels around the local maximum pulse height pixel.

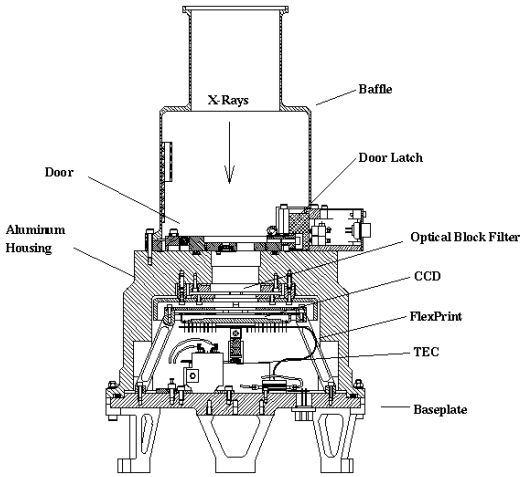

Figure 2.12: The cross section of the SIS camera.

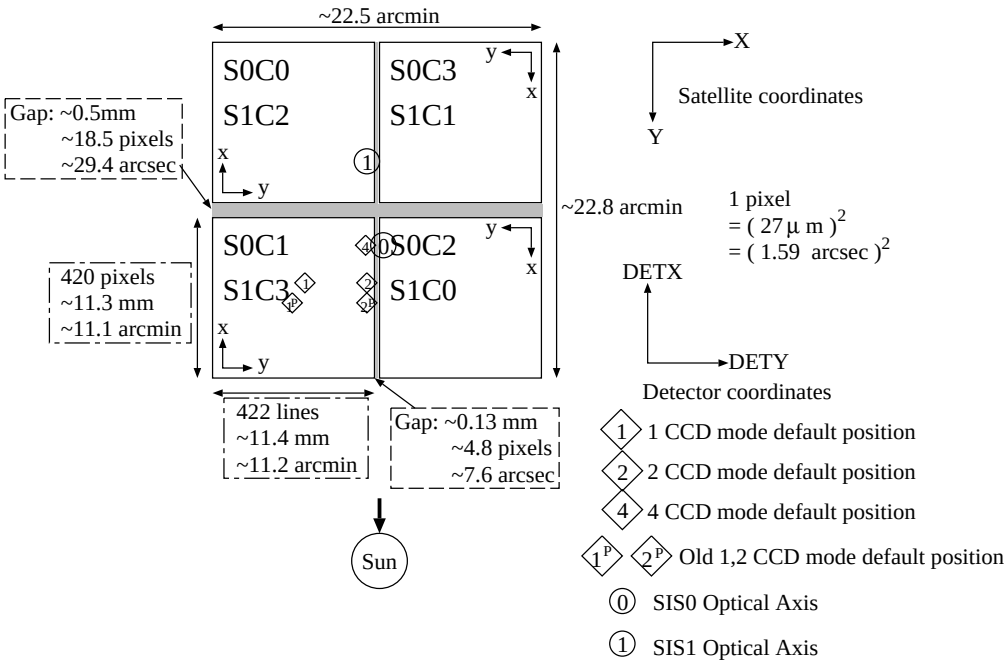

Figure 2.13: The chip configuration of the SIS.

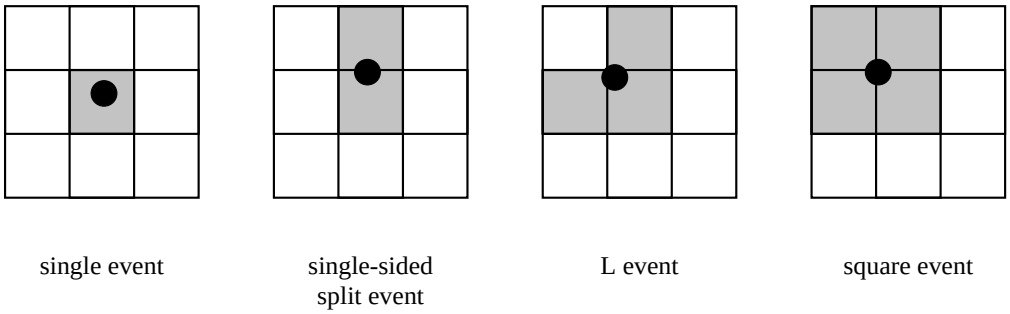

Figure 2.14: The X-ray event pattern of the CCD detector.

The dark current level consists of 'Dark level' and 'Bias level'. To save the on-board memory, the Dark level is taken from the average of the pixel group, which is typically in a $\frac{1}{16} \times \frac{1}{16}$ (default value) frame. This dark level is further time averaged and is updated using the event-free pixel levels as:

$$\text{NewDarkLevel} = \text{OldDarkLevel} + \frac{\text{MeanPixelLevel}}{n} + 1, \tag{2.1}$$

where $n+1$ is the history parameter and set as 1, 4, 8 or 16 on command. The set of Dark level is called the dark frame. The Bias level is the DC offset of the dark current level. This is obtained from the PH data of the overclock region, where there is no real electrode but only the driving clock is operated to these virtual pixels. Since the Dark level and the Bias level are the mean value in the grouped pixels, their possible variation within the group degrade the energy resolution essentially taken from multiple pixels. To take account or compensate this degradation, two approaches are currently used: (i) make the up-to-date response matrix including the long-term change of the resolution. This method can be applied for all the data, but needs the long term trend for pixel by pixel, which require a lot of work, hence has only been at a limited region. (ii) Since the dark level of each pixel is found to be rather constant in a shot time scale (a few days), we can obtain the pixel-by-pixel dark template for the short time scale, by observing the night earth with the FRAME-mode or accumulating the event-free corner pixels of the FAINT-mode data (see below). With this template, we can adjust the pulse height on the ground. This method can be applied for the FAINT-mode data and the grade-0 BRIGHT-mode data.

The SIS has three observation modes (FAINT, BRIGHT and FAST) and four diagnostic modes (FRAME, DARK FRAME, HISTOGRAM and INTEGRATION):

FAINT The event information consists of the CCD ID, the addresses and 12 bit pulse heights of nine pixels. The size of each event is 16 bytes including the CCD ID. This mode can be used only for faint sources, but all the pulse heights relating with the event is obtained.

BRIGHT The pulse heights of 9 pixels are summed, and the summed PH data and the Grade information are transmitted. Table 2.3 gives the definition of the Grades. The event data has 4 bytes and consists of the Grade, addresses and the summed pulse height binned up to 11 bit scale; the original 1024–2047 channels are binned by a factor of two and 2048–4095 by a factor of four.

FAST In this mode, the chip is driven to project all the charge onto one dimension, so the spatial information is reduced: instead, the scan period of a frame becomes faster than other modes. The event data has 2 bytes and consists of the Grade, the reduced addresses and the pulse height binned as the BRIGHT-mode. This mode is used for extremely strong point source for which each chip may be hit by X-rays more than the saturation level within accumulation time if we use the other modes.

FRAME This mode sends the pulse heights of all pixels with 12 bit resolution.

DARK FRAME This mode sends a map of dark frame to ground with 8 bit resolution.

HISTOGRAM This mode makes the histogram of pulse heights of 4096 bins for all pixels and send to ground.

INTEGRATION This mode integrates the events in the chip for 160 s, read the resultant pulse heights and send them to ground with 12 bit resolution.

The SIS has three clocking mode for observation and FRAME-modes — 1, 2 and 4 CCD-modes. The exposure time for each clocking mode is 4, 8 and 16 s, respectively. Table 2.4 gives the summary of three observation modes.

As the SIS has no radio isotope, the relative gain between each chip was determined with the strong Fe-K emission line of supernova remnant W49B. It was

Table 2.3: The grade definitions of the BRIGHT-mode SIS events.

grade	name	split pattern
0	single	center
1	single+	center (+ detouched corner(s))
2	vertical split	center + top or bottom (+ detouched corner(s))
3	left split	center + left (+ detouched corner(s))
4	right split	center + right (+ detouched corner(s))
5	single-sided+ (+ detouched corner(s))	single-sided split + touched corner pixel(s)
6	L or square	L or square split (+ detouched corner(s))
7	Others	all others

Table 2.4: Observation modes of the SIS.

	Faint	Bright	Fast
Temporal resolution†	4/8/16 s	4/8/16 s	16 ms
Maximum event rate‡	128/16/4	512/64/16	1024/128/32
PHA bits	12	11	11
Spatial bits	9×9	9×9	1 (and 3 timing bits)
Number of grade	—	8	2

†: In 1/2/4 CCD mode for Faint and Bright.

‡: In bit High/Med/Low. The unit is [events/s/2sensors].

pointed by all chips and the gains were determined within 0.5% errors. The absolute energy scale was determined with the strongest internal background emission line, Ni, which originate in the Kovar (an Fe-Ni alloy) frame-store shield.

In the transfer of the charge, there exists the charge loss which is called charge transfer inefficiency (CTI). The CTI is periodically calibrated pointing Cas-A at the each corner of chips. The calibration data is accumulated by the *ASCA* team and released to the end user.

Because of the limited telemetry capability, it is therefore possible to reduce their number in the telemetry by changing the event threshold or by applying three kinds of discrimination: Level discrimination, Grade discrimination and Area discrimination, respectively.

The event threshold is a fundamental parameter of the on-board processing, and can be changed only by the consensus of the SIS team. After initial testing during the early part of the PV phase, the event threshold was set at 100 ADU for all chips until 1995 Dec 23; after this date, the event thresholds in ADU have been set to different values for different chips such that they all correspond to an energy of 0.4 keV.

Level discrimination, when activated, plays a similar role (all events whose central pixel is below the threshold are discarded during on-board processing).

BRIGHT-mode has the eight grades (0-7), which are extensions of four basic groups: S (single), P (single-sided split; subdivided into Vertical, Left and Rights), L (L-shaped) and Q (square-shaped). The extensions arise because of the existence, in some events, of corner pixels which do not belong to the block since they touch the distributions only at the corners (so-called 'detached' corners). Usually, charge from an X-ray interaction (less than, say, 5 keV) is split into 1 or 2 pixels, i.e., S events (grades 0-1) and P events (grades 2-5). However, grade-1 events, which consist of single events with one or more detached corners, should be ignored because most are particle events (it is hard for an X-ray event to split charge diagonally). A sizable fraction of higher energy X-rays (5-10 keV), which tend to be absorbed deeper in the CCDs, are detected as L or Q (grade-6) events, while grade 7 events are dominated by particle events. Since each pixel included in the final PHA calculation contributes its own read-out-noise, grade 0 events have the best resolution and grade 6 the worst. The SIS team has concentrated on a combination of grades 0, 2, 3 and 4; this combination is therefore the best-calibrated. In some instances,

however, it may make sense to add grade 6 events (to increase signal-to-noise at high energies) or to concentrate on grade 0.

The CCDs that make up the SIS detector system are sensitive to optical light. Optical photons can be numerous, each creating an electron-hole pair; they can therefore have the effect of raising the dark level. We have discovered, moreover, that parts of SIS0 Chip 2 and Chip 3 suffer from 'light leakage': when the line of sight is close to the bright Earth, these regions produce many spurious 'detections', thought to be due to light entering SIS0 near these regions. They have effects that are similar to the flickering pixels, although the physical origins are distinct.

Chapter 3

Observations

3.1 Operation Mode

3.1.1 GIS Modes

Although the GIS has four modes, in practice the pulse height (PH) mode was used for all our observations. In this mode, the on-board CPU calculates the event position and discards background events using a specially designed event selection algorithm. Only accepted X-ray events are sent to the ground. With the standard bit assignments, pulse-height spectra consist of 1024 channels for each detector.

PH-mode allows some flexibility in how the telemetry is allocated. There are 31 bits per event to describe the pulse height("PH") value, X and Y position("X" and "Y"), rise time("RT"), spread("SP") and timing. Note that changing the bit assignments in PH-mode only changes the digital resolution, i.e., the binning, of the data.

The standard temporal resolution (timing bit=0) is 62.5 msec (in HIGH-bit-rate), 500 msec (in MEDIUM-bit-rate) and 2 sec (in LOW-bit-rate), respectively: using N bits for timing makes the temporal resolution times better. For most of our observations, we used the standard bit assignments (PH-X-Y-RT-SP-Timing) = (10-8-8-5-0-0). Note that telemetry capacity limits in the PH-mode are 128, 16, and 4 cts/s/sensor for the HIGH, MEDIUM, and LOW telemetry bit-rates respectively (table 2.2).

3.1.2 SIS Modes

Although the SIS has three observation modes, in practice the FAINT- and BRIGHT-modes were used for all our scientific observations. We applied the grade selection to on-board BRIGHT-mode telemetry included events with grades 0–4 or 0–6. FAINT-mode telemetry contain all events including grade 7. The affected areas by light leakage have been masked off in observations that use S0C2 and S0C3[1], whenever the line of sight is within 25 degrees of the bright Earth. Level discrimination was employed in some observations. We also obtained the FRAME-mode data to correct the radiation damage, for detail, given in appendix D.

3.2 Mapping of the Galactic Center Region

With *ASCA*, the mapping of the Galactic Center region was performed in '93 autumn. The observed fields were plotted in figure 3.1 and listed in table 3.1. The mapping covered one square degree with eight successive exposures of about 20 ksec each. All the SIS data were obtained in the BRIGHT mode, with all of the four CCDs in each SIS enabled (so called 4CCD-BRIGHT-mode), while all the GIS data were obtained in the standard PH-mode.

3.3 Large-Scale Mapping around the Galactic Center Region

Since we have no enough time to fully cover the larger regions around the Galactic Center, we performed the Chris-cross mapping, whose two axes intersect at the Galactic center (figure 3.2). The horizontal axis of the Chris-cross is corresponding to the Galactic plane(here after "on-plane"). The other axis is in the perpendicular direction to the Galactic plane("off-plane").

3.3.1 On-Plane

We performed the on-plane mapping with the shorter exposures of about 10 ksec. The observed fields were plotted in figure 3.4 and listed in table 3.2. Most of these

[1]SmCn, where n is the number of the SIS detector and m is the chip number.

data were taken as the Galactic plane survey project. Until November 1997, this project observation covered the region of $|l| < 30$ degrees. Since, in this thesis, we concentrate to the research for the activity near the Galactic Center, we used only the data of $|l| < 10$ degrees. Early results for the individual objects based on the data taken as this project have been already published: [48], [53], [98] and [103]. The systematic studies used of these data have been reported in the doctor theses written by Kaneda [43], Kinugasa[67], Matsuzaki[67] and Torii[104]. Except for the GP$-$1 field, the SIS data were obtained in the 4CCD-FAINT-mode for the HIGH-bit-rate and 4CCD-BRIGHT-mode for the MEDIUM-bit-rate. The SIS data in only the GP$-$1 field were obtained in the 4CCD-FAINT-mode for the HIGH-bit-rate and 1CCD-FAINT-mode for the MEDIUM-bit-rate. All the GIS data were obtained in the standard PH-mode.

3.3.2 Off-Plane

We performed the off-plane mapping with the longer exposure of roughly 30 ksec for each field. The observed fields were plotted in figure 3.4 and listed in table 3.3. All the GIS data were obtained in the standard PH-mode, except for the GB+1 field. The SIS data were obtained in various modes given in table 3.4. Because of the limited observable time, the mapping did not consecutively cover the off-plane regions and the number of the mapping to the positive Galactic latitude is less than that to the negative.

3.4 Monitoring Observations of the Galactic Center Sgr A

Two follow-up observations with deeper exposures of roughly 70 ksec each were made at the Galactic center Sgr A listed in table 3.5. These two observations were performed 1 year and 3.5 years later from the first observation named as the GC0 field. The SIS data are obtained in various modes given in tables 3.6. All the SIS data were applied with the RDD correction. All the GIS data were obtained in the standard PH-mode, except for the SgrA97 observation in HIGH-bit-rate.

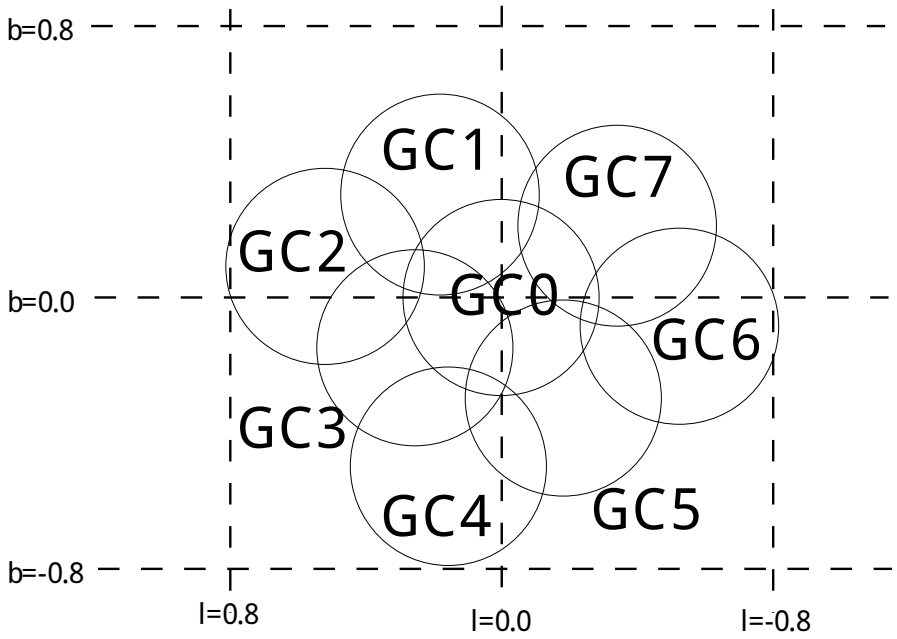

Figure 3.1: Galactic positions of the mapping fields of the Galactic Center region. Each of the solid circles represents the circular regions of 17′.5 radii of each observed field, from which GIS diffuse X-ray spectra were extracted.

Table 3.1: Observation log of the Galactic Center region

Field	Field center		Date(UT)	Exposure
	l_{II}(deg)	b_{II}(deg)	dd/mm/yy	ksec
GC0	−0.013	0.004	30/09/93	15
GC1	0.330	0.217	01/10/93	16
GC2	0.514	−0.082	01/10/93	16
GC3	0.170	−0.293	02/10/93	19
GC4	−0.169	−0.499	03/10/93	14
GC5	−0.265	−0.147	03/10/93	19
GC6	−0.534	0.094	04/10/93	19
GC7	−0.193	0.308	04/10/93	18

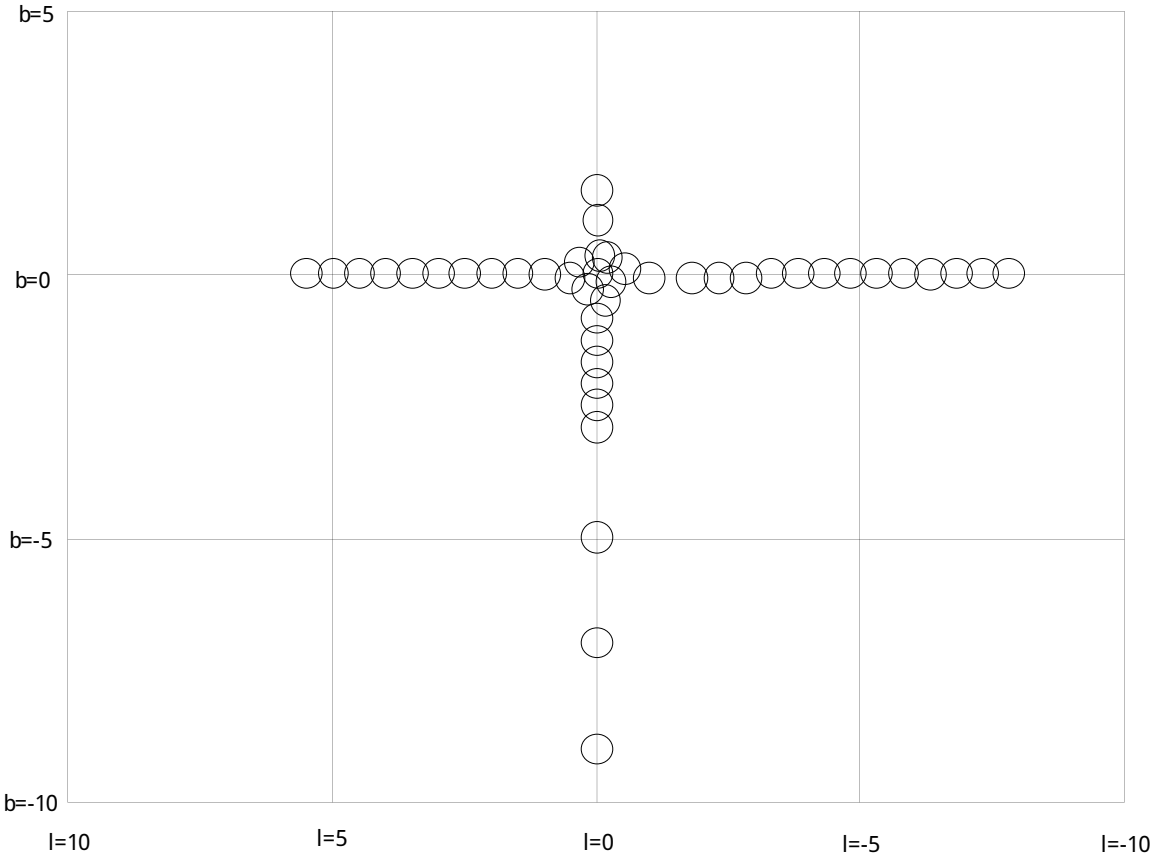

Figure 3.2: Same as figure 3.1, but for all the mapping fields including the Galactic Center fields.

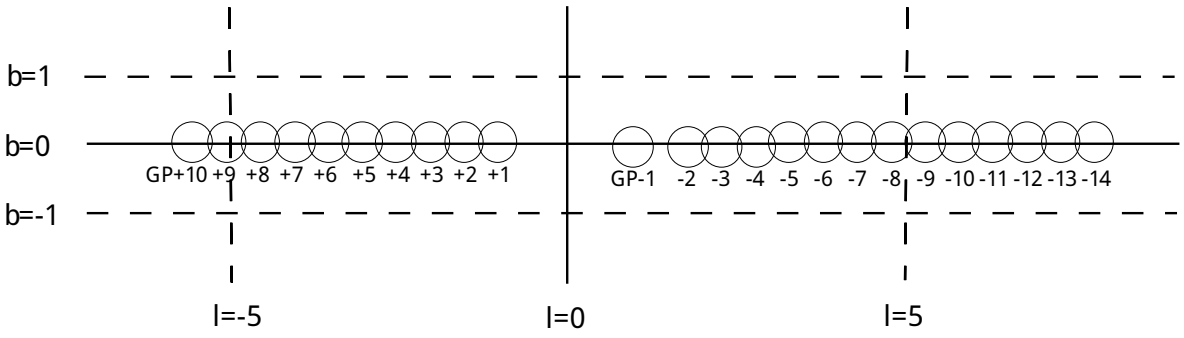

Figure 3.3: Same as figure 3.1, but for the on-plane mapping.

Table 3.2: Same as table 3.1 but for the on-plane mapping

Field	Field center		Date(UT)	Exposure
	l_{II}(deg)	b_{II}(deg)	dd/mm/yy	ksec
GP−1[a]	-0.996	-0.076	26/09/93	28
GP−2	-1.810	-0.080	25/09/95	10
GP−3	-2.310	-0.076	26/09/95	13
GP−4	-2.813	-0.075	26/09/95	10
GP−14[b]	-7.802	0.008	13/03/96	9
GP−13[b]	-7.307	0.006	14/03/96	10
GP−12[b]	-6.805	0.006	14/03/96	10
GP−11[b]	-6.305	0.004	14/03/96	8
GP−10[b]	-5.806	0.006	15/03/96	10
GP−9[b]	-5.302	0.009	15/03/96	10
GP−8[b]	-4.803	0.007	15/03/96	9
GP−7[b]	-4.305	0.006	16/03/96	10
GP−6[b]	-3.805	0.006	16/03/96	10
GP−5[b]	-3.304	0.007	16/03/96	11
GP+1[b]	0.998	0.003	19/09/96	7
GP+2[b]	1.495	0.009	19/09/96	11
GP+3[b]	1.995	0.008	20/09/96	7
GP+4[b]	2.494	0.005	20/09/96	9
GP+5[b]	2.994	0.006	20/09/96	10
GP+6[b]	3.495	0.007	20/09/96	9
GP+7[b]	3.994	0.010	22/09/96	11
GP+8[b]	4.497	0.007	22/09/96	7
GP+9[b]	4.994	0.012	23/09/96	11
GP+10[b]	5.495	0.007	23/09/96	10

a: This observation was planned as the pointing of the Great Annihilator 1E 1740.7−2942.

b: These observations were performed as the Galactic plane survey project.

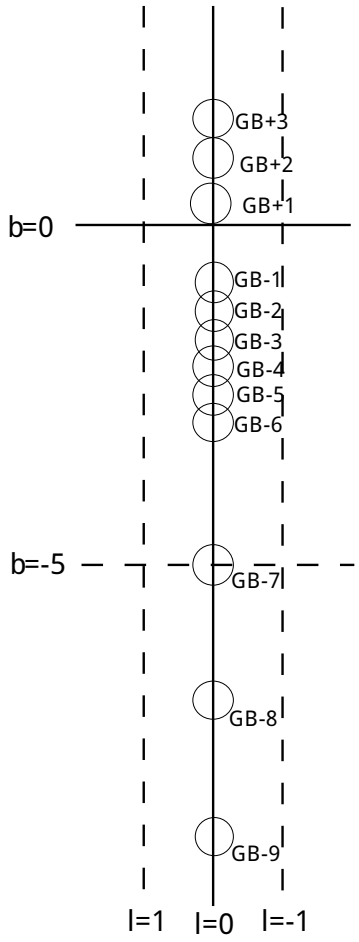

Figure 3.4: Same as figure 3.1, but for the off-plane mapping.

Table 3.3: Same as table 3.1 but for the off-plane mapping

Field	Field center		Date(UT)	Exposure
	l_{II}(deg)	b_{II}(deg)	dd/mm/yy	ksec
GB−1	0.006	−0.841	21/03/95	24
GB−2	0.005	−1.258	22/03/95	25
GB−3	0.007	−1.674	22/03/95	24
GB−9	0.007	−9.006	07/04/96	37
GB+2	−0.027	1.009	10/09/96	13
GB+3	−0.010	1.587	10/09/96	18
GB+1[a]	−0.059	0.341	11/09/96	17
GB−6	−0.004	−2.898	27/09/96	25
GB−5	−0.006	−2.486	28/09/96	27
GB−4	−0.007	−2.070	29/09/96	37
GB−8	−0.006	−6.989	07/10/97	31
GB−7	−0.010	−4.990	08/10/97	38

a: This observation was planned as the pointing of the bursting pulsar GRO J1744−28. Non-standard bits (PH-X-Y-RT-SP-Timing) = (8-8-8-5-0-2) and (8-6-6-5-0-6) were assigned in HIGH- and MEDIUM-bit-rates, respectively.

Table 3.4: Summary of the SIS mode for the off-plane mapping

Field	Bit-rate	Obs. mode	CCD mode[a] SIS0/SIS1
GB−1	HIGH	FAINT	0123/2301
	MEDIUM	BRIGHT	〃 / 〃
GB−2	HIGH	FAINT	〃 / 〃
	MEDIUM	BRIGHT	〃 / 〃
GB−3	HIGH	FAINT	〃 / 〃
	MEDIUM	BRIGHT	〃 / 〃
GB−9	HIGH	FAINT	〃 / 〃
	MEDIUM	BRIGHT	〃 / 〃
GB+2	HIGH	FAINT	〃 / 〃
	MEDIUM	BRIGHT	〃 / 〃
GB+3	HIGH	FAINT	〃 / 〃
	MEDIUM	BRIGHT	〃 / 〃
GB+1	HIGH	BRIGHT	1111/3333
	MEDIUM	BRIGHT	〃 / 〃
GB−6	HIGH	FAINT	0123/2301
GB−5	HIGH	FAINT	〃 / 〃
GB−4	HIGH	FAINT	〃 / 〃
GB−8	HIGH	FAINT	1111/2222
	MEDIUM	FAINT	〃 / 〃
GB−7	HIGH	FAINT	〃 / 〃
	MEDIUM	FAINT	〃 / 〃

a : The read-out order of CCD chips. The number 0, 1, 2 and 3 are abbreviations for Chip0, Chip1, Chip2 and Chip3, respectively.

Table 3.5: Same as table 3.1 but for the Sgr A monitor

Field	Field center		Date(UT)	Exposure
	l_{II}(deg)	b_{II}(deg)	dd/mm/yy	ksec
SgrA94	0.010	−0.058	15/09/94	74
SgrA97[a]	−0.042	0.077	16/03/97	70

a: Non-standard bit (PH-X-Y-RT-SP-Timing) = (10-8-8-0-0-5) was assigned in HIGH-bit-rate.

Table 3.6: Same as table 3.4 but for the Sgr A monitor

Field	Bit-rate	Obs. mode	CCD mode
			SIS0/SIS1
SgrA94	HIGH	BRIGHT	0123/2301
	MEDIUM	BRIGHT	〃 / 〃
SgrA97	HIGH	FAINT	〃 / 〃
	MEDIUM	FAINT	0000/2222

Chapter 4

Mapping of the Galactic Center Region

4.1 Introduction

X-ray observations of the Galactic Center region have been made with several instruments. In spite of extensive observations, direct evidence for high-energy activities of the Galactic center, such as observed in active galactic nuclei (AGN), is still lacking. However, *Ginga*, having detected Kα-lines from highly ionized iron, found a large amount of hot plasma which strongly concentrates towards the Galactic center ([51]; [108]). Koyama et al. (1989 [51]) suggested this thin hot plasma is attribute to a shock-heated interstellar medium by an energetic explosion.

In Koyama et al. (1996 [52] hereafter Paper I), we obtained detailed X-ray image and spectrum of the Galactic Center region up to 10 keV for the first time with *ASCA*. Diffuse thermal emission with distinct Kα lines from highly ionized ions of various elements confirms the presence of extended high-temperature plasma. Fluorescent X-ray emission from cold iron atoms in molecular clouds was also found. The results suggest that the Galactic center exhibited the high energy activities. In this chapter, we reported the SIS results about 1 square degree of the Galactic Center region based on the results in Paper I ([52]). The GIS results are given in the chapter 5.

4.2 Analysis & Results

As summarized in session 3.2, the mapping observation of the Galactic Center region covered one square degree with eight successive exposures of about 20 ksec each. Standard data-selection and -screening criteria were applied to the SIS data, removing data taken at low Earth elevation angles and during times of high particle background. Only the data with 0, 2, 3 and 4 grade were used for our analysis. We applied no RDD correction for all the SIS data,

4.2.1 Broad Energy-Band Maps

We made the mosaic image of the SIS instrument, covering about $1^\circ \times 1^\circ$. We show the SIS image with the 0.7–10 keV band in figure 4.1. We see several bright spots as well as extended emissions (figure 4.1). Three bright spots are found to be point-like, which are identified with AX J1745.6−2901, A 1742−294 and 1E 1743.1−2843 (figure 4.1). Details of the X-ray properties for the three sources observed with *ASCA* are separately given in chapter 6 for AX J1745.6−2901 and [91] for A 1742−294 and 1E 1743.1−2843. We also found that an oval-shaped region of $2' \times 3'$ around the Galactic center Sgr A* is distinctly bright, a factor of about 5 brighter than the surrounding region. Even at the edge of our observed region, we found excess diffuse emission above the background level. Note that the X-ray photons detected in these observations are dominated by the diffuse emission. After the contributions of these three point-like sources were removed, we again made the mosaic images in the soft (0.5–1.7 keV) and hard band (4.0–5.5 keV), which are shown in figure 4.2. The soft band covers the energy range of the soft X-ray telescopes *Einstein* Observatory and *ROSAT*. Several discrete sources found with the *Einstein* Observatory and *ROSAT*, including RX J1745.6−2900, were then detected in the soft band. On the other hand, the image in the hard band, which covers the hard X-ray continuum with no emission lines, appears entirely different from the soft band (figure 4.2). After removing the contribution of nearby point-like source AX J1745.6−2901, we can see that a bright ridge appears to extend from Sgr A* (figure 4.2).

4.2.2 Averaged Diffuse X-ray Spectrum

For each field, we made the diffuse X-ray spectrum (SIS0+SIS1) from the region of four CCD chips ($\sim 22' \times 22'$) after appropriate gain corrections for the two SIS detectors, SIS0 and SIS1. The contamination by nearby bright X-ray sources were removed. These contaminated X-rays are at most 10% of the diffuse X-rays. The backgrounds were subtracted by a method given in appendix A. We used an ancillary response assumed a constant spectrum and brightness within the field of view. Therefore the used ancillary response did not include the stray-light effect. Figure 4.3 shows the averaged SIS spectrum of the diffuse emission over the entire $\sim$1 square degree field. Its spectrum seems to contain many emission lines. We then have determined the line energy, width, equivalent width and surface brightness by fitting. For iron Kα-lines, we used a model of three Gaussian lines and an absorbed power-law to the data in 4.5–10 keV band. For Kα-lines of silicon, sulphur, argon and calcium, we used a separate model of eight Gaussian lines and an absorbed power-law to the data in 1.5–5 keV band. The line energy, surface brightness and equivalent width are summarized in table 4.1. The observed lines are identified with Kα-lines from helium-like (He-like) and hydrogen-like (H-like) ions of silicon, sulphur, argon, calcium, and iron. For each element, the fluxes of the Kα-lines from helium-like ions were found to be brighter than those from hydrogen-like ions. These highly ionized ions are likely from the hot gas discovered with *Ginga* ([51]; [108]). In addition, a significant 6.4-keV iron line due to fluorescent X-ray emission from neutral atoms or ions below XVII (Na-like) is present.

In the fitting to iron Kα-lines, we set the line widths for the Kα-lines from He-like (~ 6.7 keV) and H-like ions (~ 6.97 keV) to the same value because of the limited statistics. Therefore we determined the line widths of the Fe 6.4-keV and Fe He,H-like lines. We show confidence contours of the two line widths in figure 4.4. While the line width of the 6.4-keV line is consistent to be narrow, the other two lines are found to be significantly broadened ($\sigma \approx 80$ eV). Due to the limited statistics, we also set the line widths for silicon, sulphur, argon and calcium to the same value, but allowed to be free. We found the best-fit value of the line width σ to be 34 ± 4 eV. However, this broadening is less certain.

4.2.3 Line Distributions

We separately extracted the diffuse X-ray spectra from the eight observed fields. The spectra in arbitrary unit are given in figure 4.5. Although the flux and spectral shape vary from field to field, all the spectra contain the emission lines listed in table 4.1. In order to determine line parameters (energy, surface brightness and equivalent width) from the eight observed fields, we fitted these spectra with the same models as used in the above section. For simplicity, we fixed the line widths to be 60 eV for the three iron Kα-lines and 40 eV for the others.

Figure 4.6 shows the surface brightness of the four luminous lines: Kα-lines from He-like and H-like ions of both sulphur and iron. The surface brightness of the four lines varies from field to field, but the H-like/He-like flux-ratios of sulphur and iron Kα-lines are roughly constant. In figure 4.7, we plotted the surface brightness of the two luminous lines: Fe 6.4-keV and Fe He-like Kα-lines. Although the surface brightness of the two lines varies from field to field, the flux-ratio of the two lines is roughly constant except for the GC2 field. In figure 4.8, we also plotted the equivalent widths of the five luminous lines: Si He-like, S He-like, Fe 6.4-keV, Fe He-like and Fe H-like Kα-lines. The equivalent widths are roughly constant from place to place, except for the 6.4-keV line. Only the 6.4 keV line shows the large equivalent width in the GC2 field.

4.2.4 Narrow Energy-Band Maps

In order to research detailed line-distribution, we made narrow energy-band maps with the center energies at three luminous emission-lines: S He-like, Fe He-like and Fe 6.4-keV line. We show the narrow energy-band maps in figures 4.9 & 4.10 after removing contributions of these three point-like sources AX J1745.6$-$2901, A 1742$-$294 and 1E 1743.1$-$2843. The S He-like and Fe He-like lines have a bright spot around Sgr A* (figure 4.9). The Fe He-like line is symmetrically extending along the Galactic plane on either side of Sgr A*, while the spatial distribution of the He-like sulphur is highly asymmetric. The 6.4-keV line-map appears entirely different from the former two maps (figure 4.10). There are two bright regions; the brightest region lies near the prominent molecular cloud, Sgr B2 and the other bright region is located between Sgr A* and the Radio Arc, which is also associated with another dense molecular cloud "50 km s^{-1} cloud" ([57]; [105]). For comparison,

we show the velocity-averaged molecular line-maps of CS $J = 1 \rightarrow 0$ in figure E.1. Since the GC2 field contains the Sgr B2 region, the large equivalent width detected in the GC2 field is mainly due to this intense 6.4-keV line from the Sgr B2 region. Note that there is no bright region around Sgr A* in the 6.4 keV map.

4.2.5 Sgr B2

The Sgr B2 region is remarkably bright in the iron 6.4-keV line-map (figure 4.10). We then made the spectrum taken from a $\sim 3'.6$ radius circular region near Sgr B2. We show the observed spectrum near the Sgr B2 region in figure 4.11. The observed spectrum exhibits the three iron Kα-lines as detected over the entire $\sim$1 square degree field. The equivalent widths of the iron He-like and H-like lines are about 510$\pm$190 and 200$\pm$170 eV, respectively (table 4.2), which are the same to those in the spectrum averaged over the entire $\sim$1 square degree field within the errors (see table 4.1). However the equivalent width of the 6.4-keV line is 890$\pm$220 eV, which is about 5 times larger than that in the averaged spectrum. Therefore, we confirmed that the iron 6.4-keV line in the Sgr B2 region is extremely luminous in the entire $\sim$1 square degree field. The observed flux of the 6.4-keV line near the Sgr B2 region was found to be 1.1×10^{-4} photons cm^{-2} s^{-1}.

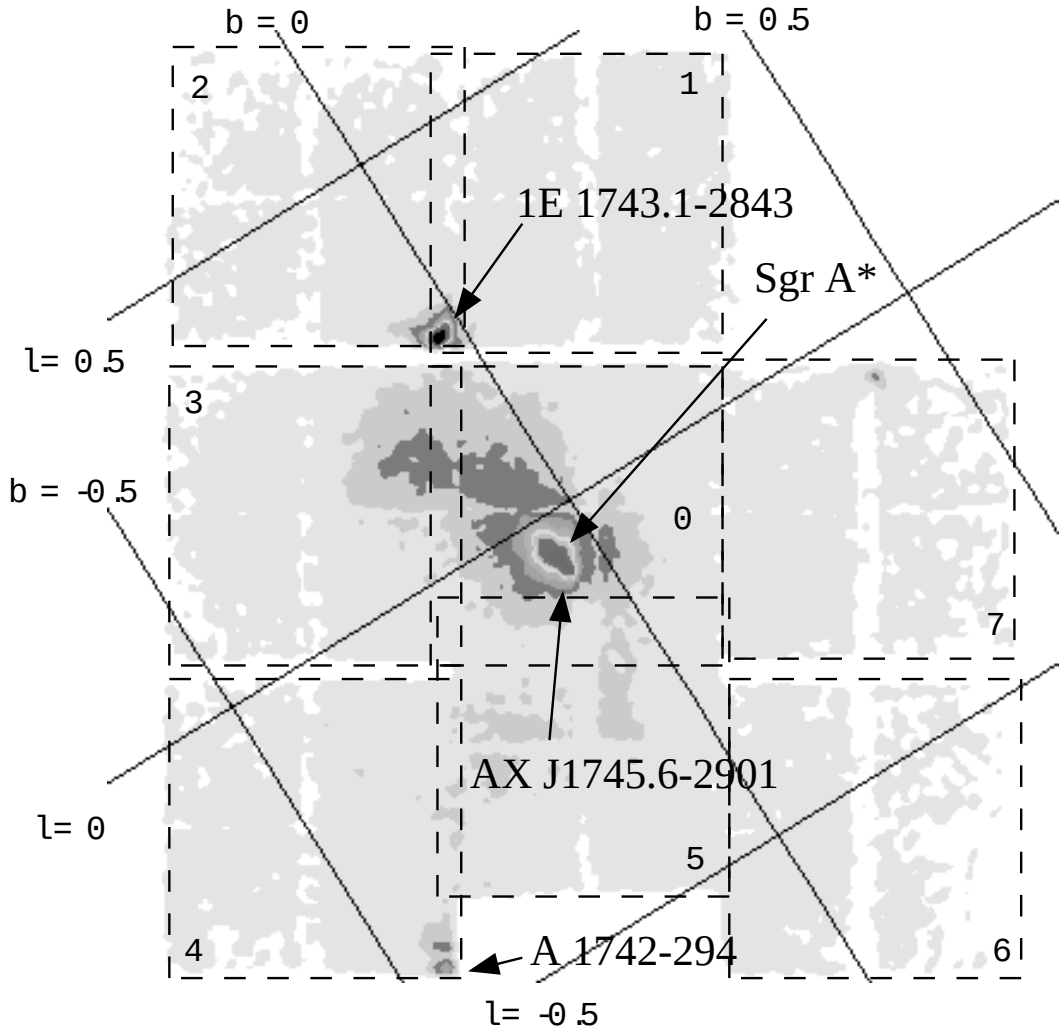

Figure 4.1: The SIS image with the 0.7–10.0 keV band (a mosaic of X-ray images of eight adjacent fields). Numbers show eight consecutively observed GC-series field. A Chris-cross structure is the gap of each CCD chip (one CCD camera consists of four adjacent CCD chips). No correlation of the non-uniform efficiency over the detector field was made on the images. See also Plate I.

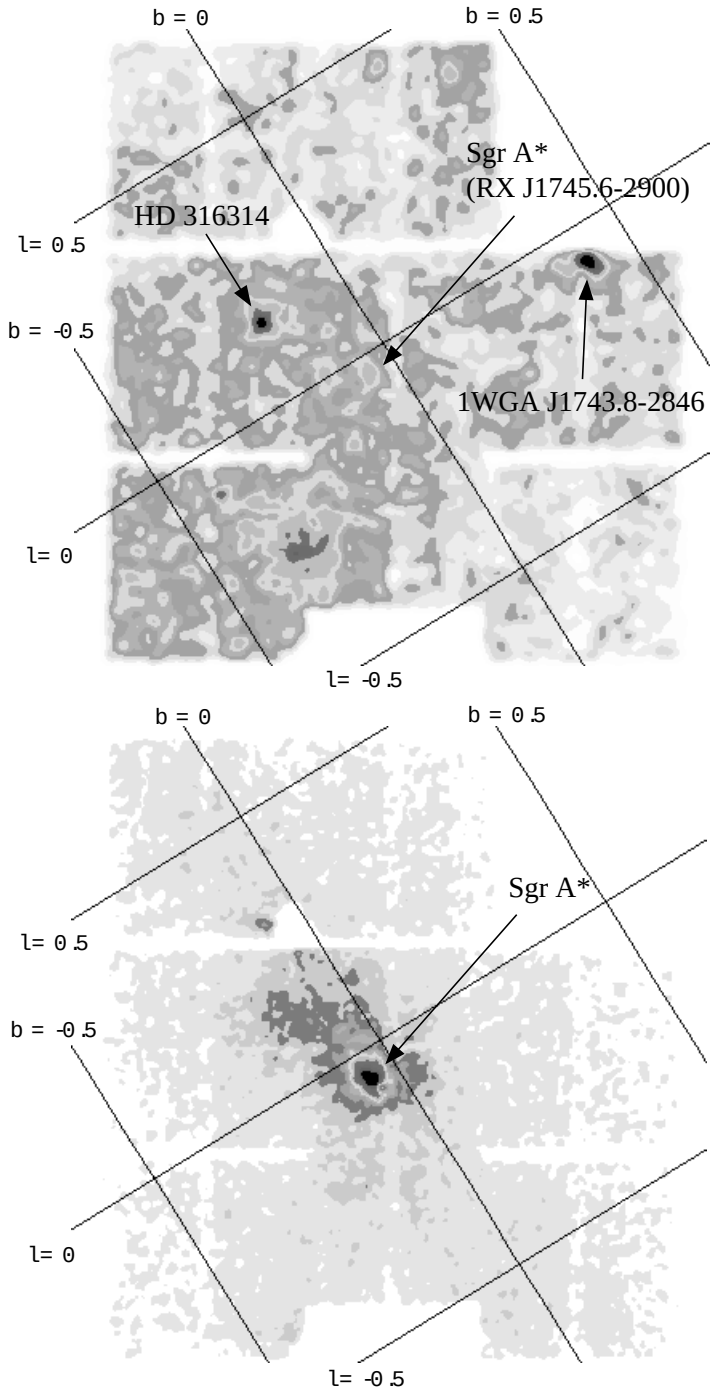

Figure 4.2: Same as figure 4.1, but after removing three bright sources, for soft (upper panel) and hard (lower panel) band images, respectively. The soft and hard bands correspond to the 0.5–1.7 and 4.0–5.5 keV bands, respectively.

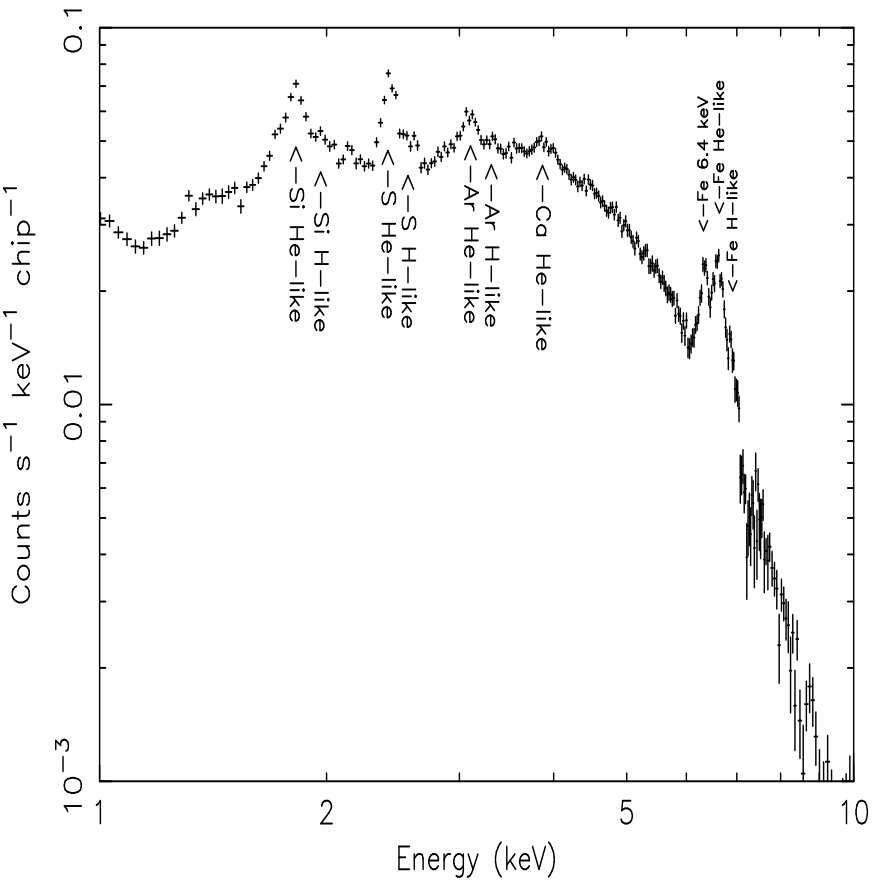

Figure 4.3: The SIS spectrum of diffuse emission (average of spectra of all the eight fields after excluding spectra of the three luminous X-ray binaries). Luminous emission lines are identified with Kα-lines from He-like and H-like ions of silicon, sulphur, argon, calcium, and iron. A significant 6.4-keV iron line, a fluorescent line from neutral atoms or ions below XVII, is also present. See also table 4.1. Error bars are 1σ level.

Table 4.1: Line energies, surface brightness and equivalent widths in the averaged diffuse X-ray spectrum

——Observed line——			——-Identification——-	
Line energy (keV)	Surface brightness (photons s^{-1} cm^{-2} sr^{-1})	EW[b] (eV)	Line name	Energy (keV)
1.86±0.01	5.0±0.3	120±10	Si He-like Kα	1.86
2.00(fix[a])	1.5±0.2	32±6	Si H-like Kα	2.00
2.45±0.01	7.9±0.4	140±10	S He-like Kα	2.45
2.63(fix[a])	1.9±0.3	33±5	S H-like Kα	2.63
3.14±0.01	2.3±0.3	40±5	Ar He-like Kα	3.14
3.32(fix[a])	0.6±0.3	11±5	Ar H-like Kα	3.32
3.93±0.03	0.8±0.2	15±5	Ca He-like Kα	3.90
4.11(fix[a])	<0.4	<8	Ca H-like Kα	4.11
6.43±0.01	6.5±0.9	170±20	Fe Neutral$\sim$Ne-like Kα	6.4
6.71±0.01	14.1±1.0	390±30	Fe He-like Kα	6.7
7.00±0.02	7.1±0.7	200±20	Fe H-like Kα	6.97

Surface brightness in the 2–4 and 2–10 keV band is 6.2×10^{-7} and 3.2×10^{-6} erg s^{-1} cm^{-2} sr^{-1}, respectively. Errors are 90% level.

a: Line energy is fixed to the theoretically predicted value because of the limited statistics.

b: EW is abbreviation for equivalent width.

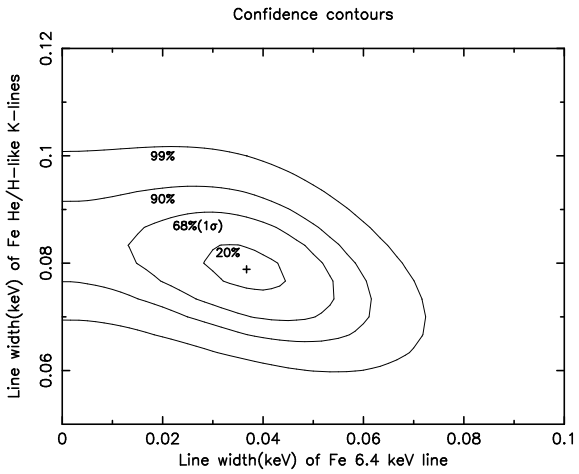

Figure 4.4: Confidence contours of the line width σ of the Fe 6.4-keV line and Fe He/H-like Kα-lines. Contours (from inner to outer) represent 20%, 68%, 90% and 99% confidence levels, respectively. The cross indicates the best-fit solution.

Table 4.2: Iron line energies, fluxes and equivalent widths in the Sgr B2 spectrum

——Emission lines——				
(——Observed line——)			(——-Identification——-)	
Line energy	Flux	EW[b]	Line name	Line energy
(keV)	(photons s^{-1} cm^{-2})	(eV)		(keV)
6.41±0.02	$1.1\pm0.2\times10^{-4}$	890±220	Fe Neutral∼Ne-like Kα	6.4
6.69±0.04	$6.2\pm1.9\times10^{-5}$	510±190	Fe He-like Kα	6.7
6.97(fix[a])	$2.4\pm1.8\times10^{-5}$	200±170	Fe H-like Kα	6.97
——Continuum——				
$N_{\rm H}$ (H cm^{-2})		$2.6(1.6–3.8)\times10^{23}$		
Photon index (γ)		1.6(0.7–2.6)		
$F_{\rm x}$(4.5–10 keV) (erg s^{-1} cm^{-2})		6×10^{-12}		
χ^2(d.o.f.)		22.74(27)		

The spectrum was taken from a ∼3′.6 radius circular region. Errors are 90% level.

a: Line energy is fixed to the theoretically predicted value because of the limited statistics.

b: EW is abbreviation for equivalent width.

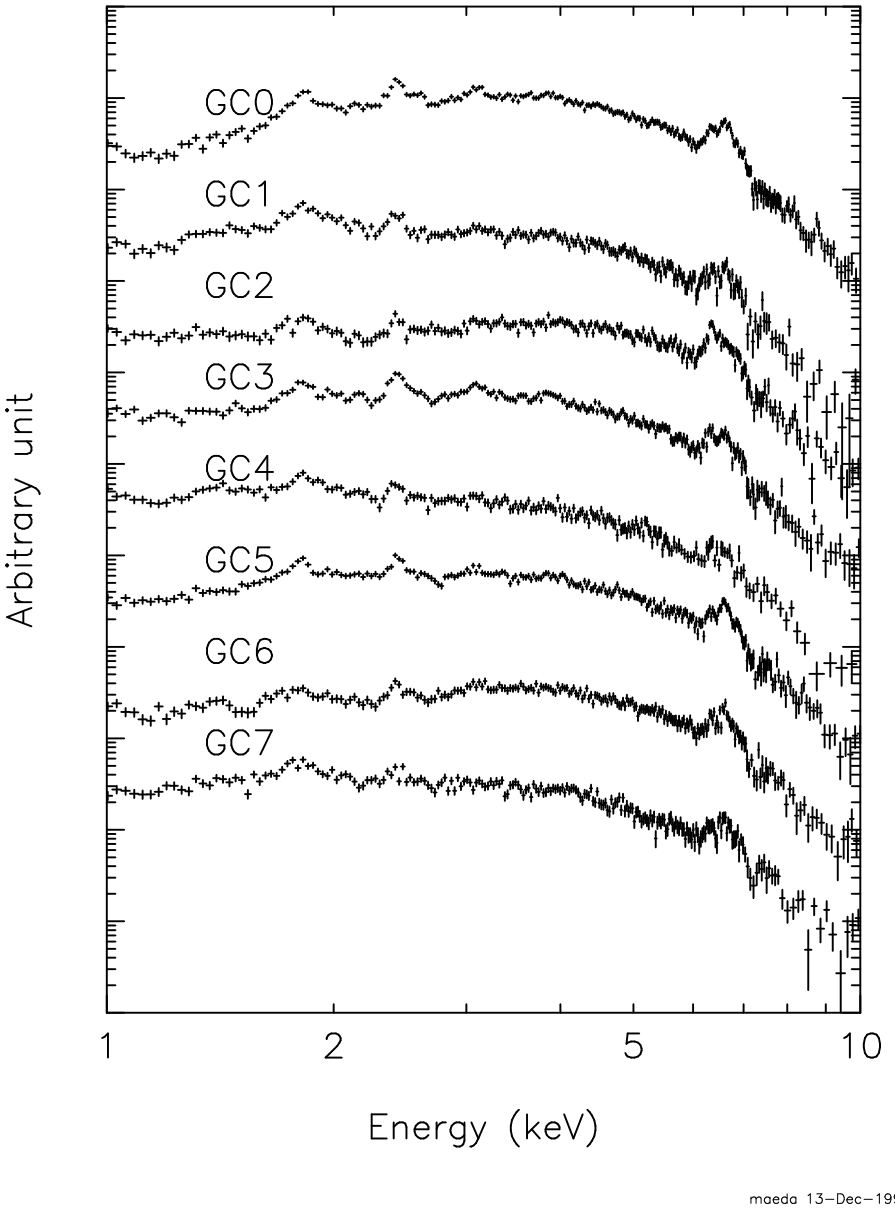

Figure 4.5: SIS spectra obtained at each GC-series observation. All the spectra were averaged over four CCD chips for the two SIS detectors, SIS0 and SIS1. The SIS internal background was subtracted while the cosmic X-ray background is included (see appendix A for detail). Error bars are 1 σ.

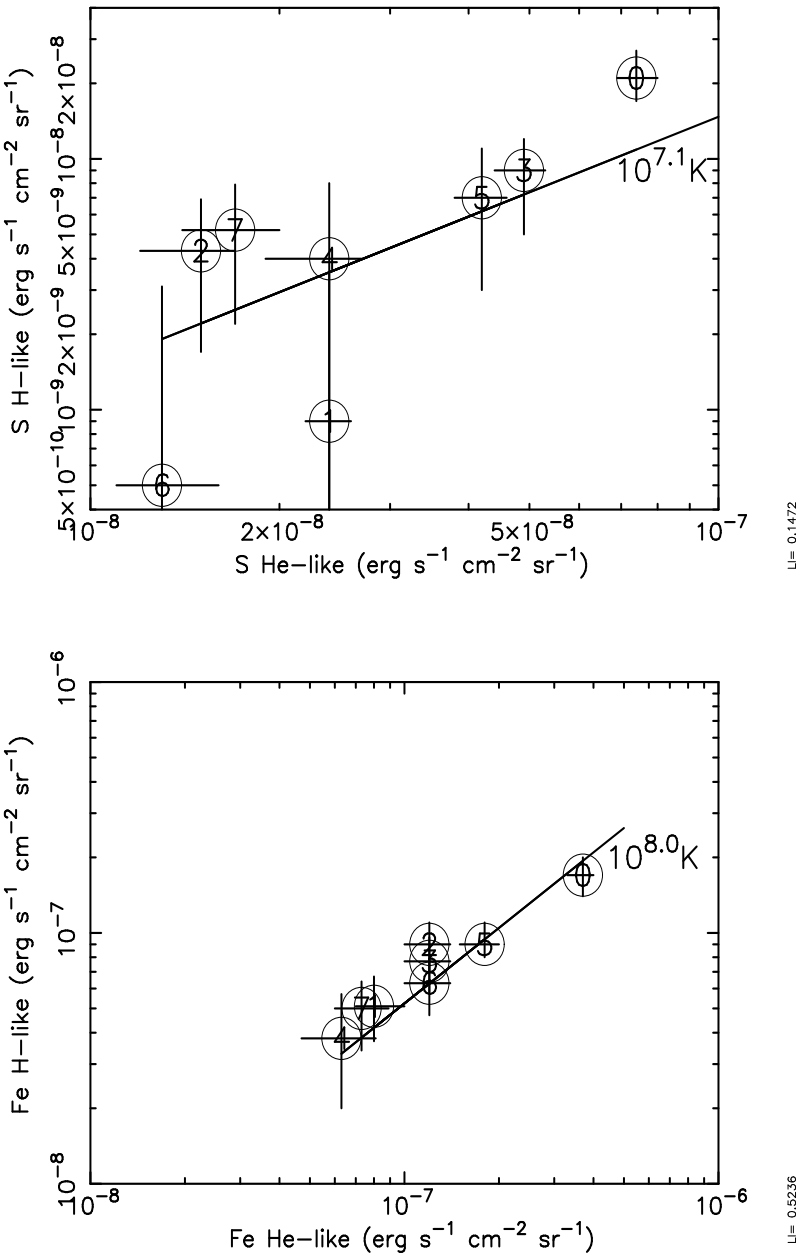

Figure 4.6: Correlations between surface brightness of the two Kα-lines from He-like and H-like ions of sulphur (upper panel) and iron (bottom panel) at each observed field, respectively. Numbers of observed fields correspond to the numbers of figure 4.1. The solid lines mean the line-ratios of $kT = 10^{7.1}$ (upper) and $10^{8.0}$K (lower) calculated from the plasma model in ionization-equilibrium ([68]). Error bars are 90%.

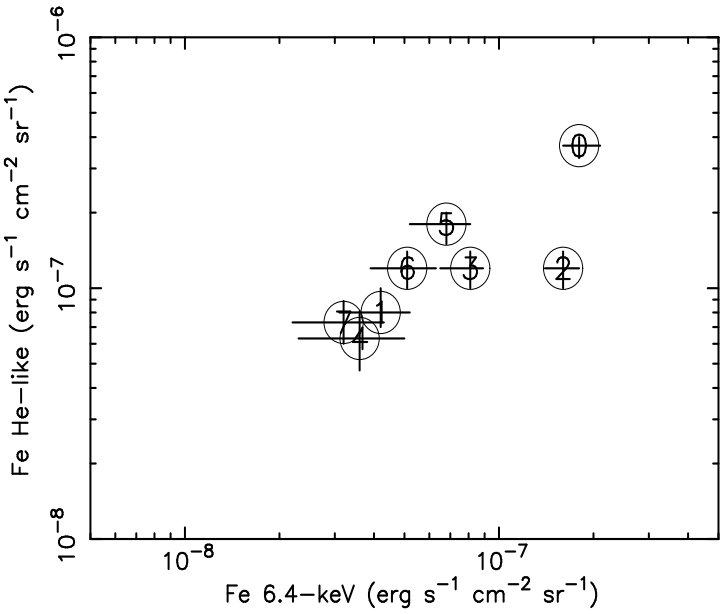

Figure 4.7: Correlations between surface brightness of the Fe 6.4-keV and Fe 6.7-keV (He-like) at each observed field. Numbers of observed regions correspond to the numbers of figure 4.1. Error bars are 90%.

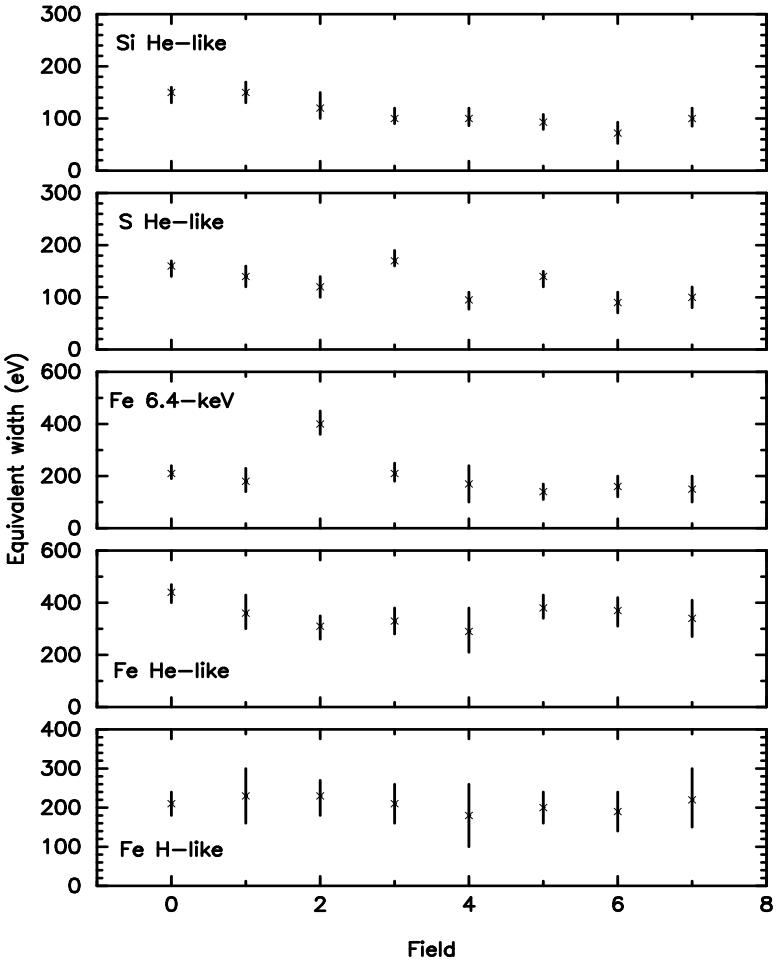

Figure 4.8: Field distributions of the line-equivalent widths of the luminous Kα-lines: Si He-like, S He-like, Fe 6.4-keV, Fe He-like and Fe H-like Kα-lines. Numbers correspond to the numbers of figure 4.1. Error bars are 90%.

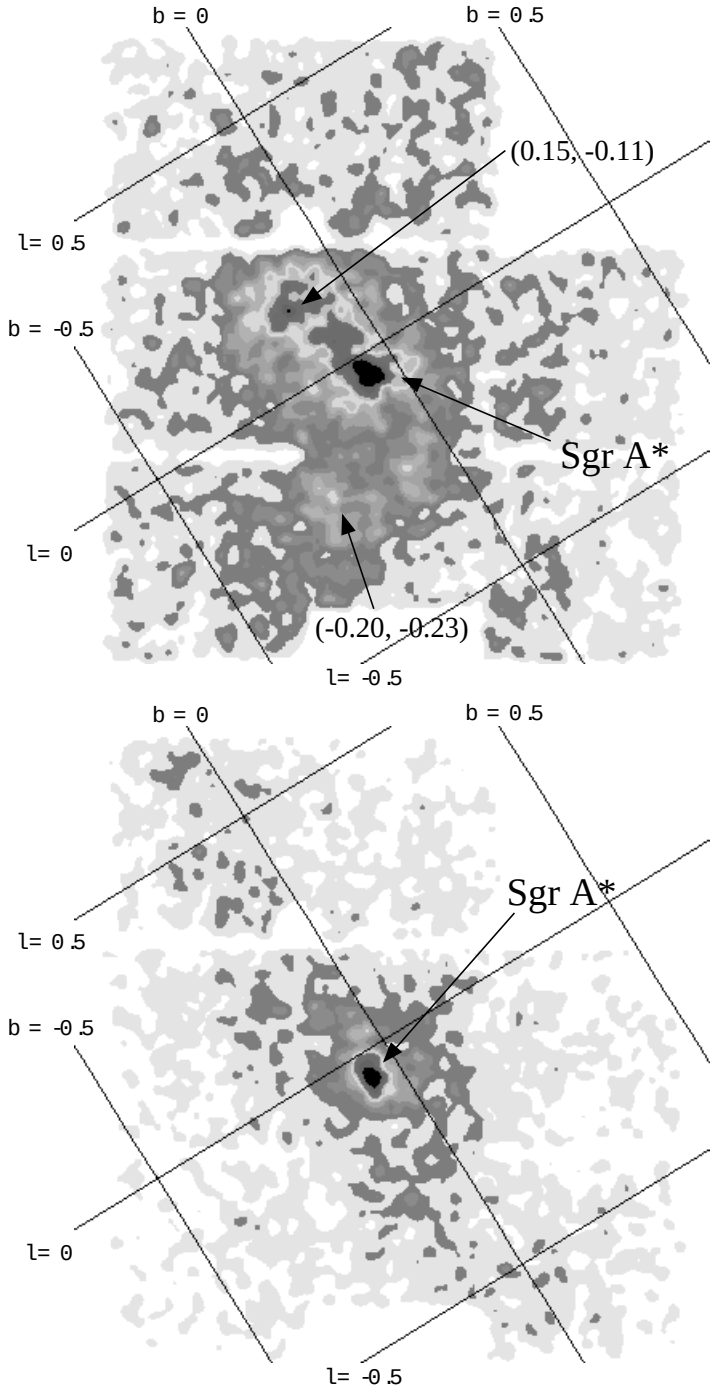

Figure 4.9: Images of narrow band-energy with the center energy at two luminous emission-lines: He-like sulphur (upper panel), He-like iron (bottom panel). In the He-like sulphur and He-like iron line-maps, there is a bright spot around Sgr A*. Only the iron He-like line exhibits a symmetric distribution along the Galactic plane. Neither correlation of the non-uniform efficiency over the detector field nor background-subtraction was made on the images.

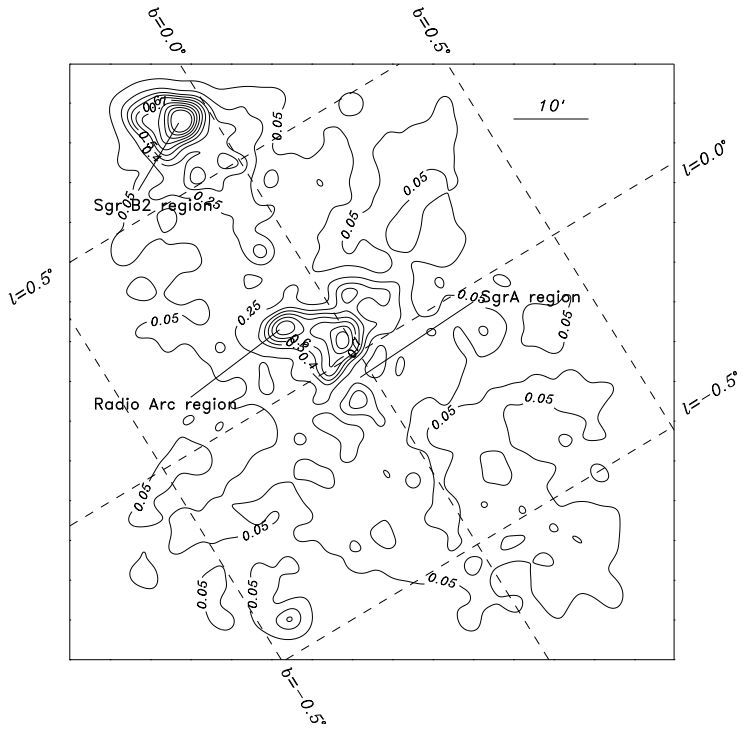

Figure 4.10: Brightness-distribution of the iron 6.4-keV line. In the iron 6.4-keV line-map, there are two bright regions. One is northern bright spot (upper-left), which is located near the Sgr B2 cloud. The other (middle) between Sgr A* and the Radio Arc appears to be associated with another dense molecular cloud. No correlation of the non-uniform efficiency over the detector field was made on the images. This map is produced in the energy-band of 6.3 - 6.5 keV, and subtracting the continuum in this band. See also Plate I.

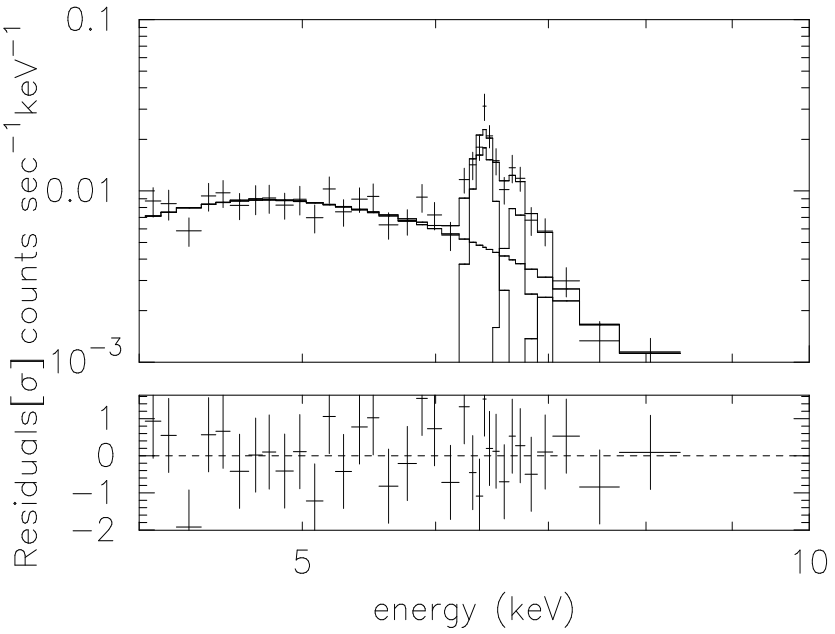

Figure 4.11: The SIS spectrum of Sgr B2. Error bars are 1 σ. The solid line corresponds to the best-fit value with the model of three Gaussian lines and an absorbed power-law to the data in the 4.5–10 keV band. Fit residuals are shown at the bottom of each panel.

Chapter 5

Large-Scale Mapping around the Galactic Center

5.1 Introduction

Using the *Ginga* satellite, Yamauchi et al. (1990 [108]) found the iron 6.7-keV line with an elliptical shape of 1×1.8 degree (FWHM) and inclination of about 20 degree near the Galactic Center. The 6.7-keV line is associated with the extended high temperature (∼10keV) plasma. The 6.7-keV iron line emission was also found to largely extend along the Galactic plane ([50];[109];[43]), which is called "the Galactic ridge X-ray emission (GRXE)" ([115]). Yamauchi & Koyama (1993 [109]) determined the scale height to be 100±20 pc. They also discovered another diffuse emission feature with the scale height of more than 750 pc, whose 2–10 keV luminosity is about $(2.8\pm0.8)\times10^{36}$ erg s^{-1}.

Snowden et al. (1997 [96]) presented maps of the soft X-ray background in the 0.1–2.0 keV range derived from the *ROSAT* all-sky survey (RASS) data. They found the diffuse soft X-ray emission with a radial extent of ∼5.6 kpc along the Galactic plane. The X-ray emitting gas has a scale height of 1.9 kpc, where the typical temperature is estimated to be ∼0.34 keV using the soft X-ray color.

The *ASCA* satellite has the capability to observe these diffuse emission with a reasonable high energy resolution to resolve the emission lines, which often provide key information for the origin of the X-rays. *ASCA* also has the broad-band sensitivity from ∼0.7 to ∼10 keV, which is suitable to detect the plasma with the temperature both of 0.34 and 10 keV. Through this chapter, we give constraint

on the shape of the high temperature plasma near the Galactic Center. We also report the largely extended high temperature plasma over the Galactic Center. The successful *ASCA* study of the Galactic ridge emission away from the Galactic Center have been already performed by Kaneda (1997 [43]). Therefore we limited the observed region up to 10 degree from the Galactic Center. In this chapter, we used only the GIS data because the SIS data were degraded by the radiation damage.

5.2 GIS Images & Findings of Discrete Sources

In Plate III, we show GIS mosaic images of the Chris-cross mapping. These images consist of two contour maps for the energy bands of 0.7–3 and 3–10 keV. Individual images obtained with GIS2 and GIS3 have been synthesized into a mosaic map. Many bright discrete sources, in addition to the diffuse X-ray emission, are seen in the images.

band.

If discrete sources is located in the observed field, the data should include the event not only from the diffuse emission but also from the discrete sources. If the discrete source is relatively bright in the observed field, the spill-over X-rays from these sources significantly contaminate the diffuse X-rays. In order to estimate the spill-over X-rays from the discrete sources, we gave a following procedure to find discrete sources included in a field. We made images with the 0.7–3 keV and 3–10 keV bands for each observation. We smoothed the images by the Gaussian function with appropriate widths (from $0'.38$ to $0'.75$) and found peak positions for source candidates. In order to test the significance of the source detection, we specified a source box-region with the half-size of $2'$ centered at the peak position and counted the number of events within the specified box. The background was estimated from a region within two boxes centered on the peak, whose inner and outer boxes had half-sizes of $3'$ and $5'$, respectively. We also counted the number of events within the background boxes and compared them to the counts from the source box-region. We repeated this process for all the areas of the GIS2 and GIS3 fields independently. However, if the discrete sources exhibit much brighter X-rays than the diffuse emission, the source made sharp tails due to the point spread function with Maltese-cross shape (figure 2.6). If we applied our above methods, the tails

often showed highly significant detections. Therefore we ignored source-detections with smaller significance ($\leq 10\ \sigma$) in the field where brighter sources (≥ 1 count s^{-1} GIS^{-1}) were detected in the same fields ; GP$-$1(1E 1740.7$-$2942), GP$-$10(GX 354$-$0), GB+1(GRO J1744$-$28). The stray lights from the bright sources were located near but outside the observed field, i.e. GX 3+1, GX 5$-$1, GRS 1739$-$278 and A 1742$-$294, formed a quasi diffuse X-rays with dappled structures (figure 2.8), which were also regarded as the discrete sources with high significance. Therefore we also ignored the source-detections ($\leq 10\ \sigma$) in the field where the stray lights were remarkably seen in the images ; Fields GP+1$\sim$5(GX 3+1), GP+8$\sim$10(GX 5$-$1), GP$-$7$\sim$11(GX 354$-$0), GB+2$\sim$3(GRS 1739$-$278), GB$-$1$\sim$2(A 1742$-$294). We listed the positions of the source candidates with more than 4.5σ excess both in the GIS2 and GIS3 detectors in table 5.1.

All the brighter sources listed in table 5.1 were confirmed to be LMXBs or LMXB candidates. On the contrary to the brighter source, the fainter sources contain non-degenerated Galactic objects, i.e. #12, #17, #18. These sources were often detected only in the 0.7–3 keV band (soft band). The soft source #15, which was faintest among the sources detected near the Galactic Center, exhibited 0.013 counts s^{-1} $GIS2^{-1}$ (0.7–3 keV) with 6 σ significance. The faintest source #20 (table 5.1) was detected from the GB$-$9 field in the two energy bands both with $\sim 5\ \sigma$ significance. The count rates of this source were found to be 0.0031 counts s^{-1} $GIS2^{-1}$ (0.7–3 keV) and 0.0035 counts s^{-1} $GIS2^{-1}$ (3–10 keV), respectively. Therefore the lower limit of the source detection in the GB$-$9 field was estimated to be about 0.003 counts s^{-1} GIS^{-1} both in the 0.7–3 and 3–10 keV bands. However the lower detection-limit varied from field to field, which depends on the exposure time and the intensity of the diffuse emission. The lower limit in the field near the Galactic Center is estimated to be roughly ten times larger than that in the GB$-$9 field. The detailed studies of the discrete sources were developed and reported by [91] & [67].

5.3 Diffuse X-ray Spectra

We made GIS X-ray spectra from the circular regions of $17'.5$ radii for each GP- and GB-series observation (see chapter 3), which are the same regions used in [43] & [44]. Only for each GC-series observation, we created the spectra using the

smaller radii of 13′ in order to reduce the spill-over X-rays from the bright LMXBs 1E 1743.1−2843 and A 1742−294 which were often detected in the edge of GIS in the GC-series observations. The backgrounds were subtracted by a method given in appendix B. We used an ancillary response assumed a constant spectrum and brightness within an angular extent of 1°.5. Therefore the used ancillary response included the stray-light effect. We show 26 representative X-ray spectra of the individual fields in figures 5.1–5.3. From these representative X-ray spectra, we calculated the X-ray count rates in the energy bands of 0.7–3 keV and 3–10 keV. We show a field-to-field variation of these count rates in figure 5.4. The hardness ratios of 3–10 keV to 0.7–3 keV are also shown in figure 5.5.

As is given in figure 5.4, we detected the significant X-ray emission from all the observed fields. Therefore we confirmed the presence of the diffuse emission around the Galactic Center (the Galactic ridge emission ; e.q., [109]). The inner ∼1° region of the Galactic Center exhibits largest count rates both in the two energy bands. Along the Galactic plane, the count rate decreases slowly (∼1/5 at $|l|$ =2°) in the 0.7–3 keV band and rapidly (∼1/10 at $|l|$ =2°) in the 3–10 keV band (figure 5.4). The decreases were found to become dull around $|l| = 2°$–3° and confirmed to become roughly flat in $|l| > 2°$–3° both in the 0.7–3 and 3–10 keV bands ([43]). The spectra become the hardest in the Galactic Center (figure 5.5). As is shown in figure 5.1, the GC2 & GC6 spectra in the Galactic Center region show a peak around 3–4 keV, which indicates the low-energy cut-off by a large interstellar absorption. Therefore the spectral hardness detected in the GC-series fields is mainly due to the large interstellar absorption near the Galactic Center (cf. [91]). In spite of the spectral hardness, the inner ∼1° region also shows a brightest peak in the 0.7–3 keV band. The Galactic Center was then found to emit the more luminous diffuse emission both in the 0.7–3 keV and 3–10 keV bands than the surrounding region.

The latitudinal distributions of the count rates and the spectral hardness show more complexity than the longitudinal. The count rate in the 0.7–3 keV band has double peaks near $b = 0°$ and −1°.5. The first peak near $b = 0°$ is due to the luminous Galactic Center emission as already discussed in this session. As is shown in figure 5.1, the X-ray emission around 1 keV was seen in the spectra at $|b| > 1°$ (GB−2 ∼ −9), which indicates the decreasing of the low-energy cut-off. Therefore, the second peak near b= −1°.5 is inferred to be mainly due to a rapid decrease

of the interstellar absorption perpendicular to the Galactic plane (cf. [91]). The count rate of the 0.7–3 keV band shows a slow decrease from $|b| \sim -1^\circ.5$ to $\sim 5^\circ$. The significant X-rays were detected up to $|b| = 9^\circ$ in the 0.7–3 keV band, which are about 1/10 of those at the Galactic Center. On the contrary to the 0.7–3 keV band, the count rate in the 3–10 keV band has a single peak at $b = 0^\circ$. The count rate in the 3–10 keV band decreases very rapidly up to $|b| \sim 2^\circ$ and becomes $\sim$1/20 at $|b| = 2^\circ$. The count rate in the 3–10 keV band decreases again from $|b| \sim 2^\circ$ with a slightly duller slope. The count rates in the 3–10 keV band at $b = -7^\circ$ and -9° become less than 1/10 of the CXB level. The latitudinal distribution of the spectral hardness exhibits the stair-like structure (figure 5.5). The spectra exhibit the hardest at the Galactic center ($b = 0^\circ$) and soften the hardness along the latitudinal direction to $|b| \sim 1^\circ$. The spectral hardness becomes nearly constant around $|b| = 2^\circ$. The spectra soften again the hardness from $|b| \sim 4^\circ$ to 9°.

Note that, as is shown in figures 5.1–5.3, all the spectra contain many emission lines. Although the flux and spectral shape vary from field to field, the emission lines contained in the spectra are a common characteristics for the Galactic diffuse emission.

5.4 Line Distributions

Several emission lines, which can provide key information for the origin of the X-rays, were seen in the spectra (figures 5.1–5.3). In this section, we derive line parameters (energy, width, surface brightness and equivalent width) from these spectra. When the bright X-ray sources, listed in the upper parts of table 5.1, were located in or around the observed field, the spectra of the diffuse emission obtained in the field show no clear line feature, which is due to the large contamination by the bright sources. In these contaminated fields, we could determine no line parameter. Therefore, the line parameters in these fields are lacking in the later session. Note that all the bright X-ray sources are identified with LMXBs or LMXB candidates, whose spectra show no prominent emission line (cf. [69]). Generally speaking, spill-over or stray X-rays contaminate the continuum level of the diffuse X-ray spectra.

5.4.1 Iron-Broad-Line Model

For each field, we determined the observed line energy, width, surface brightness of the iron line by fitting a model of a single Gaussian line and an absorbed thermal bremsstrahlung to the data in 3.5–9 keV band. All the line parameters (line energy, width and surface brightness) of the Gaussian function were free. We summarized the best-fit parameters in table C.1. In figure 5.6, we plotted the line energy, width and surface brightness as a function of an angle from $(l, b) = (0,0)$ along the longitudinal and latitudinal directions, respectively.

As is given in figure 5.6, the significant iron Kα-line was detected in each field, except for the GB$-8(b = -7^\circ)$ and GB$-9(-9^\circ)$ observations. The iron Kα-line at each field shows a line energy of about 6.6 keV, which corresponds to the Kα-line from the highly ionized ions of iron. The iron lines detected in each GC-series field show distinct broad line width around 200 eV. As is shown in figure 4.3, the SIS spectra of the Galactic Center field exhibited the three discrete Kα-lines (6.4, 6.7 and 6.97 keV) from field to field. The fluxes both of the 6.4-keV and 6.97-keV line obtained with SIS are roughly $\frac{1}{2}$ of that of the 6.7-keV (He-like) line while the ratio varies from field to field. The observed line width of about 200 eV is also very similar to the difference among the three line energies, i.e., 6.7 keV $-$ 6.4 keV $=$ 300 eV and 6.97 keV $-$ 6.7 keV $=$ 270 eV. Therefore, the broad line-width in the GC-series field obtained with GIS is due to the blend of the three lines. The iron lines outside the Galactic Center region also show broad line widths of about 200 eV with the large errors of $\sim$100–200 eV, which are due to the limited statistics. The iron Kα-lines in these fields are then consistent both with a single narrow line and with a blend of the three narrow lines. Kaneda (1997 [43]) analyzed the averaged SIS spectrum of the Galactic ridge emission, which was made from the observations around $(l, b) = (10^\circ, 0^\circ)$ and $(23^\circ, 0^\circ)$. He found the intense single $\sim$6.6 keV iron line from the averaged SIS spectra. He also found no significant 6.4 and 6.97 keV lines with more than 99% confidence. Therefore the multi iron Kα-lines (6.4+6.7+6.97 keV) were inferred to be plausible for the spectra near the Galactic Center, while the single iron Kα-line with the moderate narrow width was plausible for the spectra away from the Galactic Center.

5.4.2 Double Iron-Line Model

Although the iron line outside the GC-series field is not clear whether it is blended or not, we determined the observed surface brightness and equivalent widths of the iron lines by fitting a model of two Gaussian lines and an absorbed thermal bremsstrahlung to the data in 3.5–9 keV band. Due to the limited energy resolution, we fixed the line energies to 6.4 keV and 6.7 keV. Both line widths were fixed to zero. We summarized the best-fit parameters in tables C.2 & C.3. In figure 5.7, we plotted the surface brightness as a function of an angle from $(l, b) = (0,0)$ along the longitudinal and latitudinal directions. In figures 5.8 & 5.9, we also plotted the line-equivalent width, electron temperature, emission measure and absorption column using the data obtained in the less-contaminated field where the contaminated X-rays (3–10 keV band) by the discrete sources occupied at most $\sim$10% of those from the diffuse emission itself.

We fitted the surface brightness S as a function of an angle θ from (l, b)=(0,0) (figure 5.7) with a double exponential-decay model given by

$$S(\theta) = S_1 \exp(-\frac{|\theta|}{\omega_1}) + S_2 \exp(-\frac{|\theta|}{\omega_2}), \tag{5.1}$$

where $S_{1,\ 2}$ and $\omega_{1,\ 2}$ are surface brightness at (l, b)=(0,0) and scale lengths in unit of degree, respectively. The best-fit results were given in figure 5.7 and table 5.2. The surface brightness both of the two iron Kα-lines decreases rapidly near the Galactic Center and decreases slowly away from the Galactic Center (figure 5.7). Since the surface brightness of the 6.4-keV line shows a rough decrease along the Galactic plane, the double exponential-decay model did not reproduce well the brightness distribution with the large χ^2 value of 122.5 (table 5.2). We found two data-points at l = 0°.5 & 3°.5 show large excess from the best-fit model. Note that both of these two fields include the giant molecular clouds, i.e., Sgr B2 and Clump II clouds for l=0°.5 and 3°.5, respectively ([97]). The surface brightness of the 6.4-keV line shows the rapid decrease with the scale length of $\sim$0.17 degree perpendicular to the Galactic plane, which is equivalent to 25 pc at the distance (8.5 kpc) of the Galactic center. The brightness distribution of the 6.7-keV line near the Galactic Center also shows the rapid ($\omega_1 \sim 0°.19$) and slow (0°.42) decreases along the longitudinal and latitudinal directions, respectively. The 6.7-keV line shows the large-scale decreasing of the surface brightness with the scale lengths of ($\omega_2 \sim 2°$) and ($>8°$) along the longitudinal and latitudinal directions, respectively.

As is shown in figure 5.8, the line equivalent widths of the two iron Kα-lines seem to be roughly constant. We then fitted the line equivalent width in figure 5.8 with a constant model. The best-fit results were given in table 5.8. The constant model for the 6.7-keV line was fitted with the moderately small χ^2 values both along the longitudinal and latitudinal directions (table 5.3). Roughly speaking, the equivalent widths of the 6.7-keV lines are nearly constant around 500 eV from field to field. On the contrary to the 6.7-keV line, the equivalent width of the 6.4-keV line was fitted with the large χ^2 value of 131.2 (d.o.f. = 15) along the longitudinal direction. This large χ^2 value was mainly due to the prominently large equivalent width ($\approx$600 eV) observed in the GC2 field (l =0°.5).

As is shown in figure 5.9, the typical electron temperature and hydrogen column density derived from the 3.5–9 keV band continuum became about 20 keV and about 6×10^{22} H cm^{-2} in the GC-series fields, respectively. The typical electron temperatures in the GP- and GB-series fields are roughly 10 keV and 5 keV, respectively. The emission measure n_e^2V at the distance of 8.5 kpc was plotted in figure 5.9. The distributions of the emission measure are similar to those of the iron 6.7-keV line. Because of the limited energy-range, the hydrogen column density at each field was not clear outside the GC-series fields (figure 5.9).

5.4.3 Kα-lines of Magnesium, Silicon, Sulphur, Argon and Calcium

We also found Kα-lines from highly ionized ions of magnesium, silicon, sulphur, argon and calcium as well as iron in the GIS spectra (figures 5.1–5.3). We determined the observed line energies, surface brightness and equivalent widths of these lines by fitting a model of five Gaussian lines and an absorbed thermal bremsstrahlung to the data in 1.15–4.5 keV band. Due to the limited energy resolution, all the line widths were fixed to zero. We separately summarized the best-fit parameters in tables C.4–C.6. As was found in chapter 4, the diffuse X-rays show the Kα-lines not only from helium-like ions but also from hydrogen-like ions (figure 4.3). However, for each element, the fluxes of the Kα-lines from helium-like ions are about four-times brighter than those from hydrogen-like ions (table 4.1). We thus ignore the Kα-lines from hydrogen-like ions.

The highly ionized ions of iron emit L-complex emission lines around 1 keV

as well as K-lines around 7 keV. Because of the small interstellar absorption, the counts of the iron L-complex were dominant in the field away from the Galactic plane, i.e., most of the GB-series fields. The energy resolution of GIS is not good enough to distinguish between magnesium Kα-line and iron L-complex. In these fields, the best fit parameters of magnesium Kα-line sometimes floundered to unphysical values because of nearby iron L-lines. In fields with a heavy interstellar absorption, i.e., near the Galactic Center, the parameters for magnesium Kα-line coupled with that of the hydrogen column. In these fields, the best fit parameters for the magnesium Kα-line sometimes floundered to unphysical values, too. The stray lights from the bright source typically $\sim$1.5 degree away from the center of the GIS field of view make the broad-line-like feature around 1.5 keV (see figure 4.16 in [39]), which is due to the jump of the optical constant around M-edges of gold which coats the XRT surface. This broad-line-like feature was remarkably seen in the field of GP+1,+2 by GX 3+1 and GP$-$8,$-$12 by GX 354$-$0. In these fields, the best-fit parameters for the magnesium, silicon and sulphur lines floundered to unphysical values, too. The argon and calcium Kα-lines sometimes had too poor statistics to determine their line energies. For these data, we fixed the line energies for argon and calcium Kα-lines to the theoretical values predicted for the helium-like ions, i.e., 3.14 keV and 3.90 keV for argon and calcium, respectively.

After removing the fields where the parameters floundered to unphysical values, we plotted the line energies, surface brightness and equivalent widths for silicon, sulphur, argon, and calcium Kα-lines as a function of an angle from (l, b)=(0,0) along the longitudinal and latitudinal directions, respectively (figures 5.10–5.12). The line energies for each Kα-line are roughly constant from field to field and roughly coincide with the energies of Kα-lines from helium-like ions of each element. Diffuse thermal emission with distinct Kα lines from highly ionized ions of various elements confirms the presence of high-temperature plasmas around the Galactic Center ([51];[108];[109];[43]). The significant silicon Kα-line is detected in every observed field, while the sulphur, argon, calcium Kα-lines are not detected in all the fields.

Surface Brightness and Equivalent Width along the Longitudinal Direction

The longitudinal distributions of the surface brightness of all the four Kα-lines in figure 5.11 are similar to that of the iron 6.7-keV line (figure 5.7). All the four lines concentrate in the region within about 1 degree from the Galactic center, a factor of about 10 brighter than the surrounding region. We fitted the line equivalent width in figure 5.12 with a constant model. The best-fit results are given in table 5.4. Since all the four lines were fitted with moderately small χ^2 values, the equivalent widths of all the four Kα-lines are concluded to be roughly constant distributions (table 5.4).

Surface Brightness and Equivalent Width along the Latitudinal Direction

The latitudinal distributions of the surface brightness of argon and calcium Kα-lines are similar to that of the iron 6.7-keV line (figure 5.7). On the other hand, the surface brightness of the silicon Kα-line shows the distribution with double peaks near $b = 0^\circ$ and -1° , which is similar to that of the count rate in the 0.7–3 keV band (figure 5.4). The sulphur Kα-line shows the intermediate distribution among these Kα-lines.

We fitted the line equivalent width in figure 5.12 with a constant model. The best-fit results are given in table 5.4. The χ^2 value for the sulphur Kα-line became the largest value of 79.74 at d.o.f.=9 (table 5.4). We then confirmed the decreasing of the equivalent width of the sulphur Kα-line. The argon Kα-line also seems to be decreasing from the Galactic center as seen in the sulphur Kα-line, but with less confidence. The equivalent-width distribution of the calcium Kα-line is unclear because of the limited statistics. Only the equivalent width of the silicon Kα-line shows roughly constant distribution.

Table 5.1: Summary of the discrete sources ($> 4.5\sigma$)

No.	$l_{\rm II}$(degree)	$b_{\rm II}$(degree)	Catalog	ID	Soft/Hard
———(>10 counts s^{-1} GIS^{-1})———-					
#1[a]	(5.08)	(-1.02)	GX 5−1(Stray)	LMXB	(Both)
#2[a]	(2.29)	(0.79)	GX 3+1(Stray)	LMXB	(Both)
#3	-5.70	-0.14	GX 354−0	LMXB	Both
#4[a]	(0.68)	(1.16)	GRS 1739−278(Stray)	LMXB(transient)	(Both)
———(>1 counts s^{-1} GIS^{-1})———-					
#5	0.43	-0.39	A 1742−294	LMXB	Both
#6	-0.88	-0.10	1E 1740.7−2942	LMXB(BHC)	Both
#7	0.04	0.31	GRO J1744−28	LMXB(transient)	Both
———(>0.1 counts s^{-1} GIS^{-1})———-					
#8	-0.07	0.05	SgrA complex	Diffuse + LMXB	Both
#9	0.27	-0.03	1E 1743.1−2843	Unidentified(LMXB?)	Both
#10	-0.05	0.12	GRS 1741.9−2853	Unidentified(LMXB?)	Both
#11	-0.02	1.25	SLX 1737−282	Unidentified(LMXB?)	Both
#12	-0.33	-7.23	V4046 Sgr	T-Tauri star	Soft
#13	-0.24	-3.10	IRAS 17543−3044	Unidentified(AGN?)	Both
———(>0.01 counts s^{-1} GIS^{-1})———-					
#14	0.13	-0.12	(Radio Arc)	Diffuse Emission	Both
#15	-0.06	0.41	1WGA J1743.8-2846	Unidentified	Soft
#16	-3.82	0.11	IRAS 17325−3203	Unidentified	Soft
#17	-4.33	0.06	NGC 6383	HII region	Soft
#18	-7.25	-0.12	G352.7−0.1	SNR	Soft
#19	-7.83	-0.26	1RXS J172641.7−354030	Unidentified	Soft
———(<0.01 counts s^{-1} GIS^{-1})———-					
#20	-0.11	-9.09	AX J1822.5−3327[c]	Unidentified(AGN?)	Both
#21	-0.13	-8.94	AX J1821.9−2349[c]	Unidentified(CG?)	Both

a: These sources are located outside of the GIS field of view. We show their source positions cited from the *ROSAT* catalog.

b: "Soft" and "Hard" mean the significant detection in the 0.7–3 and 3–10 keV bands, respectively. "Both" means the detection both in the 0.7–3 and 3–10 keV bands.

c: Since there are no cataloged sources, we named these sources base on their GIS positions.

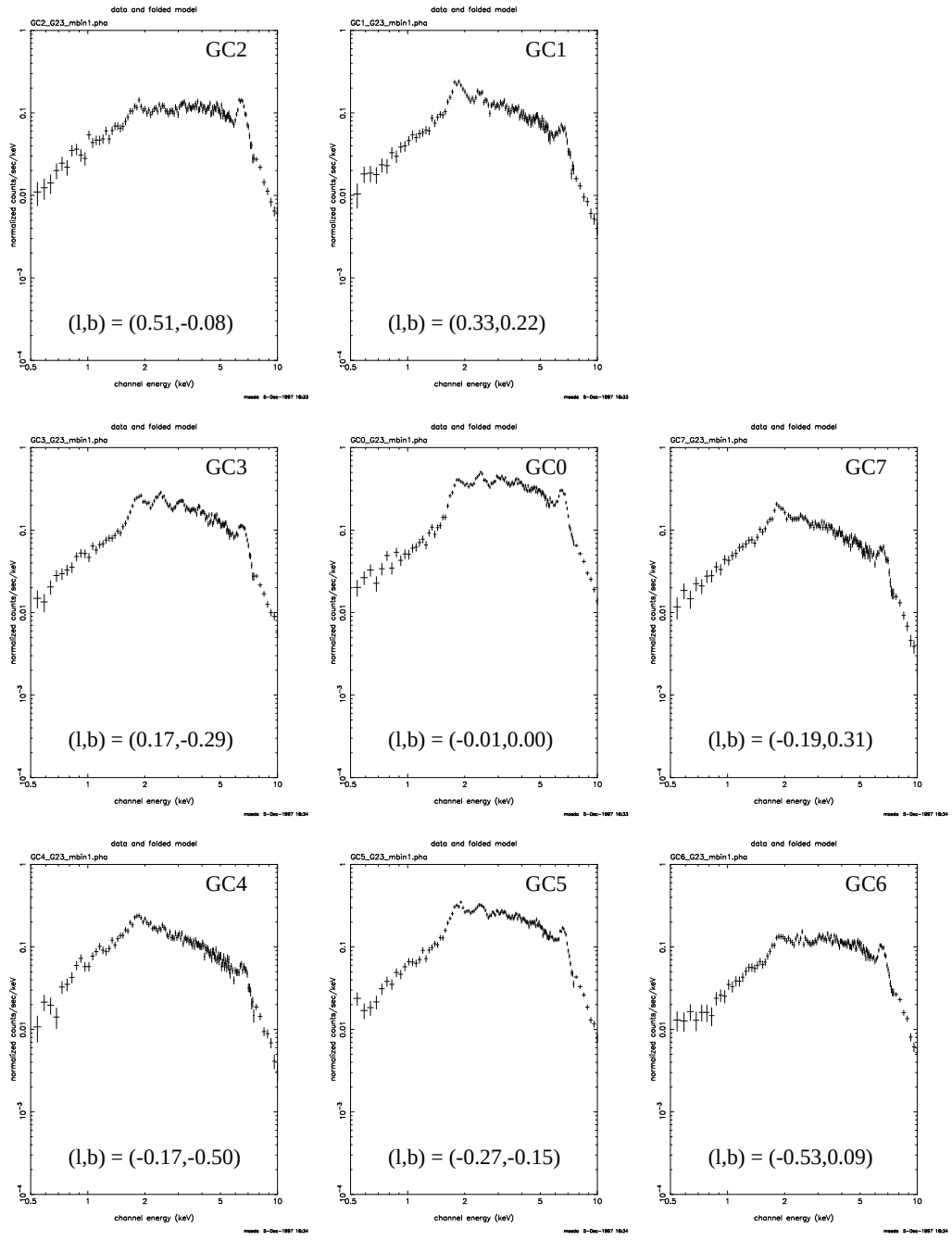

Figure 5.1: GIS spectra obtained through the GC-series observations. All the spectra were taken from the circular regions of 13′ radii. Each spectrum is the average of the two detectors (GIS2/3). The non-X-ray background (NXB) was subtracted while the cosmic X-ray background (CXB) is included (the details for NXB and CXB are described in appendix B). Error bars are 1 σ.

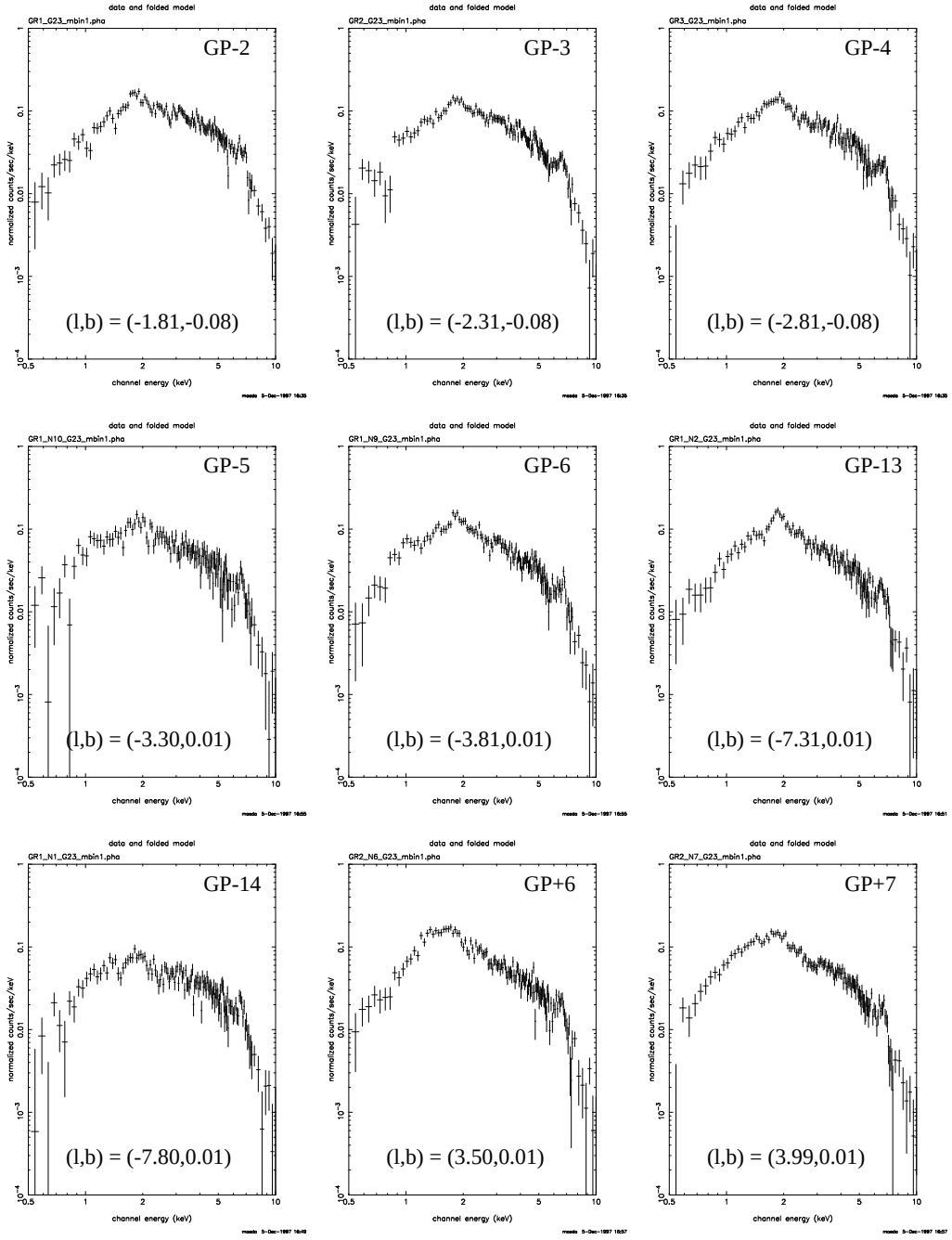

Figure 5.2: Same as figure 5.1, but through the GP-series observations. All the spectra were taken from the circular regions of $17'.5$ radii.

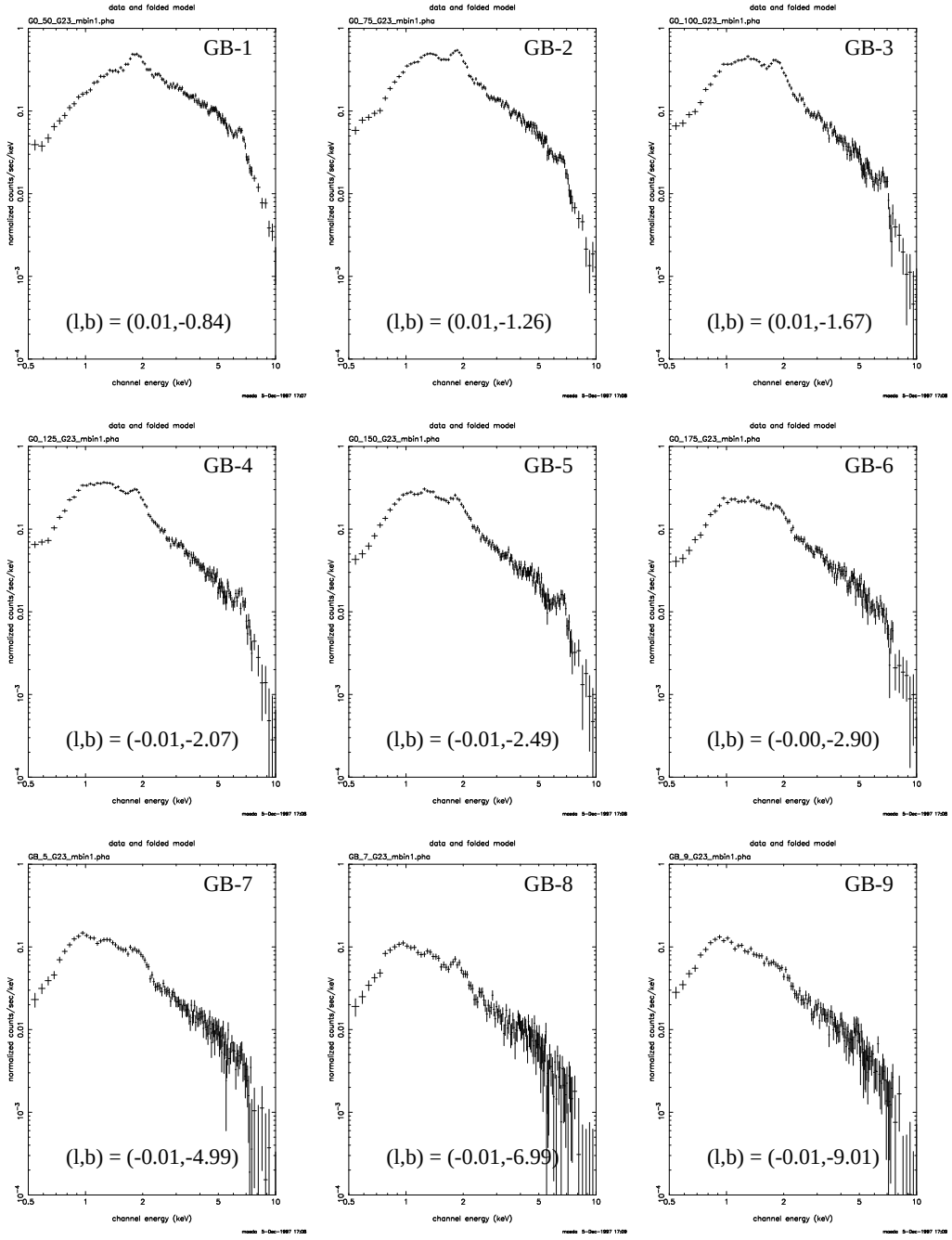

Figure 5.3: Same as figure 5.1, but through the GB-series observations. All the spectra were taken from the circular regions of $17'.5$ radii.

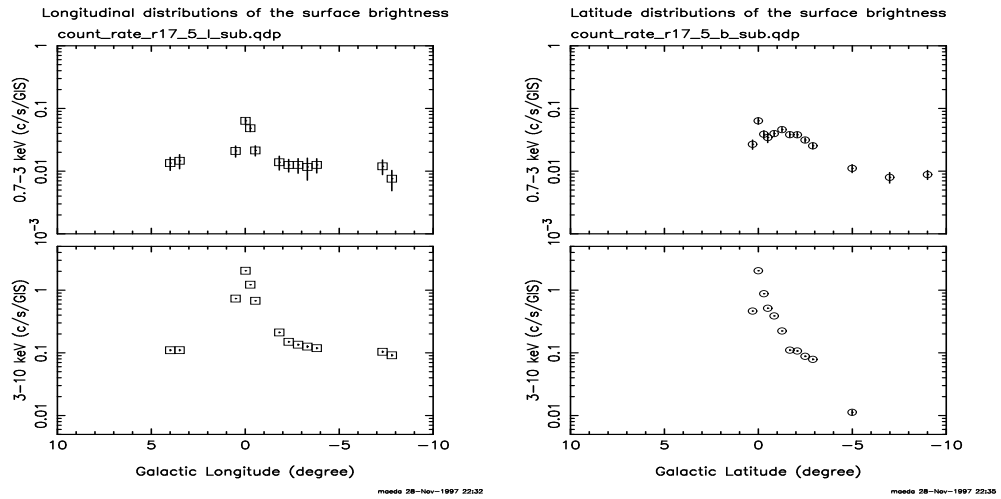

Figure 5.4: Distributions of the GIS count rates. All the count rates are the average of the two detectors (GIS2/3). Left and right panels show the longitudinal and latitudinal distributions, respectively. The distributions in the 0.7–3 and 3–10 keV bands are shown in upper and lower panels, respectively. We plotted the data with the field center of $|b| < 0^{\circ}.2$ for the longitudinal distributions and $|l| < 0^{\circ}.2$ for the latitudinal distributions, respectively. All the count rates are normalized with the circular regions of $17'.5$ radii. Both NXB and CXB were subtracted. Error bars are 1 σ.

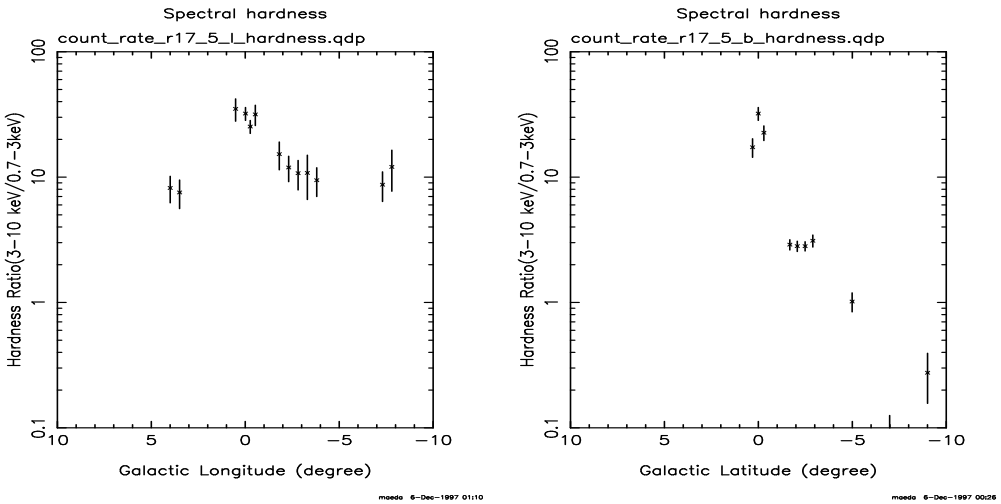

Figure 5.5: Distributions of the GIS spectral hardness ($\frac{3-10\mathrm{keV}}{0.7-10\mathrm{keV}}$). The hardness ratios were calculated with the count rates in figure 5.4. Left and right panels show the longitudinal and latitudinal distributions, respectively. Error bars are 1 σ.

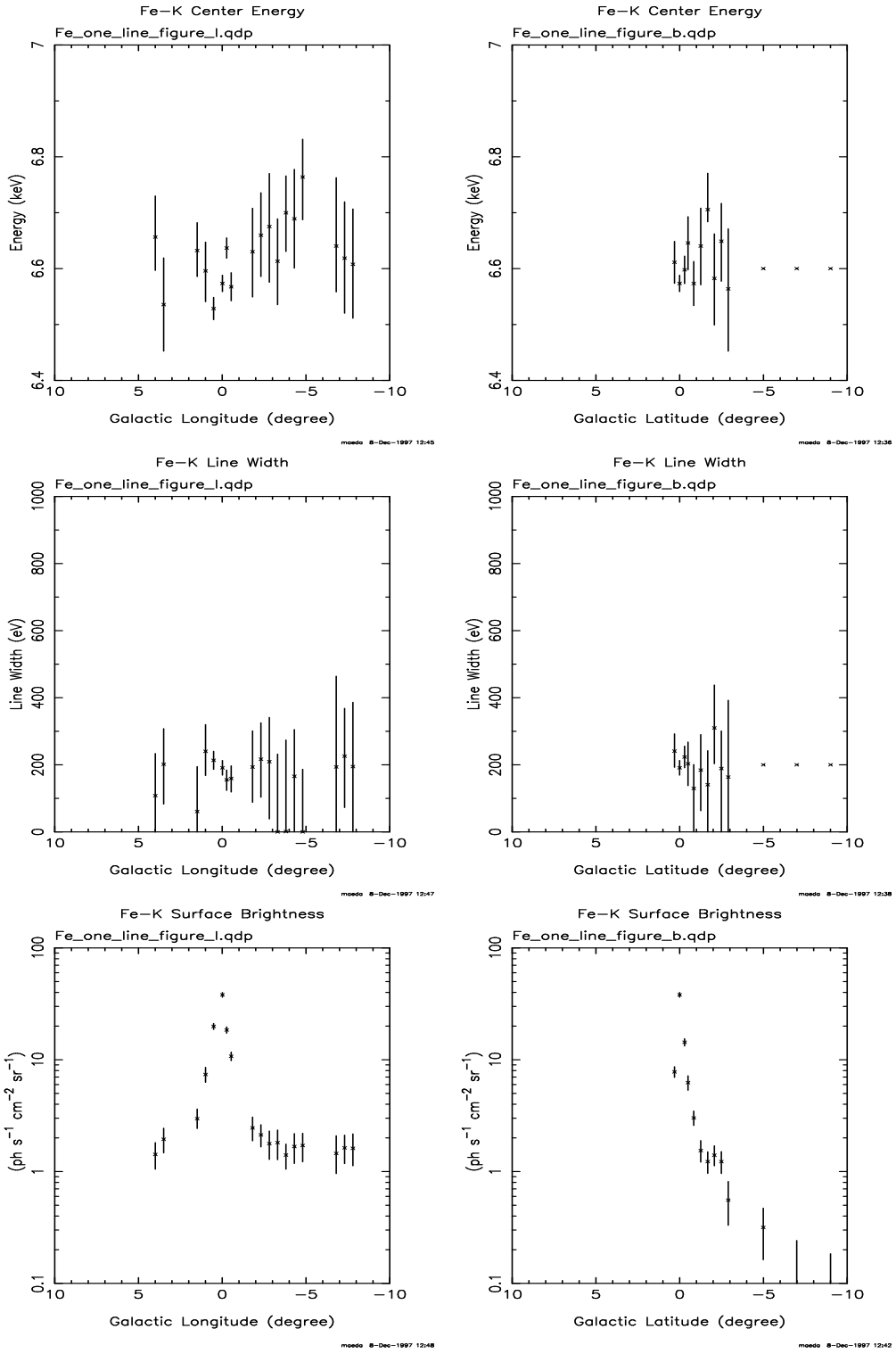

Figure 5.6: Plot of longitudinal (left) and latitudinal (right panel) distributions of the iron Kα-line determined with the iron-broad-line model (see section 5.4.1). The line energy, width and surface brightness are shown in upper, middle and bottom panels, respectively. We used the data with the field center of $|b| < 0^\circ.2$ for the longitudinal distributions and $|l| < 0^\circ.2$ for the latitudinal distributions, respectively. Error bars are 90% confidence level.

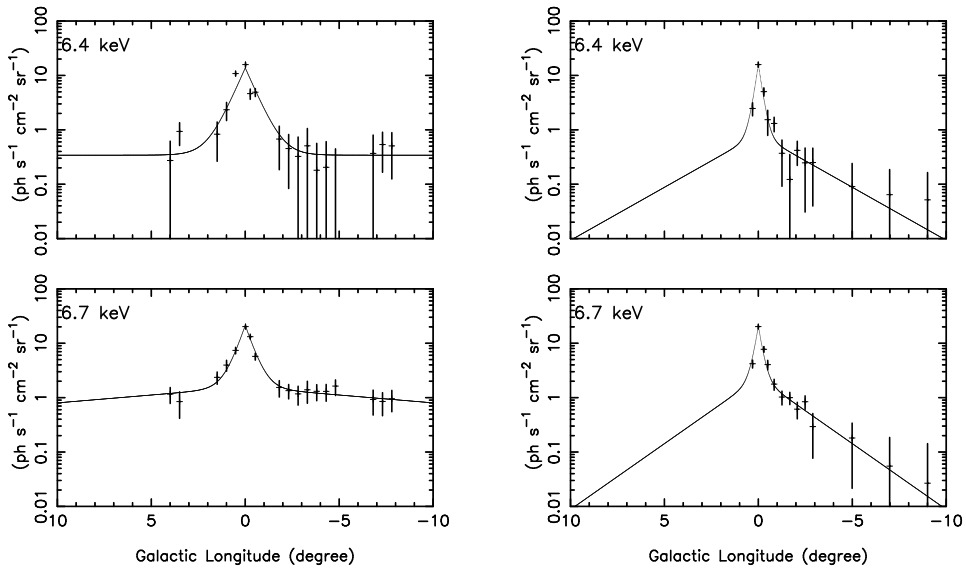

Figure 5.7: Plot of surface brightness distributions of the 6.4 (upper panel) and 6.7 keV (bottom panel) lines determined with the double iron-line model (see section 5.4.2). The distributions along the longitudinal and latitudinal directions are shown in right and left panels, respectively. The solid lines correspond to the best-fit values of the double exponential-decay model as summarized in table 5.2. We used the data with the field center of $|b| < 0^{\circ}.2$ for the longitudinal distributions and $|l| < 0^{\circ}.2$ for the latitudinal distributions, respectively. Error bars are 90% confidence level.

Table 5.2: GIS results of the double exponential-decay model to the surface brightness

	$S(\mathrm{l})^a$	$S(\mathrm{b})^a$
—- 6.4-keV line component ——		
ω_1 (degree)	0.54±0.07	$0.18^{+0.03}_{-0.05}$
S_1 (photons s^{-1} cm^{-2} sr^{-1})	13.4±1.4	$15.2^{+1.7}_{-2.3}$
ω_2 (degree)	∞(fix)^b	$2.2^{+3.2}_{-1.4}$
S_2 (photons s^{-1} cm^{-2} sr^{-1})	0.34±0.25	$0.83^{+2.09}_{-0.44}$
χ^2/d.o.f.	122.5/15	22.69/9
—- 6.7-keV line component ——		
ω_1 (degree)	0.42±0.06	0.19±0.03
S_1 (photons s^{-1} cm^{-2} sr^{-1})	19.7±1.6	18.1±1.8
ω_2 (degree)	15(>8)	$1.8^{+0.8}_{-0.5}$
S_2 (photons s^{-1} cm^{-2} sr^{-1})	1.6±0.5	$2.3^{+1.1}_{-0.7}$
χ^2/d.o.f.	17.67/14	30.59/9

Errors are 90% confidence level.

a : $S(\theta)$ is the surface brightness as a function of an angle θ from (l, b)=(0,0) given by $S(\theta) = S_1 \exp(-\frac{|\theta|}{\omega_1}) + S_2 \exp(-\frac{|\theta|}{\omega_2})$.

b : The fitting was insensitive to this parameter. We fixed to this parameter to ∞.

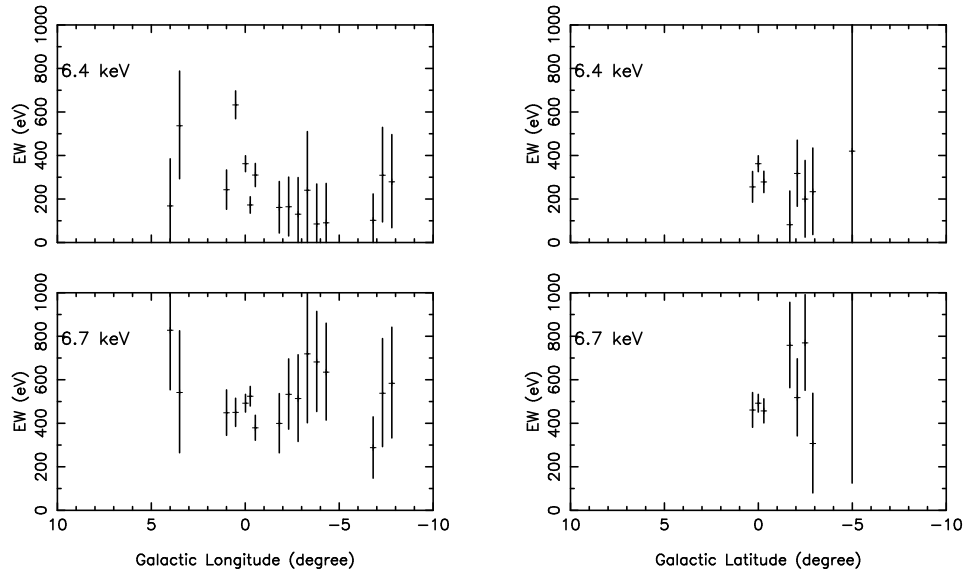

Figure 5.8: Same as figure 5.7, but for the line equivalent width.

Table 5.3: Best-fit results of the constant model to the equivalent widths of iron Kα-lines

Line name	Equivalent width(eV)	χ^2/d.o.f.
—- Along the longitudinal direction ($\|b\| < 0^\circ.2$) ——		
Fe 6.4-keV	294±21	131.2/15
Fe 6.7-keV	477±23	26.32/15
—- Along the latitudinal direction ($\|l\| < 0^\circ.2$) ——		
Fe 6.4-keV	310±27	14.72/7
Fe 6.7-keV	487±30	12.80/7

We performed the fittings to the data points given in the left and right panels in figure 5.8 along the longitudinal and latitudinal directions, respectively. Errors are 90% confidence level.

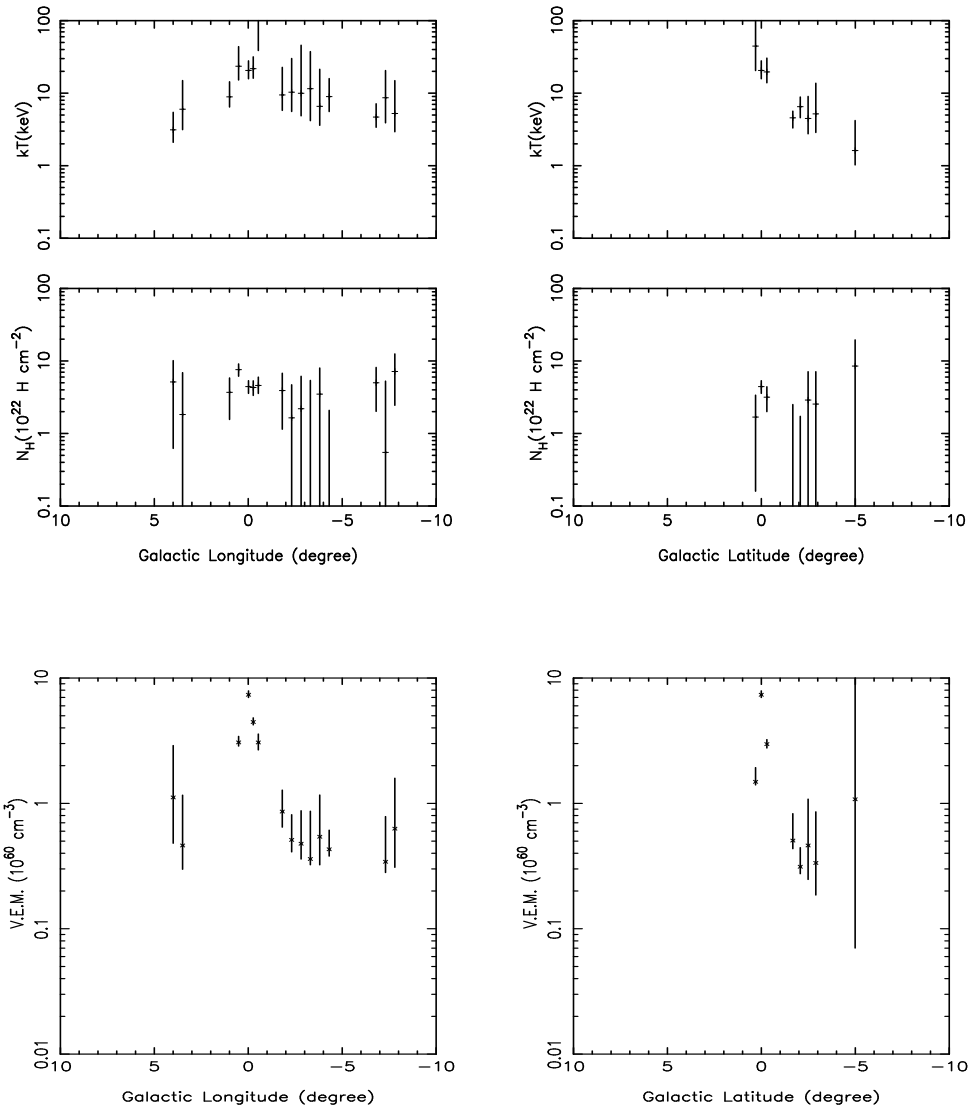

Figure 5.9: Same as figure 5.7, but for the electron temperature (upper panel), absorption column (meddle panel) and emission measure (bottom panel). The emission measure in unit of 10^{60} cm^{-3} is normalized by a 1°.5 radius circular field. The emission measure was calculated assuming the distance of 8.5 kpc.

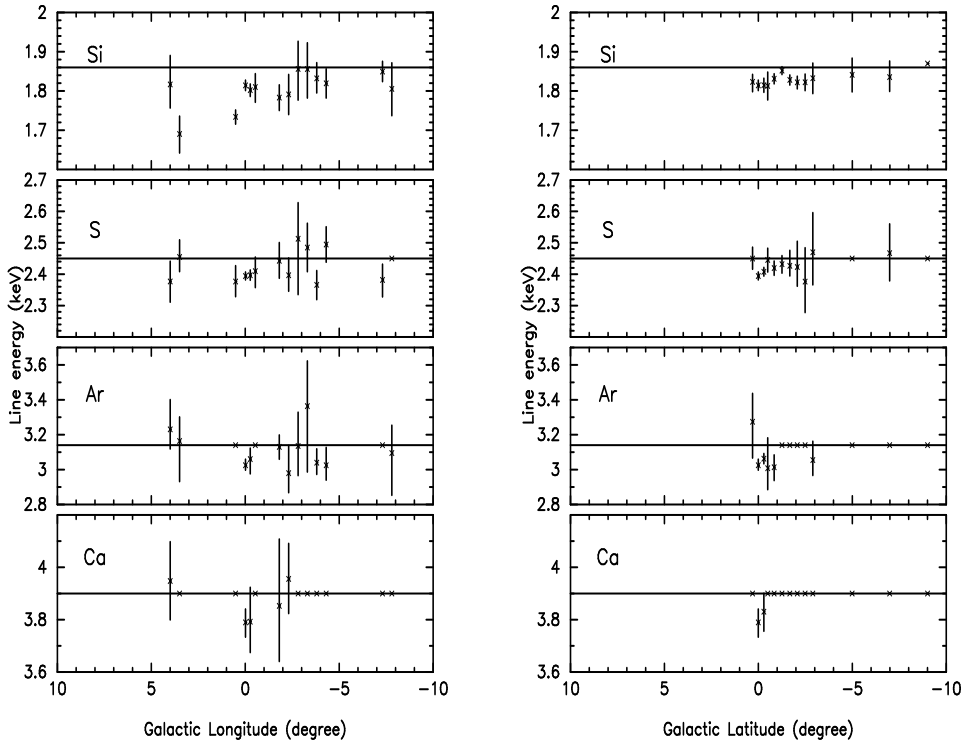

Figure 5.10: Plot of line energy distributions of silicon (top panels), sulphur (second), argon (third) and calcium (bottom) Kα-lines. The distributions along the longitudinal and latitudinal directions are shown in right and left panels, respectively. We draw solid lines, which mean the theoretically predicted line energies for Kα-lines from helium-like ions of silicon (upper panel), sulphur (second), argon (third) and calcium (bottom), respectively. We used the data listed in table C.4 with the field center of $|b| < 0^\circ.2$ for the longitudinal distributions and $|l| < 0^\circ.2$ for the latitudinal distributions, respectively. We did not plot the data obtained in the field where the best-fit parameters floundered to unphysical values (see text). Error bars are 90% confidence level.

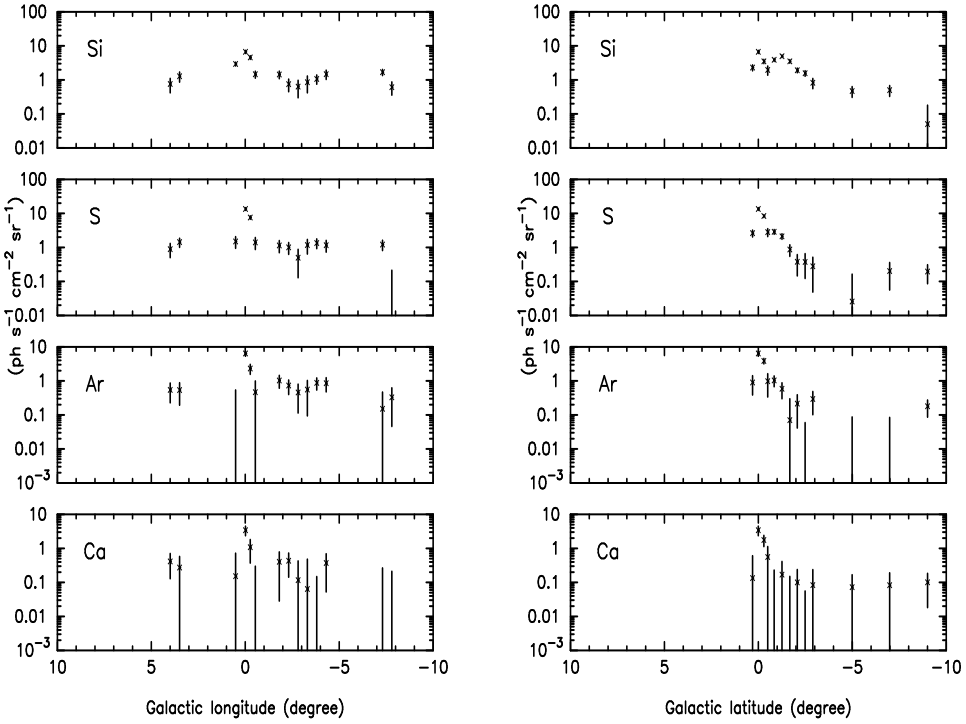

Figure 5.11: Same as figure 5.10, but for the surface brightness.

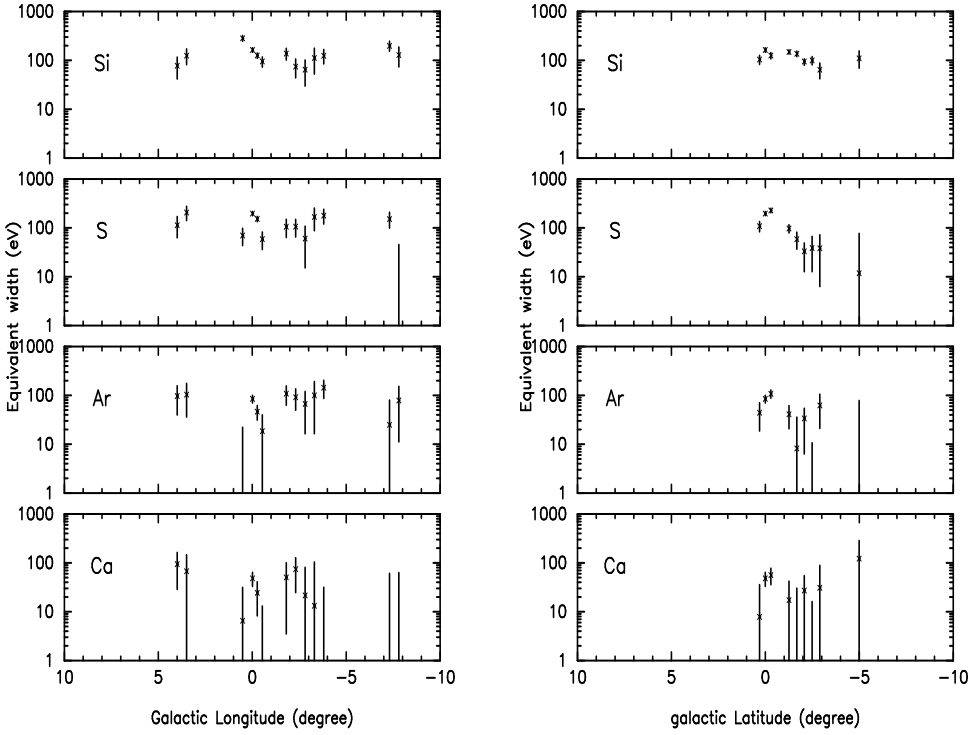

Figure 5.12: Same as figure 5.12, but for the equivalent width. All the data were obtained in the less-contaminated field where the contaminated X-rays both in the 0.7–3 and 3–10 keV bands by the discrete sources occupied less than ∼10% of those from the diffuse emission itself.

Table 5.4: Best-fit results of the constant model to the equivalent widths of silicon, sulphur, argon and calcium Kα-lines

Line name	Equivalent width(eV)	χ^2/d.o.f.
—- Along the longitudinal direction ($\|b\| < 0^\circ.2$) ——		
Si He-like	82±8	33.32/12
S He-like	80±9	41.97/12
Ar He-like	34±8	19.20/12
Ca He-like	13±8	9.603/12
—- Along the latitudinal direction ($\|l\| < 0^\circ.2$) ——		
Si He-like	77±6	21.58/8
S He-like	67±8	79.74/8
Ar He-like	24±7	35.70/8
Ca He-like	16±8	8.351/8

We performed the fittings to the data points given in the left and right panels in figure 5.12 along the longitudinal and latitudinal directions, respectively. Errors are 90% confidence level.

5.5 Correlations of Flux-Ratios

We consider a differential volume dV whose direction is within a solid angle $d\Omega$ at a distance of r from the Sun (figure 5.13). The luminosity $L(E, \theta, r)$ from the infinitesimal volume, as a function of an energy E, an angle θ from the Galactic center and a distance r, is given by,

$$dL(E, \theta, r) = \varepsilon(E, \theta, r)dV = \varepsilon(E, \theta, r) \cdot r^2 dr d\Omega \tag{5.2}$$

with a volume emissivity ε. If we assume a single absorption at each angle, a observed flux $F(E, \theta)$ is given by

$$F(E, \theta) = \alpha(E, \theta) \int \frac{dL(E, \theta, r)}{4\pi r^2} d\Omega = \alpha(E, \theta) \int \varepsilon(E, \theta, r) dr \frac{d\Omega}{4\pi}, \tag{5.3}$$

$$\alpha(E, \theta) = e^{-N_{\rm H}(\theta)\sigma(E)}. \tag{5.4}$$

where $N_{\rm H}$ is an hydrogen column density (in unit of $\rm cm^{-2}$) and σ is a photo-electric cross-section ($\rm cm^2$). Then the flux-ratio of energies E_0 and E_1 at an angle θ is written as

$$\frac{F(E_1, \theta)}{F(E_0, \theta)} = \frac{\alpha(E_1, \theta)}{\alpha(E_0, \theta)} \frac{\int \varepsilon(E_1, \theta, r) dr \frac{d\Omega}{4\pi}}{\int \varepsilon(E_0, \theta, r) dr \frac{d\Omega}{4\pi}}. \tag{5.5}$$

We assumed a volume-emissivity ratio at energies E_0 and E_1 to be independent of a distance r,

$$R(E_0, E_1, \theta) \equiv \frac{\varepsilon(E_1, \theta, r)}{\varepsilon(E_0, \theta, r)} = \frac{L(E_1, \theta, r)}{L(E_0, \theta, r)}. \tag{5.6}$$

For example, a thin thermal plasma with single temperature, single abundance and single ionization-time-scale is described by equation 5.6. From the equations 5.5 and 5.6, we can get a simple relation given by

$$\frac{F(E_1, \theta)}{F(E_0, \theta)} = \frac{\alpha(E_1, \theta)}{\alpha(E_0, \theta)} R(E_0, E_1) = e^{-N_{\rm H}(\theta)(\sigma(E_1) - \sigma(E_0))} R(E_0, E_1). \tag{5.7}$$

As well as equation 5.7, we can also get one more similar relation given by

$$\frac{F(E_2, \theta)}{F(E_0, \theta)} = \frac{\alpha(E_2, \theta)}{\alpha(E_0, \theta)} R(E_0, E_2) = e^{-N_{\rm H}(\theta)(\sigma(E_2) - \sigma(E_0))} R(E_0, E_2). \tag{5.8}$$

From equations 5.4, 5.7 and 5.8, we can derive a relation, which is independent of an absorption column $N_{\rm H}$, given by

$$\log \frac{F(E_1, \theta)}{F(E_0, \theta)} - a \log \frac{F(E_2, \theta)}{F(E_0, \theta)} = \log R(E_0, E_1, \theta) - a \log R(E_0, E_2, \theta), \tag{5.9}$$

or

$$\frac{F(E_1,\theta)}{F(E_0,\theta)} = \frac{R(E_0,E_1,\theta)}{R(E_0,E_2,\theta)^a}(\frac{F(E_2,\theta)}{F(E_0,\theta)})^a \equiv C(E_0,E_1,E_2,\theta)(\frac{F(E_2,\theta)}{F(E_0,\theta)})^a, \quad (5.10)$$

where

$$a \equiv \frac{\sigma(E_1)-\sigma(E_0)}{\sigma(E_2)-\sigma(E_0)}. \quad (5.11)$$

We detected the intense three Kα-lines from helium-like ions of silicon, sulphur and iron. Therefore, we can apply line energies and surface brightness(fluxes) of these lines to equation 5.9 or 5.10. We set E_0, E_1 and E_2 to 6.7 keV(Fe He-like), 1.86 keV(Si He-like) and 2.45 keV(S He-like), respectively. For this combination, we found a(defined by equation 5.11) to be 2.24 using the cosmic material([75]). For simplicity, we used the best-fit values of the exponential-decay model as the flux of the iron 6.7-keV line(table 5.2), while we used the data points plotted in figure 5.11 as the fluxes for Si He-like and S He-like Kα-lines.

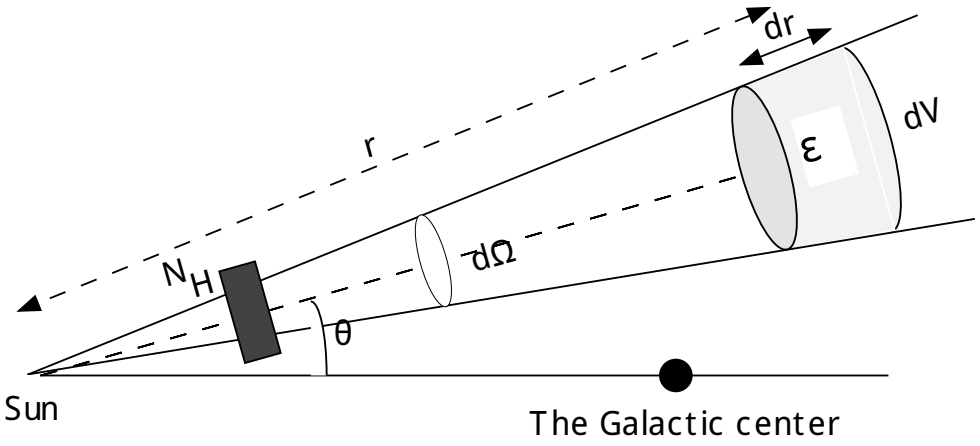

Figure 5.13: A schematical view to show a relation between the Sun and a differential volume of emitting region.

We show correlations between the flux-ratios using these three Kα-lines in figures 5.14 & 5.15. The GC-series fields share the lower left region in figures 5.14 & 5.15, while the GB-series fields share the upper right (figure 5.15). The GP-series fields share the intermediate region between the GC- and GB-series fields (figure 5.14). The Galactic Center exhibits the large interstellar absorption. The absorption decrease slowly along the Galactic plane and rapidly perpendicular to

the plane([91]). From $\sigma(1.86\mathrm{keV}) > \sigma(2.45\mathrm{keV}) > \sigma(6.7\mathrm{keV})$, we can interpret that these distribution seen in figures 5.14 & 5.15 is explained by the difference of the interstellar absorption using equations 5.7 and 5.8.

We show a solid line in figures 5.14 & 5.15, which is corresponding to the relation derived by substituting $a = 2.24$ and $C = 1$ for equation 5.10. The GC- and GP-series fields seem to be roughly located on this solid line in figures 5.14 & 5.15 except for the GC2 and GC6 fields. We interpreted from equation 5.10 that the emissivity-ratio of the silicon to the sulphur Kα-line normalized by that of the iron Kα-line is roughly constant along the Galactic plane. Complex distribution of many dense molecular clouds in the GC0, GC2 and GC6 fields was reported by the radio observations ([80]; [105]; figure E.1). The assumption of a single absorption column defined in equation 5.3 may be not appropriate for these fields. Therefore it is less certain whether the emissivity ratios in the GC2 and GC6 fields are different or not.

In figure 5.15, the GB-1 and GB-2 fields are roughly located on the same solid line, while the GB$-3\sim-7$ fields show the systematic shift to the left side of the solid line. Therefore we can interpret that the emissivity-ratio of the silicon to the sulphur Kα-line normalized by that of the iron Kα-line is high in the GB-series fields more than 2 degree away from the Galactic center. The GB-8 and GP-9 fields show the lower count rates (figure 5.4), which are same order of that from CXB. The fluxes in the two fields then depend on the reproducibility of the cosmic X-ray background(CXB, see appendix B for detail). Since we did not research it here, we do not constraint the emissivity ratios in the GB-8 and GB-9 fields.

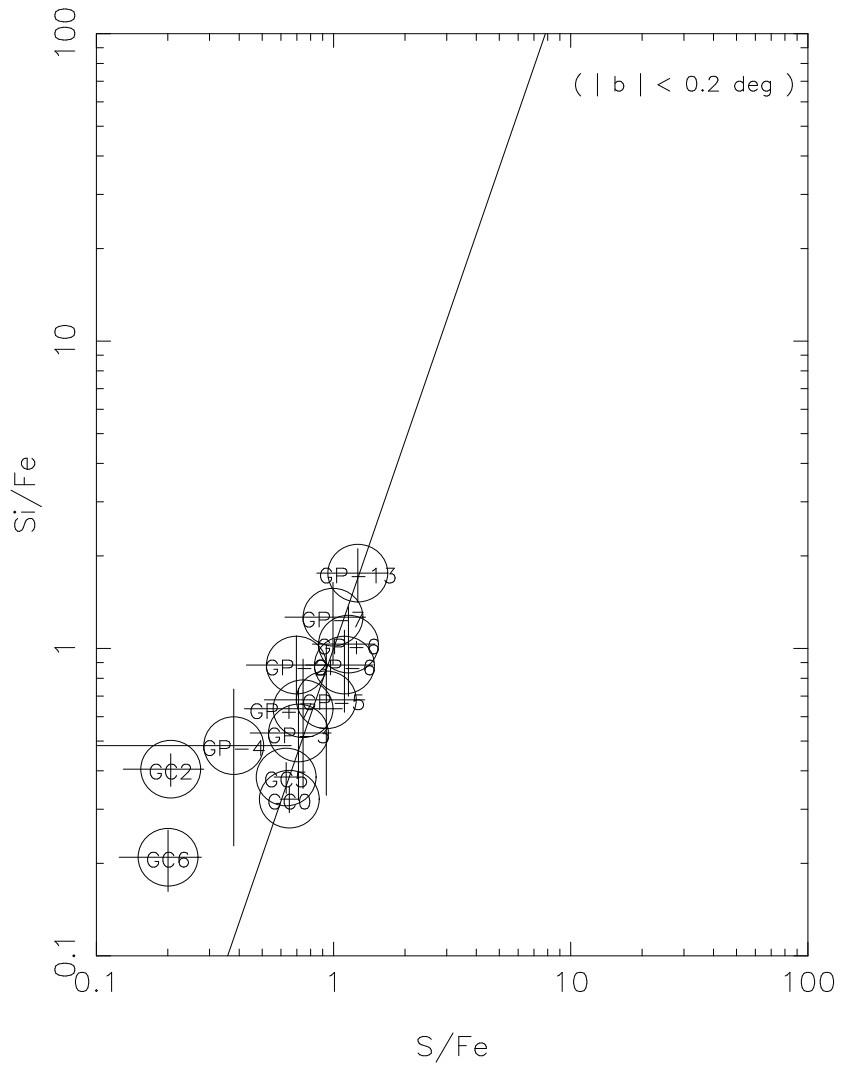

Figure 5.14: Correlation between the two flux-ratios using the three lines at each field. The horizontal(x) and vertical(y) axes correspond to the flux-ratios of S He-like to Fe 6.7-keV and Si He-like to Fe 6.7-keV, respectively. We simultaneously plotted a solid line given by a function of $y = x^{2.24}$. We used the data with the field center of $|b| < 0^\circ.2$. Correlation in the fields of $|l| < 0^\circ.2$ was separately plotted in figure 5.15. The field name is defined in chapter 3. Error bars are 90% confidence level.

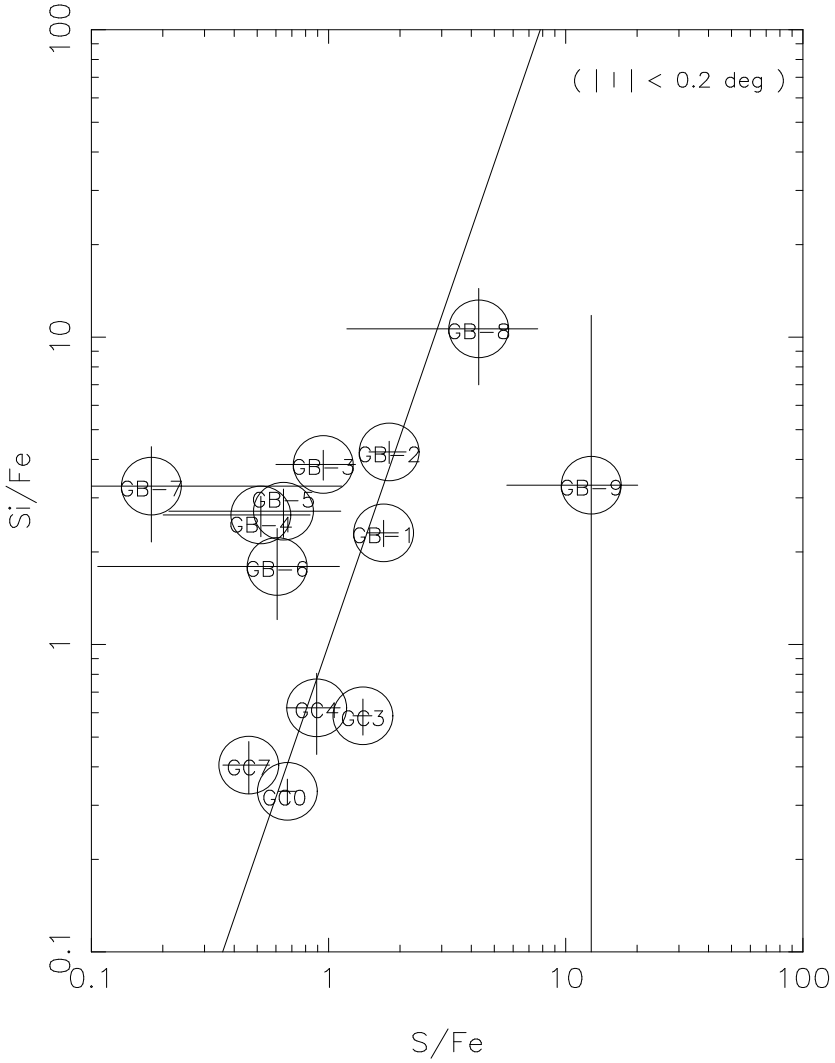

Figure 5.15: Same as figure 5.14, but for the data of $|l| < 0^{\circ}.2$.

Chapter 6

Monitoring Observations of the Galactic Center Sgr A

6.1 Introduction

The Galactic Center region is very complex over a wide range of wavelengths ([74] for a recent review). X-ray structures near to the Galactic center have been confusing due either to the limited spatial resolution of the non-imaging instruments or to the limited energy range of the soft X-ray telescopes or both. The *ASCA* satellite has the capability to observe the Galactic center with a reasonable high spatial resolution as well as sensitivity for the high-energy band up to 10 keV.

In chapter 4, we found two moderate bright spots near the Galactic center. The softer spot (hereafter "the soft source") appears diffuse structure. The bright and unresolved radio source Sgr A* has currently been believed to be the nuclear supermassive black hole candidate($\sim 3\times10^6$ $M_\odot$) of our Galaxy. The mean position of the soft source corresponds to Sgr A* within a $\sim 0'.4$-radius error circle. The other bright spot (hereafter "the hard source") is about $1'.3$ south-west from Sgr A*. The flux was found to be about five times brighter after one years later. We also found an X-ray burst and eclipses, establishing that this source is an eclipsing low-mass X-ray binary (Maeda et al. (1996 [62]); hereafter Paper II). Only one possible X-ray counterpart A 1742−289 was found near to the edge of the error circle, which was a old transient source flared up on 1975 February 16([21];[11]; [114]). However, since no eclipse was found in A 1742−289, the hard source is likely a new LMXB and is named as AX J1745.6−2901([47]).

In this chapter, we report the results of the monitoring observations of the Galactic center Sgr A including the results of Paper I([52]) and II([62]).

6.2 Data Screening and Correction

The time variability is key information for the activity of the soft source(which includes Sgr A*) and the hard source (AX J1745.6−2901) and is discussed in the following sections.

6.2.1 The GIS Data for the '93 Autumn & '94 Autumn Observations[1]

The non-X-ray background, which is due to the high-energy particle in orbit, depends on the cut-off-rigidity. The count rate of the non-X-ray background varies from 2×10^{-3} to 4×10^{-3} counts s^{-1} GIS^{-1} when the count rate is taken from a circular region of a radius of 4 arcmin. The Sgr A* complex and AX J1745.6−2901 in non-eclipse have count rates of about 0.1∼1 counts s^{-1} GIS^{-1}. Therefore the results do not depend much on the non-X-ray background. In order to obtain the data with the longer span time, we can re-screened with the looser criteria, which do not include the rejection during times of high particle background as a function of the cut-off-rigidity.

Since in the '93 & '94 observations the observed L1[2] count rate was several counts s^{-1} GIS^{-1}, the dead time is less than ∼1% for HIGH- and MEDIUM-bit-rate data[3]. There are no bit-rate-LOW data in the two observations. Therefore we did not need to apply the dead time correction for these data in order to obtain the accurate fluxes.

[1]These criteria were also applied for a timing analysis of the the short time-scale of ∼ 1 s for the '97 spring data given in section 6.4.1.

[2]L1 is one of the monitor count rate, which survives the hardwired background rejection. The L1 count rate is useful for the estimation of the dead time.

[3]During the '94 autumn observations, AX J1745.6−2901 exhibited a type-I burst in the HIGH-bit-rate. The maximum peak L1 count rate shows ∼ 40 counts s^{-1}, which is equivalent to dead time fraction of several %. Therefore we applied the dead time correction only for the burst analysis. The detailed burst analysis is given in section 6.4.3.

6.2.2 The SIS Data for the '93 Autumn & '94 Autumn Observations

If one needs to obtain the most accurate fluxes using the SIS data, telemetry-saturated frames should not be used since the count-rates will be incorrect. In order to search the flux variability, we applied the strict criteria with no telemetry saturation.

6.2.3 The GIS Data for the '97 Spring Observations

In the 1997 spring observations, the transient X-ray bursting pulsar GRO J1744−28 became more than ten times brighter than the two sources in the Sgr A region as is given in the later session. As is discussed in the later session, the contamination of GRO J1744−28 could significantly degrade the data quality of the two sources. Therefore we added the further criteria to them given in sections 6.2.1 & 6.2.2.

About 0.4 % of the total X-rays from GRO J1744−28 falls on a $4'$ radius circular region near Sgr A. The observed L1/GIS count rates of GRO J1744−28 were ∼300 counts s^{-1} GIS^{-1} at the burst peak and ∼30 counts s^{-1} GIS^{-1} in the persistence, respectively. Therefore the X-rays from GRO J1744−28 falling on a $4'$ radius circular region near the Sgr A region are estimated to be ∼1 counts s^{-1} at the burst peak and ∼0.1 counts s^{-1} at the persistent state, respectively. At the burst peak, the counts from GRO J1744−28 falling on this region were larger than that from the two sources, which significantly damaged the data quality in this region. Therefore, we selected only the data during the persistent state of GRO J1744−28 with the additional screening criteria given by,

$$\mathrm{L1} \ < 40 \text{ counts } s^{-1}, \tag{6.1}$$

where L1 is the monitor count rate which survives the hardwired background rejection.

Even in the persistent state, the count rate of GRO J1744−28 is so high that the GIS dead time is not ignored. Using the monitor data, the dead time was corrected by the formula

$$\text{GIS dead time fraction} = 1 - (1 - \mathrm{LD} * \tau) * \frac{\mathrm{CI}}{\mathrm{L1}} * \frac{\mathrm{TLM} - \mathrm{Out}}{\mathrm{CO}} \tag{6.2}$$

where τ is 25μsec and LD, L1, CI, CO and TLM-Out are the monitor count rates which hits the lower discriminator before any rejection, survives the hardwired background rejection, transfers into the CPU, accepts as X-ray events by the CPU, and outputs to the telemetry, respectively. The GIS dead time fractions during the '97 spring observations are about a few %, 30-50% and 70-90 %, in HIGH, MEDIUM and LOW-bit-rate, respectively.

6.2.4 The SIS Data for the '97 Spring Observations

As for the GIS data, we used only the data when GRO J1744−28 was in non-bursting phase, adding the screening criteria given by equation 6.1,

6.3 Images Near the Galactic Center

6.3.1 The GIS Images

Figure 6.1 shows the GIS images for the three observations in the 1–3 keV and 3–10 keV bands. We can see three bright spots in figure 6.1, which were listed in table 6.1. Since the spot #3 was seen only at the west tip of the '97 spring images, the spot #3 is a bright transient source. As the spot #3 exhibits type-II X-ray bursts and periodic pulsations of ∼0.467 second, this source is found to be a cataloged bursting pulsar GRO J1744−28 as well as the positional coincidence, which is a low-mass X-ray binary including a neutron star. During the '97 spring *ASCA* observations, GRO J1744−28 showed 17 type-II X-ray bursts and dips. The flux in the persistence was found to be $\sim 4\times10^{-9}$ erg s^{-1} cm^{-2}(2–10 keV band). GRO J1744−28 was then found to the brightest source in the GIS field of view during '97 spring, though GRO J1744−28 was not detected in '93 & '94 autumn. On the contrary, the other two spots(#1 & #2) were detected in all the three observations. The spot #1 is located near the Galactic center Sgr A. The other north-east spot #2 is found to be point-like, which was already catalogued and was named as 1E 1743.1−2843. 1E 1743.1−2843 showed a flux of 1×10^{-10} erg s^{-1} cm^{-2}(2–10 keV band), which was comparable to that of the Sgr A complex. 1E 1743.1−2843 has no counterpart of other wavelengths and has not been identified yet. The spot #1 is composed of the diffuse emission and a bright point source AX J1745.6−2901 as is found in the later section 6.3.2. Then we tentatively referred

to the spot #1 as the "Sgr A complex". In this chapter, we would concentrate to research the Sgr A complex. Detail results of GRO J1744−28 and 1E 1743.1−2843 were separately reported by [78] and [91].

Table 6.1: Summary of bright sources found in the GIS images

Source No.	Source position ($l_{\rm II}$, $b_{\rm II}$)	Source name	Identification
#1	(−0.07,0.05)	Sgr A complex	Diffuse & LMXB^a(AX J1745.6−2901)
#2	(0.27,−0.03)	1E 1743.1−2843	Unidentified(LMXB?)
#3	(0.04,0.31)	GRO J1744−28	LMXB^a

a : LMXB is an abbreviation for Low Mass X-ray Binary which contains a neutron star and an old low-mass star(typically $M_* \leq 2{\rm M}_\odot$)

6.3.2 The SIS Images

Figures 6.2a&b show the SIS images for the '93 autumn observation in the 1–3 keV (the soft) and 3–10 keV (the hard) bands, respectively. The Chris-cross structure is the gap of each CCD chip (one CCD camera consists of 4 adjacent CCD chips). The Sgr A complex is located at the bright region around ($l_{\rm II}$, $b_{\rm II}$) = (−0.07,0.05). Figures 6.2c&d are the same as figures 6.2a&b, but for the '94 autumn observation, pointing slightly shifted from the '93 autumn position. Thus, the Sgr A complex in figure 6.2c&d is moved to the south-west chip. From figures 6.2b&d, we found a bright spot in the hard-band images (here the "hard source"). Another bright spot was found about $1'.5$ north-east from the hard source. In the soft-band images, this spot is brighter than the hard source, and appears to be diffuse structure. An oval-shaped region of $2'\times3'$ centered at this peak is distinctly bright by a factor of about five compared to the surrounding region as described in chapter 4. We refer to the peak as the "soft source". In order to determine the source positions, we compared the SIS image (1–2.5 keV band) of adjacent pointing data during '93 autumn with the *ROSAT* image given by [85]. We then found two point-sources in the *ASCA* SIS images near to the position of the *ROSAT* catalog: 1E 1743.4−2852 and RX J1746.1−2859. The differences between the *ASCA* and *ROSAT* positions

were $\sim 0'.4$ and $\sim 0'.1$ for 1E 1743.4−2852 and RX J1746.1−2859, respectively. We therefore estimate that the error of the *ASCA* position (including systematic error of the attitude determination of *ASCA*) for the Galactic center observations was less than $\sim 0'.4$. We listed the position of the soft and hard sources determined from the three observations in table 6.2. From table 6.2, we found that the positional differences between the two early independent observations are $0'.3$ and $0'.1$ for the soft and hard sources; both are within a possible error of $0'.4$. The mean position of the soft source during the two early independent observations is within $0'.2$ from the Galactic center, Sgr A* at $(\alpha_{\rm J2000}, \delta_{\rm J2000})$ = (266.4165,−29.0078). Thus, the soft source is likely to be the X-ray counterpart of Sgr A*. The mean position of the hard source was determined to be $(\alpha_{\rm J2000}, \delta_{\rm J2000}) = (266.401, -29.026)$, which is about $1'.3$ away from the Galactic center Sgr A*.

As GRO J1744−28 has relatively small column density of about 6×10^{22} H cm^{-2}, the position of this source was well studied by the soft X-ray telescope HRI/*ROSAT*([4]). They found that the position of GRO J1744−28 was $(\alpha_{\rm J2000}, \delta_{\rm J2000})$ =(266.1379, -28.7414) with the circular error of $\sim 10''$ radius. During the '97 spring observation, we found that GRO J1744−28 detected at the edge of the CCD chip and found that the difference of SIS/*ASCA* and HRI/*ROSAT* positions of GRO J1744−28 was less than $0'.2$. Therefore the positional deference between SIS/*ASCA* and HRI/*ROSAT* is estimated to be about $\sim 0'.3$ after including the *ROSAT* systematic error. The differences between the mean position of the early two observations and the position of the '97 spring were $\sim 0'.4$ and $\sim 0'.3$ for the soft source and the hard source, respectively. We then confirmed that the positions of the '97 observations for the two sources coincided with the early two observations within the systematic error.

We searched for a cataloged X-ray source within an error region of $0'.4$ of the hard source, and found a transient source (A 1742−289) near to the edge of the error circle. A 1742−289 was found to flare up on 1975 February 16, and was repeatedly observed with the *Ariel* 5, *ANS*, and *Copernicus* satellites ([11]; [21]). The position of A 1742−289 determined with the RMC onboard *Ariel* 5 is $(\alpha_{\rm J2000}, \delta_{\rm J2000})$ = (266.404±0.02, −29.018±0.02). The radio source, which was unseen in 1974, appeared near to the center of the error box of A 1742−289 at the position of $(\alpha_{\rm J2000}, \delta_{\rm J2000}) = (266.4048, -29.0180)$, with about $3''$ error ([16]). A 1742−289 was reported to exhibit a large column density of approximately 2×10^{23}

H cm^{-2}. As shown in section 6.4.2, the hard source was found to exhibit $\sim 10^{23}$ H cm^{-2} of absorption, which is a similar value to A 1742−289 during the flare state. However Kennea & Skinner (1996 [47]) re-analyzed the *Ariel* 5 RMC data and found no evidence for eclipses as described in the later section, which suggests that the hard source is a previously undetected distinct system. Although the column density and the positional coincidence are very similar, we concluded that the hard source is a new source, which was named as AX J1745.6−2901 based on the *ASCA* position([47]).

Table 6.2: *ASCA* SIS positions[a] $(\alpha_{\rm J2000}, \delta_{\rm J2000})$ of the hard and soft sources.

Date	Soft source	Hard source
'93 autumn	$(266.421, -29.006)$	$(266.401, -29.026)$
'94 autumn	$(266.414, -29.006)$	$(266.400, -29.026)$
'97 spring	$(266.414, -29.011)$	$(266.395, -29.028)$

a: The error including the attitude determination of *ASCA* is about $0'.4$.

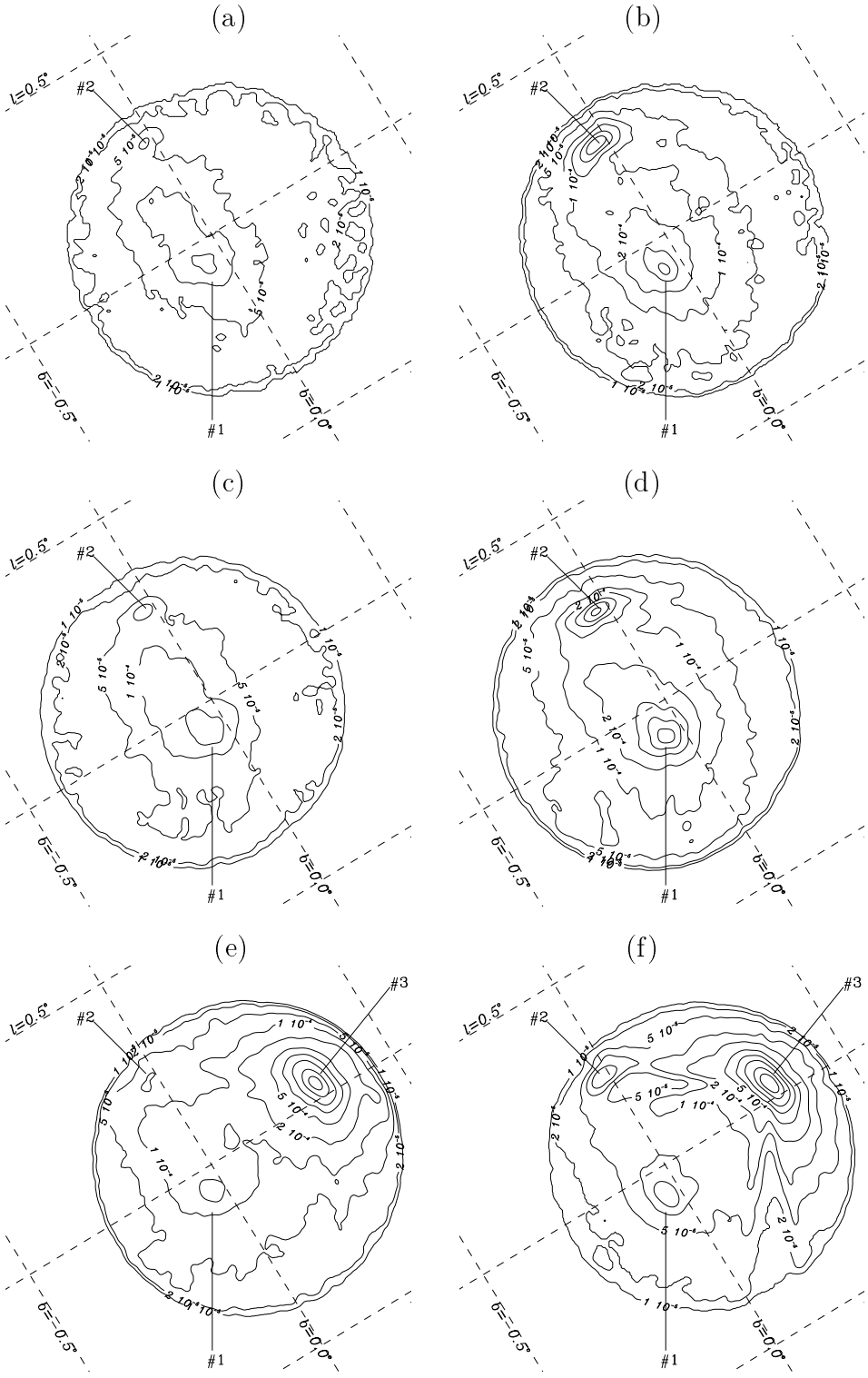

Figure 6.1: Smoothed GIS images of the Galactic center with the Gaussian function of 1 $\sigma = 2$ pixels ≈ 0.5 arcmin. The images observed during '93 autumn, '94 autumn and '97 spring are given in the upper(a,b), middle(c,d) and bottom(e,f) panels, respectively. The left and right figures are 1–3 and 3–10 keV band images, respectively. No corrections for vignetting and background-subtraction were applied.

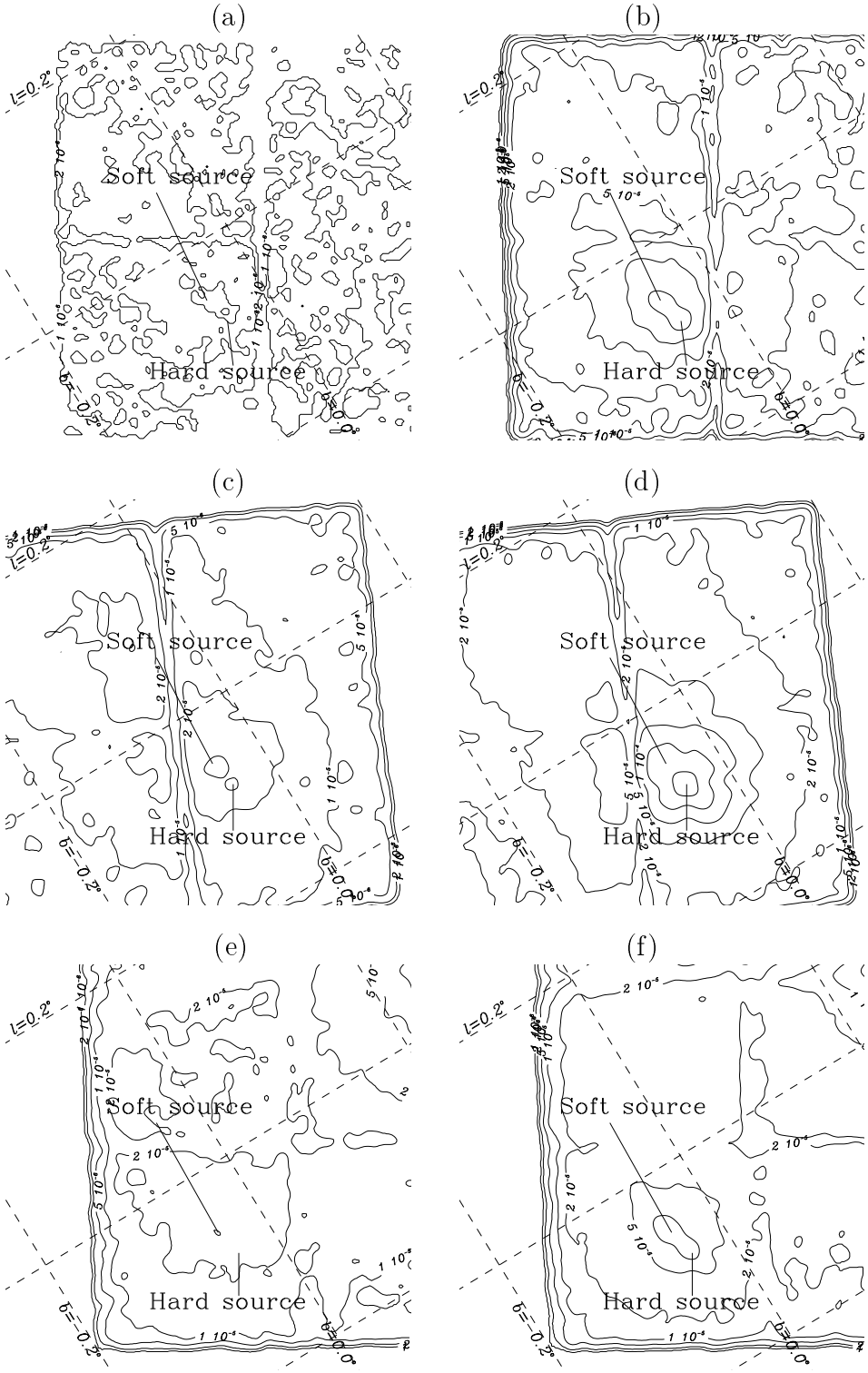

Figure 6.2: Same as figure 6.1 but for SIS. All the images were smoothed with the Gaussian function of 1 σ = 12 pixels $\approx$ 0.32 arcmin.

6.4 The Hard Source (AX J1745.6−2901)

6.4.1 Variability of the Hard Source

Long Time Variability

By comparing the hard X-ray images of figure 6.2, we can clearly see the flux variation of the hard source between the two observations separated by 1 and 3.5 years. In fact, after background subtraction, the X-ray flux of the hard source in '94 autumn was found to be about 5-times brighter than those in '93 autumn and '97 spring.

Short Time Variability

For a timing analysis of a short time-scale of $\sim$ 1 s, we used only the GIS data, because the SIS had no sufficient time resolution. We first made a light curve with a time resolution of 1 s from the circular regions of $6'$ radii, and found an X-ray burst in the '94 autumn data. The light curves in the 3–6 keV and 6–10 keV bands near to the X-ray burst with appropriate binnings are given in figure 6.3. The fluxes show a fast rise, followed by an exponential decay after $\sim$ 3 s of the peak. The decay time in the 3–6 keV band was found to be slower than that in the 6–10 keV band, indicating spectrum softening during the decay phase of the burst. Therefore, this burst is a typical type-I burst; hence, AX J1745.6−2901 is unambiguously classified to be a neutron-star binary with a low-mass companion star.

Moderate Time Variability

For a timing analysis of a moderate time-scale of $\sim$ 1 hour, we made the GIS light curve with a time resolution ($\sim$ minute) from the circular regions of $6'$ radii after removing the bursting phase. We found periodic flux dips from the '94 autumn data with about an 8.4-hour interval. By a folding technique, we found the periodicity of the dips to be 8.356$\pm$0.008 hr (90% error).

The folded GIS light curve with 8.356 hr taken from the circular region of $4'$ radii is given in figure 6.4c. From the periodicity of the dips and its deep trapezoidal shape, we infer that the dip is due to the eclipse of a companion star. The eclipse

duration was about 0.047 of the orbital phase, corresponding to an eclipse semi-angle θ_e of $\sim 8^\circ.5$. From this eclipse ephemeris, we found that the '93 autumn data had no dip data, which is due to the limited coverage of the orbit phase (figure 6.4a). Although the '97 spring observations fully covered the orbit, we found no apparent dip, which is due to the low signal-to-noise ratio. In order to improve the signal-to-noise ratio, we re-created a light curve taken from the smaller circular regions of $4'$ radii. The folded GIS light curves with 8.356 hr are given in figure 6.4e.

We found the candidate of dip duration of ~ 0.05 of the orbital phase around a phase 0.8 in figure 6.4e. The averaged count-rates of the eclipse from $\phi = 0.7617$ to 0.8164 and of the non-eclipse from $\phi = 0.8164$ to 0.7617 were found to be 0.363 ± 0.008 and 0.413 ± 0.002 counts s^{-1} (1 σ error), respectively. We can then estimate the significance of the dip detection using these count-rates and found the significance to be 6.3 σ for the 97 spring observation.

Since we found that the smaller region reduces the background ratio, we made the SIS light curve with the same time resolution ($\sim$ minute) as GIS, but from the smaller circular regions of $0'.8$ radii because the the SIS spatial resolution (roughly $0'.5$) is good enough to resolve two sources. The folded SIS light curves with 8.356 hr for the three observations are given in figure 6.4. We found the candidate of dip with duration of ~ 0.05 of the orbital phase around the phase 0.8 from the '97 spring data (figure 6.4f). The averaged count-rates of the eclipse from $\phi = 0.7617$ to 0.8164 and of the non-eclipse from $\phi = 0.8164$ to 0.7617 were found to be 0.0184 ± 0.0017 and 0.0340 ± 0.0006 counts s^{-1} (1 σ error), respectively. Therefore we found the significance to be 8.8 σ, which was higher than that of GIS. Since we also detected high-significant 8.4 hrs periodic eclipse from the SIS data of '94 autumn with 30σ significance (figure 6.4), we concluded that we detected the eclipse both in a high-state ('94 autumn) and in a low-state ('97 spring).

In the folded light curve in the high-state ('94 autumn), excess X-rays above the background level, even in the eclipsing phase, were found. We further made X-ray images during the eclipse phase of the '94 autumn & '97 spring, which are given in figure 6.5. In the high-state ('94 autumn), we can see a point-like source at the position of the hard source (figure 6.5b), with a flux level comparable to the hard source in a low-state; hence, confirmed the presence of an excess flux in the eclipse. The excess flux in the 3–10 keV band was roughly $\frac{1}{5}$ of that of the

non-eclipse. Although we also found the similar eclipse in '97 spring as seen in '94 autumn, we detected no significant excess flux with more than 2 σ confidence for the low-state data ('97 spring), which is due to the limited statistics.

6.4.2 X-Ray Fluxes and Spectra

The Persistent GIS Spectra

We made persistent X-ray spectra from the '94 autumn & '97 spring data using the non-eclipse phase from the circular regions of $4'$ radii for the GIS. The background data for the spectra were extracted from the same area, but during the eclipse phase ("background-1"). The spectra of '94 autumn & '97 spring after the background subtraction are given in figure 6.6. We fitted the GIS spectra to two simple models: a power-law and thermal bremsstrahlung, both modified by interstellar absorption, including Compton scattering, of the cosmic abundances (see Morrison & McCammon 1983[75]). These models were acceptable. The best-fit parameters are given in table 6.3. We also show the best-fit parameters for a power-law fit in figure 6.6.

We further made the high-state ('94 autumn) spectrum by subtracting the low-state ('93 autumn) normalized by the effective area ("background-2") and fitted to the same model. The best-fit parameters, $N_{\rm H} = 2.1(2.0\text{–}2.3) \times 10^{23}$ H cm^{-2} and a photon index of 2.8(2.7–3.0), are the same as those determined with the other background subtraction (background-1). We concluded that the best-fit parameters of the GIS spectrum have little dependence on the method of the background subtraction.

Furthermore, we fitted the high-state spectrum assuming the interstellar absorption with the different abundance ratio given in Anders & Grevesse (1989 [3]). The abundance ratio for each element coincides with each other within a factor of 2 between the two abundance tables. The best-fit parameters were $N_{\rm H} = 2.2(1.8\text{–}2.5) \times 10^{23}$ H cm^{-2} and a photon index of 2.4(2.1–2.8) for the spectrum applied the background-1 subtraction and $N_{\rm H} = 1.8(1.7\text{–}1.9) \times 10^{23}$ H cm^{-2} and a photon index of 2.7(2.6–2.9) for the background-2, respectively, which are not different by more than a few tens % of the cosmic abundance ratio from those given in Morrison & McCammon (1983 [75]). Here and after, we assumed the photo-electric cross section given in Morrison & McCammon 1983 ([75]) because the difference of the

best-fit parameters between the two assumptions of the abundance ratio is only a few tens %.

The Persistent & Eclipse SIS Spectra

For the '93 autumn and '97 spring observations (low-state), because of their limited fluxes, contamination from the nearby soft source became significant (cf. table 6.4). We thus made those spectra from a small region of $0'.8$ radius circle of the SIS. For a comparison, we made the '94 autumn spectrum (high-state spectrum) using the same method as those for the '93 autumn and '97 spring spectra. We made the background spectra from a $0'.7$–$2'.5$ radius annular region centered at the soft source, excluding an area of $0'.8$ radius from the hard source. About $\frac{1}{4}$ of the total X-rays from the hard source falls on the $0'.8$ radius circular region. The diffuse X-rays from the soft source are roughly spherically symmetric as is shown in figure 6.2. Since the spill-over X-rays from GRO J1744−28 in '97 spring to the region were expected to be $\sim$0.0025 counts s^{-1} (table 6.4), which was roughly 10% of the count rate of the hard source itself (0.015 counts s^{-1}). We also found that we can remove all these contaminations using the background which we made. Inversely, the spill-over X-rays from the hard source to the background region were subtracted from the source flux. However, these spill-over X-rays are only about 10%. We thus ignore this over-subtraction.

The spectra after the background subtraction are shown in figure 6.7. Since the statistics are limited for the low-state and eclipse spectra, we fixed the $N_{\rm H}$ value to that of the persistent in the high state. The best-fit parameters are listed in table 6.5 & 6.6. We can see that the best-fit power-law index and $N_{\rm H}$ values of the high-state spectrum are consistent with those determined with GIS (see table 6.3). We are, thus, confident that the background was properly subtracted in any case. As shown in table 6.5, the persistent flux of '93 autumn is the same as that of '97 spring but is about one fifth of '94 autumn. The photon index of '94 autumn in the persistent state is larger than that of '97 spring. From the high-state data, we can clearly see that the eclipse spectrum is much softer than the non-eclipse spectra.

6.4.3 The Burst Spectrum

Since the time resolution of SIS was insufficient (16 s), we only used the GIS data for the burst spectra. We made four time-sliced energy spectra, each with a 3–6 s exposure: the burst rise (exposure time = 3 s), the burst peak (6 s) and the burst decay (6 s each after the burst peak), from the circular region of $6'$ radius and subtracting the persistent flux in the same region. Since the statistics were limited, we fitted the burst spectra to a black-body model, fixing $N_{\rm H}$ to 2.6 $\times 10^{23}$ H cm^{-2} (see table 6.3). We plotted the best-fit temperature, luminosity and black-body radius as a function of the time in figure 6.8. We found that the temperature during the decay becomes softer as time passes, and that the black-body radius become constant during the decay phase. Such characteristics of the burst are typical of type-I bursts. For type-I bursts, the black-body radius at the decay phase is usually the same as the neutron star radius (r =10 km). From figure 6.8, if we use the distance of the hard source to be about 10 kpc, the black-body radius of the neutron star become reasonable, about 10 km. Hence, we suggest that the distance of the hard source is about 10 kpc, or more likely 8.5 kpc, geometrically near to the Galactic center. Then, the peak luminosity of the burst did not reach the Eddington luminosity of a neutron star, which is often the case of a small X-ray burst.

6.4.4 Discussion

Comparison with the Previous Observations

The persistent X-ray spectra in the high state ('94 autumn) were described with a power-law model with a photon index of about 2.2 (table 6.5), while the photon index in the low state was about 1.7 ('97 spring), which indicates the spectral hardening with decreasing flux. The change in spectral shape associated with the intensity decrease was often detected in low-mass X-ray binaries (for example, [70]).

The SAS 3 satellite found an X-ray burster (MXB 1743−29) in the Galactic center region ([55]). Within its rather large error region, several point sources, including the new X-ray burster (the hard source), were found. Therefore, the hard source is the most probable candidate of MXB 1743−29.

Constraint on the Binary Structure

Combining Kepler's law and the Roche geometry (e.q. [82]) and assuming that the ratio of the mass of the companion star ($M_{\rm opt}$) to the mass of the neutron star ($M_{\rm NS}$) is less than 0.8 ($M_{\rm opt}/M_{\rm NS} < 0.8$), we obtained the relation $(R_{\rm opt}/R_\odot)^3 = 0.013\ (M_{\rm opt}/M_\odot)P^2$, where $R_{\rm opt}$ is the radius of the companion and P is the orbital period in unit of hour. Using the present result of $P = 8.4$ hr, and assuming the mass-radius relation of Whyte and Eggleton (1980 [113]) for the main-sequence companion star and the Roche lobe overflow, the mass of the companion star is estimated to be $\sim 1.0\ M_\odot$; hence, the companion would be a G dwarf. This result is consistent with the low-mass X-ray binary predicted from the detection of the burst. For the neutron-star mass of 1.4 $M_\odot$, the semi-major axis of the binary system is estimated to be $\sim 2.7\ R_\odot$ by Kepler's law. Then, the orbital inclination angle i is found to be $\sim 70^\circ$, using the relation $R_{\rm opt} \approx a\ [\cos^2 i + \sin^2 i\ \sin^2\theta_{\rm e}\ ]$ for a circular orbit, where $\theta_{\rm e}$ is the eclipse semi-angle.

Excess Emission During the Eclipse

In order to examine the origin of X-rays found in the eclipse, we calculated the ratio of the eclipse spectrum to that of the high state (non-eclipse). The ratio was found to be energy dependent with a power-law index of $\sim$ 2–3. Since this power-law index is in the range expected from the dust-scattering cross section (power-law index ~ 2 within the optically thin limit) ([33]; [27]), we infer that the X-rays in the eclipse are due mainly to the dust-scattering.

Using a lunar occultation, Mitsuda et al. (1990 [71]) measured the spatial extension of the dust-scattered X-rays from another Galactic center transient source, GS 1741.2−2859/1741.6−2849. Using their data, we made a 2-dimensional distribution of the dust-scattered X-rays, and convolved it with the telescope point-spread function. We then found that 6% of the total photons can be detected in a $0'.8$ circular region on the average during the eclipse of the hard source. We also estimated that 25% of the direct X-rays fall on the same region. Although the flux ratio of the direct to scattered fluxes is a function of the X-ray energy, we estimate the energy-averaged ratio for simplicity. Then, as long as the scattering is single, the optical depth τ of the dust scattering can be estimated using the following

equation:

$$\frac{F_{\rm scattered}}{F_{\rm scattered}+F_{\rm direct}} = \frac{4F_{\rm eclipse}}{3F_{\rm eclipse}+F_{\rm high-state}} = 1-\exp(-\tau), \tag{6.3}$$

where $F_{\rm eclipse}$ is the observed flux in the eclipse, and is $\frac{1}{4}$ of the scattered flux $F_{\rm scattered}$; $F_{\rm high-state}$ corresponds to the direct flux $F_{\rm direct}+F_{\rm eclipse}$. Then, τ is given as

$$\tau = -\ln(1-\frac{4F_{\rm eclipse}}{3F_{\rm eclipse}+F_{\rm high-state}}). \tag{6.4}$$

Since the dust-scattering optical depth is roughly proportional to E^{-2}, we fit the data to

$$\tau = \tau_{\rm 1keV}E^{-2}, \tag{6.5}$$

and found that the $\tau_{\rm 1keV}$ is 14±3 with the $\chi^2 = 3.0$ (d.o.f. = 6). The best-fit result is given in figure 6.9.

Mitsuda et al. (1990 [71]) detected the dust-scattering from the transient GS 1741.2−2859/1741.6−2849, and found the optical depth of $\tau_{\rm 1keV}$ to be ~ 4. Although the hard source lies close to GS 1741.2−2859/1741.6−2849, it shows about a 4-times larger optical depth ($\tau_{\rm 1keV} \sim 14$). This can be understood to be due to a difference $N_{\rm H}$ values between these two sources. Predehl and Schmitt (1995 [86]), on the other hand, studied dust-scattering halos for 29 objects, and found a linear regression to be $\tau_{\rm sca}(1\ {\rm keV}) = 0.05 \times N_{\rm H}\ [10^{21}\ {\rm cm}^{-2}] - 0.083$. Using this relation and observed column density of 260 $\times[10^{21}\ {\rm cm}^{-2}]$, we estimate $\tau_{\rm sca}(1\ {\rm keV})$ of the hard source to be ~ 13. This is not largely different from $\tau_{\rm 1keV}$ of ~ 14, determined with the eclipse spectrum.

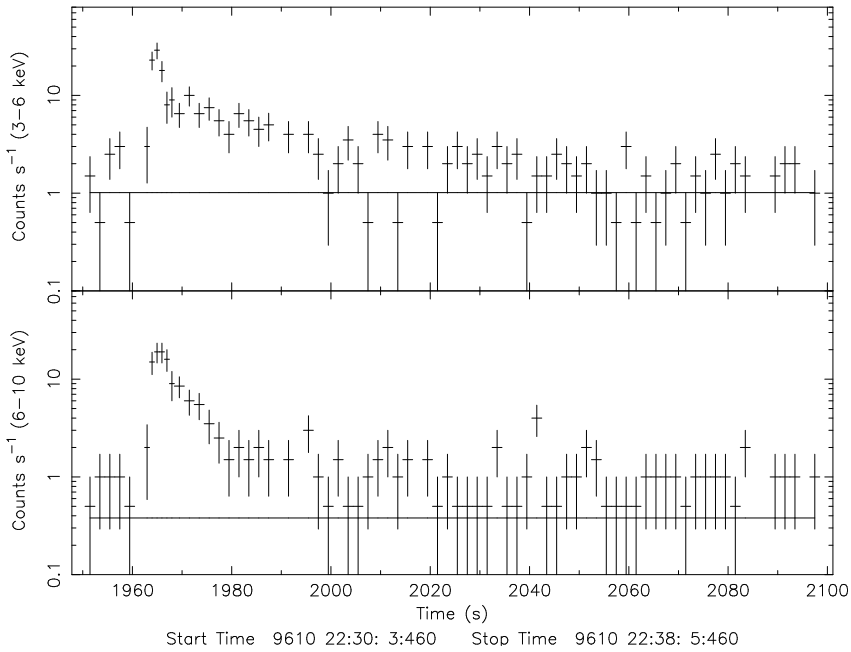

Figure 6.3: X-ray light curve of the hard source during the X-ray burst (GIS) in two different energy bands. The solid line is the averaged flux of the persistent X-ray during the eclipse. Error bars are 1σ.

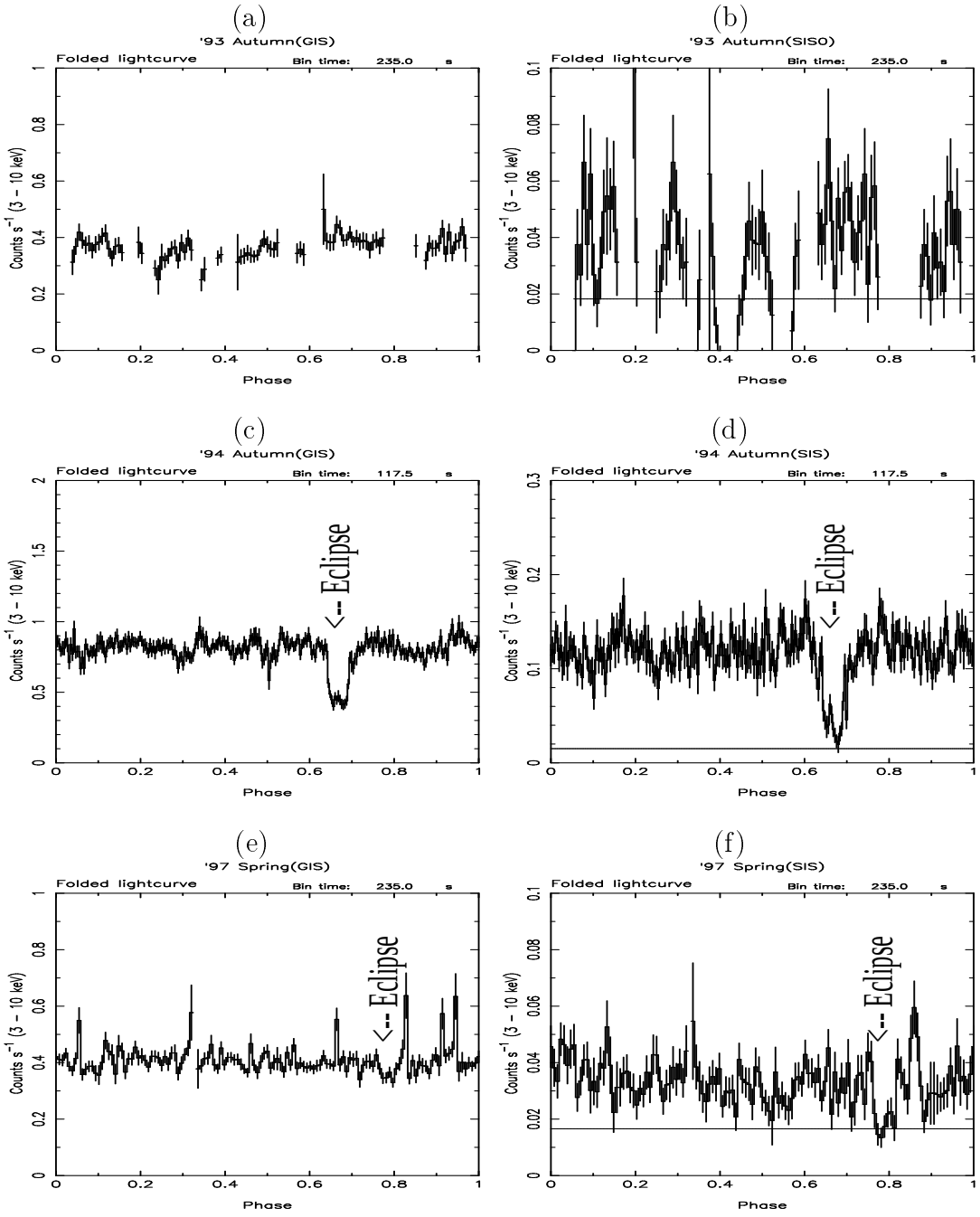

Figure 6.4: Folded light curves (3–10 keV) of the hard source. The folded light curves given in the right and left panels are taken from the circular region of $4'$ radii of GIS and from that of $0'.8$ radii of SIS, respectively. The folded light curves during '93 autumn (low state), '94 autumn (high state) and '97 spring (low state) are given in the upper (a,b), medium (c,d) and bottom (e,f) panels, respectively. All the folded periods are 8.356 hr. The phase 0 epochs for the '93 autumn, '94 autumn and '97 spring observations were set to MJD 49260.0, MJD 49610.0 and MJD 50523.0, respectively. Background is not subtracted. The solid lines given in the right panels are the background levels. Error bars are 1 σ.

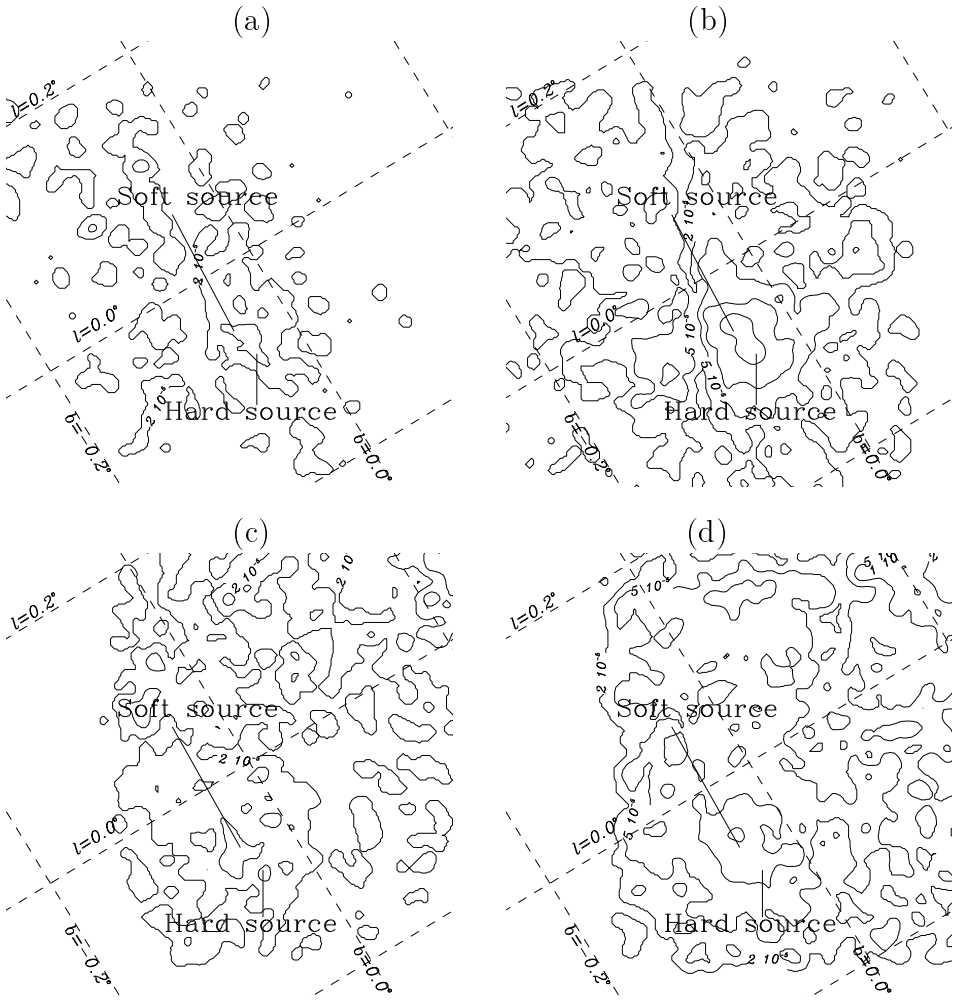

Figure 6.5: Same as figure 6.2 but for SIS in eclipse. The images observed during '94 autumn and '97 spring are given in the upper (a,b) and bottom (c,d) panels, respectively.

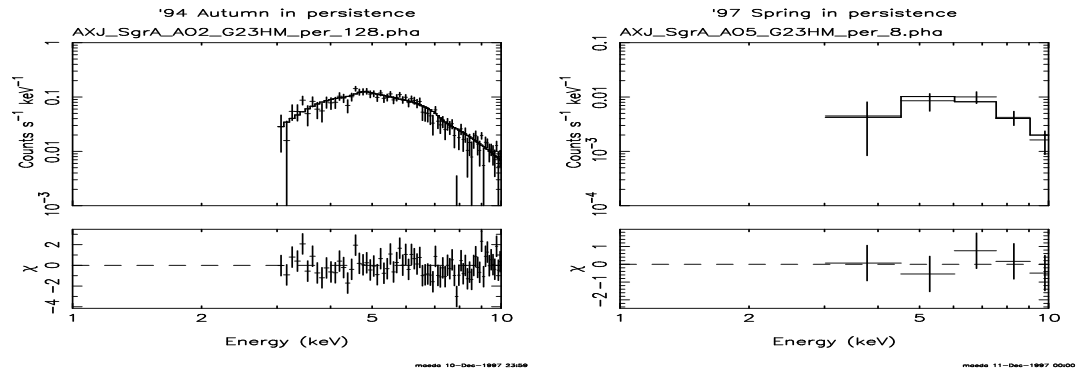

Figure 6.6: Persistent GIS spectra from the hard source. Right and left panels show the spectra obtained with the '94 autumn and '97 spring observations, respectively. The background was subtracted by the background-1 method (see text). Error bars are 1 σ. The solid lines correspond to the best-fit values with the power-law model, which are listed in table 6.3. Fit residuals are shown at the bottom of each panel.

Table 6.3: Simple model fits to the GIS spectra.

Model	Power-law	Bremsstrahlung
—— '94 autumn ————		
$N_{\rm H}{}^{b}$	2.6(2.2–3.0)	2.2(1.9–2.6)
Γ/kT^{c}	2.5(2.2–2.9)	6.7(5.1–9.2)
Normalization^{d}	0.23(0.11–0.49)	$6.9(5.1–9.7)\times10^{-2}$
$F_{3-10{\rm keV}}{}^{e}$	6.0×10^{-11}	6.0×10^{-11}
$L_{3-10{\rm keV}}{}^{f}$	1.9×10^{36}	1.3×10^{36}
χ^2(d.o.f)	67.74(71)	69.95(71)
—— '97 spring ————		
$N_{\rm H}{}^{b}$	2.6(fix^{a})	2.2(fix^{a})
Γ/kT^{c}	0.72(-0.41–+1.8)	>13
Normalization^{d}	$1.2(0.1–8.8)\times10^{-3}$	$<6.8\times10^{-3}$
$F_{3-10{\rm keV}}{}^{e}$	1.0×10^{-11}	9.5×10^{-12}
$L_{3-10{\rm keV}}{}^{f}$	2.3×10^{35}	1.8×10^{35}
χ^2(d.o.f)	1.150(3)	2.730(3)

Errors are 90% level.

a: $N_{\rm H}$ values were fixed to that of '94 autumn because of the limited statistics.

b: $N_{\rm H}$ $\times10^{23}$ H cm^{-2}

c: Γ and kT(keV) are photon index and temperature, for the power-law and thermal bremsstrahlung models, respectively.

d: $3.02\times10^{-15}/(4\pi D^2)$

e: $F_{3-10{\rm keV}}$ (erg s^{-1} cm^{-2})

f: $L_{3-10{\rm keV}}$ is the absorption-corrected luminosity (erg s^{-1}) at the distance of 8.5 kpc.

Table 6.4: Count rates[a] of the spill-over X-rays (1–10 keV band) from the three bright sources of SIS

	Net X-rays		Count rate of spill-over X-rays from		
	Hard source		Soft source	1E 1743[b]	GRO J1744[c]
(Phase)	Non-eclipse	Eclipse	Persistent	Persistent	Persistent
'93 autumn	0.017	–	∼0.01	(<0.001)	negligible
'94 autumn	0.10	0.024	∼0.01	(<0.001)	negligible
'97 spring	0.017	(0.0031)	∼0.01	(<0.001)	0.0025

a: The circular region of $0'.8$ radii centered at the hard source

b: 1E 1743.1−2843

c: GRO J1744−28

Table 6.5: Best-fit parameters to the non-eclipse SIS spectra

	'93 autumn	'94 autumn	'97 spring
$N_{\rm H}$ (H cm^{-2})	2.5×10^{23}(fix[a])	$2.5(2.4–2.7)\times10^{23}$	2.5×10^{23}(fix[a])
Photon index (γ)	1.8(1.3–2.2)	2.2(2.0–2.4)	1.7(1.4–2.0)
Normalization[b]	$1.0(0.5–2.2)\times10^{-2}$	$1.2(0.8–1.8)\times10^{-1}$	$9.4(5.7–15.4)\times10^{-3}$
$F_{3-10{\rm keV}}$ (erg s^{-1}cm^{-2})	1.1×10^{-11}	5.3×10^{-10}	1.2×10^{-11}
$L_{3-10{\rm keV}}$ (erg s^{-1})	2.6×10^{35}	1.4×10^{36}	2.8×10^{35}
χ^2(d.o.f.)	10.65(10)	35.23(22)	26.72(23)

The model used in these fits is a power-law model modified with the interstellar extinction of $N_{\rm H}$. Errors are 90% level.

a: $N_{\rm H}$ values were fixed to that of the '94 autumn because of the limited statistics.

b: (photons keV^{-1} cm^{-2} s^{-1} at 1 keV)

Table 6.6: Best-fit parameters to the eclipse spectra

	'93 autumn[a]	'94 autumn	'97 spring
$N_{\rm H}$ (H cm^{-2})	-	2.5×10^{23}(fix[b])	2.5×10^{23}(fix[b])
Photon index (γ)	-	5.6(4.3–7.1)	5.6(fix[c])
Normalization[d]	-	4.1(0.6–32.0)	$<$1.4
$F_{3-10{\rm keV}}$ (erg s^{-1}cm^{-2})	-	5.6×10^{-12}	$<2\times10^{-12}$
$L_{3-10{\rm keV}}$ (erg s^{-1})	-	3.1×10^{35}	$<1\times10^{35}$
χ^2(d.o.f.)	-	13.31(12)	7.256(6)

Same as table 6.5, but for in eclipse.

a: We found no significant eclipse.

b: $N_{\rm H}$ value was fixed to that of '94 autumn in non-eclipse (persistent) phase because of the limited statistics.

c: Photon index of '97 spring in eclipse was fixed to that of '94 autumn in eclipse because of the limited statistics.

d: (photons keV^{-1} cm^{-2} s^{-1} at 1 keV)

(a)

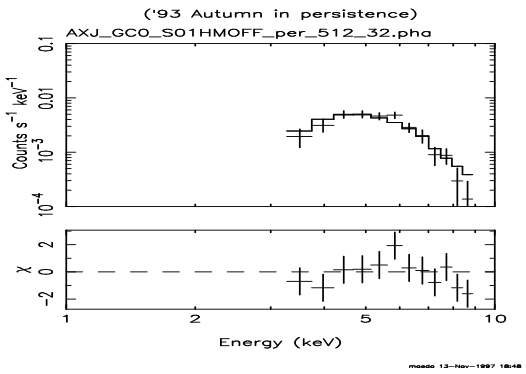

(b1)

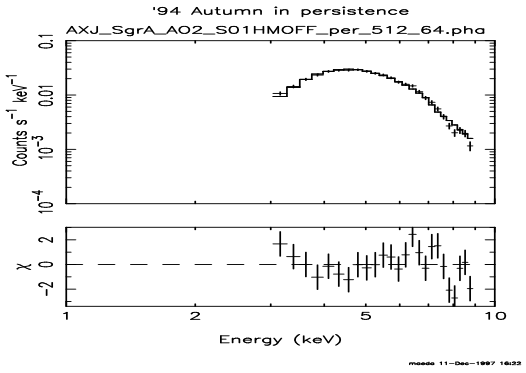

(b2)

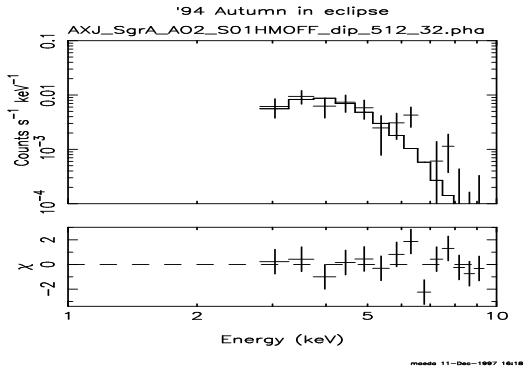

(c1)

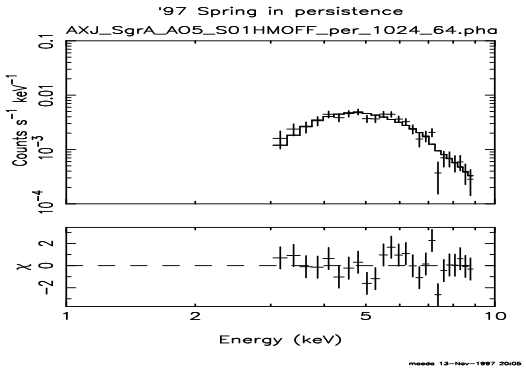

(c2)

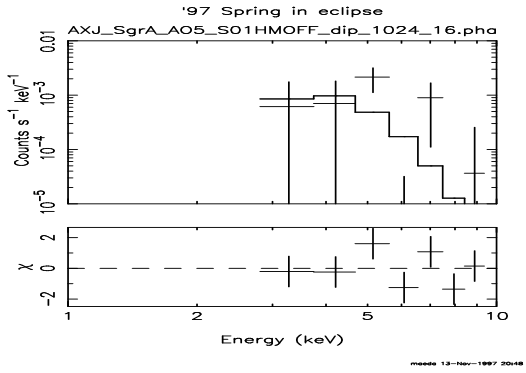

Figure 6.7: SIS spectra of the hard source and the best-fit power-law models in the three observations. The spectra observed during '93 autumn, '94 autumn and '97 spring are given in the upper (a), middle (b1,b2) and bottom (c1,c2) panels, respectively. The left and right figures are the spectra in non-eclipse and in eclipse phases, respectively. The solid lines show the best-fit parameters given in tables 6.5 & 6.6. Error bars are 1 σ. Fit residuals are shown at the bottom of each panel.

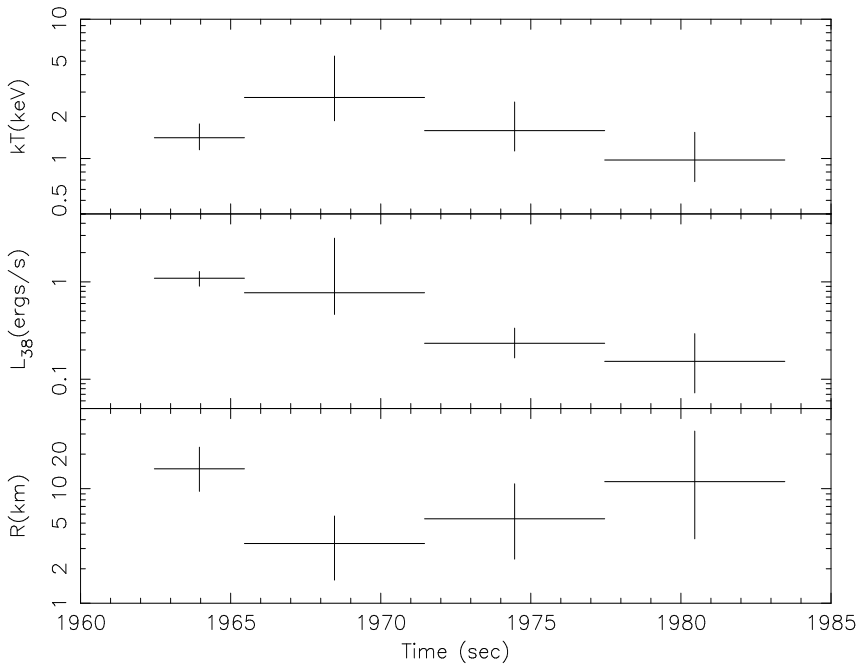

Figure 6.8: Best-fit parameters to the spectra during the burst, temperature [keV] (upper panel), bolometric luminosity[erg s^{-1}] (middle panel) and radius[km] (lower panel) normalized with the source distance of 10 kpc. We fixed $N_{\rm H}$ to 2.6×10^{23} H cm^{-2}. Errors are at the 90% confidence limits.

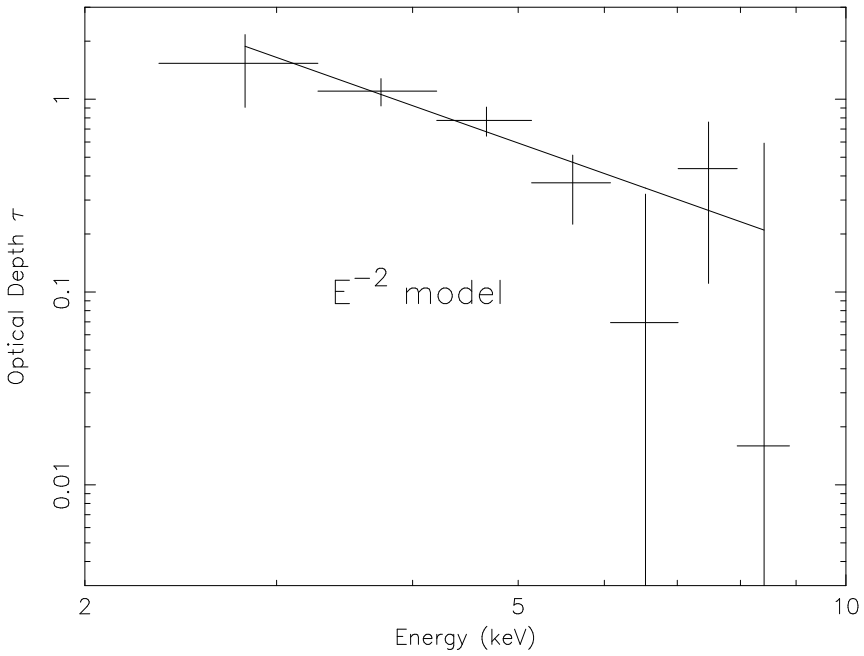

Figure 6.9: Optical depth as a function of the energy (see this text). The solid line shows the best-fit model. Error bars are 1σ.

6.5 The Soft Source (Bright Region around Sgr A*)

6.5.1 Time Variability

By comparing the soft and hard X-ray images of figure 6.2, we can see no flux variation of the soft source among the three observations. We also found no clear flux variation of the soft source on the various time-scale through the three observations.

6.5.2 Flux and Spectra

We made the SIS spectra from a "source region" of $2'.5$ radius circle centered at Sgr A*, excluding an area of $0'.8$ radius from the hard source. The raw (background-non-subtracted) spectra of this region include both the X-ray events from the soft source itself and backgrounds. The backgrounds are composed of the two components: the diffuse backgrounds including the non-X-ray and extragalactic backgrounds (so called CXB) and the spill-over X-rays from nearby bright sources. We made the background spectra from a $2'.5$–$4'.0$ radius annular "background region" centered at Sgr A*. Since we subtracted the background normalized by the integrated area, we removed the diffuse background component from the source spectra. As is shown in figure 6.1, we found, near Sgr A, the three bright sources the hard source, 1E 1743.1−2843 and GRO J1744−28. We estimated that ∼30%, ∼0.2% and ∼0.16% of the total X-rays from the hard source, 1E 1743.1−2843 and GRO J1744−28, respectively, fall on the source region using the XRT point-spread function ([92]). As the total count rates of 1E 1743.1−2843 show less than 1 counts s^{-1} GIS^{-1} through the three observations, we derived the spill-over count rate of 1E 1743.1−2843 to be about less than 0.002 counts s^{-1} SIS^{-1}, which is less than ∼2% of the count rate of the soft source ($\sim$ 0.1 counts s^{-1}). We then found that we can ignore the contamination from 1E 1743.1−2843. The spill-over X-rays from GRO J1744−28 in the persistent phase to the source and background region were estimated to be $\sim$ 0.16% and $\sim$ 0.29% of the total X-rays from the GRO J1744−28. The contamination to the source region from GRO J1744−28 is expected to be roughly 0.02 counts s^{-1}, which is about 20% of the count rate of the soft source itself. The count rate of the spill-over X-rays to the source region was derived

to be about 0.54 times as that to the background region. The area of the source region is 0.537 times as that of the background region. We then found that we could remove the contamination of GRO J1744−28 with the background spectra normalized by the integrated area. We estimated that about $\frac{3}{10}$ and $\frac{1}{4}$ of the total X-rays from the hard source fall on the source and background regions, respectively, assuming that the hard source is a point-like source. If we use the area-normalized method for background-subtraction, about $\frac{1}{20}$ of the total X-ray photons of the hard source remains in the background-subtracted spectra. We further subtracted this remained X-rays using the best-fit value given in tables 6.5 and 6.6. However, the hard source may make a small halo of the size of roughly 1.5 arcmin radius by the interstellar dust scattering (see section 6.4.4). In this case, we might not derive the exact estimate of the spill-over X-rays using the above method. The raw soft-source spectrum during the non-eclipse phase of the hard source in the '94 autumn observation included a large amount of the spill-over X-rays from the hard source which became comparable to the events of the soft source itself. Therefore we did not use this data for our spectral analysis. The spill-over X-rays from the soft source to the background region are subtracted from the source flux. However, the over-subtractions by these spill-over X-rays become roughly 15%, which are nearly constant (within $\sim \pm 1\%$) among the three observations. We thus ignore this over-subtraction.

6.5.3 The '93 Autumn SIS Spectrum

Background-subtracted SIS spectrum in '93 autumn is shown in figures 6.10 . Several emission lines, which can provide key information for the origin of the X-rays, are found in the spectrum. We have determined the line energy, flux and equivalent width and summarized them in table 6.8. Kα lines from helium-like ions of silicon, sulphur, argon, calcium and iron atoms were detected in the SIS spectrum. The significant 6.4 keV line from the neutral iron atoms was not detected in the spectrum.

Single-Component NEI Plasma Model

As is given in figure 6.10, the presence of these highly ionized heavy atoms indicates that the X-rays are attributable to an optically thin thermal plasma. Furthermore,

co-existence of emission lines from a lighter element (e.g. silicon) and heavier element (e.g. iron) suggests a multi-temperature structure or non-equilibrium ionization (NEI) state or both. Since no significant 6.4 keV line was found, we can ignore this component. Therefore we start our spectral analysis with the conventional NEI model often applying for the thin thermal plasma observed from SNR: the model for coronal plasma with keeping constant electron temperature after a shock heating. The model describes the thin thermal plasma with a single electron-temperature $kT_{\rm e}$, a single ionization-time-scale $n_{\rm e}t(\int n_{\rm e}(t')dt')$, elemental abundance z, and a normalization factor Norm. $\equiv \int n_{\rm H}^2 dV/(4\pi D^2)$, where $n_{\rm e}$, t, $n_{\rm H}$, V and D are the mean electron density, elapsed time after the plasma was heated to the temperature $kT_{\rm e}$, mean hydrogen density, plasma volume and distance to the plasma. We used the NEI code developed by Masai ([64]). This model incorporates the X-ray emission from thirteen elements (H, He, C, N, O, Ne, Mg, Si, S, Ar, Ca, Fe and Ni). We modified this model with the interstellar absorption along the line of sight using the cross section, including Compton scattering, of Morrison & McCammon (1983 [75]).

Due to the limited energy range, we could find only several emission lines from Si, S, Ar, Ca, Fe and Ni (by K-shell transitions). Therefore we assumed the cosmic ratios for all the twelve elements (He–Ni), but allowed for the global abundance Z to vary in our fits. The best-fit parameters were given in figure 6.11 & table 6.9. As given in figure 6.11, this simple NEI model well reproduces the iron K-line and continuum, while it does not reproduce the emission lines from Si and S. Another component is required in order to explain the emission lines from Si and S.

6.5.4 The Flux & Spectral Shape of the Three Observations

In order to study the flux variations of the soft source, we have fitted the spectra obtained by the follow-up observations ('94 autumn & '97 spring) with the same model given in section 6.5.3. For simplicity, we assumed the continuum shape & flux and the line energies & fluxes fixed to the best-fit parameters given in table 6.8 but allowed to vary a global normalization. The best-fit parameters were given in table 6.10 & figure 6.10. These models reproduce the spectral shapes of the two spectra obtained with the follow-up observations, which are characteristic of the flat

continuum and many emission lines with the low-energy absorption. The absolute flux of the '93 autumn observations is coincided with that of the '97 spring, but roughly 20% larger than that of the '94 autumn. During '93 autumn & '97 spring, the soft source was located at the positions more than $\sim 1.5'$ arcmin away from the CCD gaps of SIS. On the contrary, the soft source was located very near the edge (only $\sim 0.7'$ for SIS1) of the CCD gaps during '94 autumn, where the unknown systematic-uncertainty for the flux estimation would increase. Furthermore, the SIS data in '94 autumn were obtained with the 4CCD-BRIGHT-mode. As is discussed in appendix D, the detection-efficiency in '94 autumn might become roughly 85% of the other observations because of the radiation damage in space. If we correct this decrease of the detection-efficiency, the fluxes of the three observations become the same within their statistical errors. Therefore we can safely conclude that the flux and spectral shape of the soft source are nearly constant with the flux level around 2×10^{-11} erg s^{-1} cm^{-2} (2–10 keV) among the three observations.

Table 6.7: Count rates of the spill-over X-rays (1–10 keV band) from the three bright sources to the SIS region

	Net X-rays	Count rate of spill-over X-rays from			
	Soft source	Hard source		1E 1743[a,b]	GRO J1744[a,c]
Phase	Persistent	Non-eclipse	Eclipse	Persistent	Persistent
'93 autumn	0.1	0.025	–	(<0.002)	negligible
'94 autumn	0.1	0.15[d]	0.039	(<0.002)	negligible
'97 spring	0.1	(0.024)	0.0050	(<0.002)	0.023

a: We can subtract these spill-over X-rays using our backgrounds (see this text).

b: 1E 1743.1−2843

c: GRO J1744−28

d: This became comparable to the events of the soft source itself. Therefore we did not use this data during the non-eclipse phase of the '94 autumn observation.

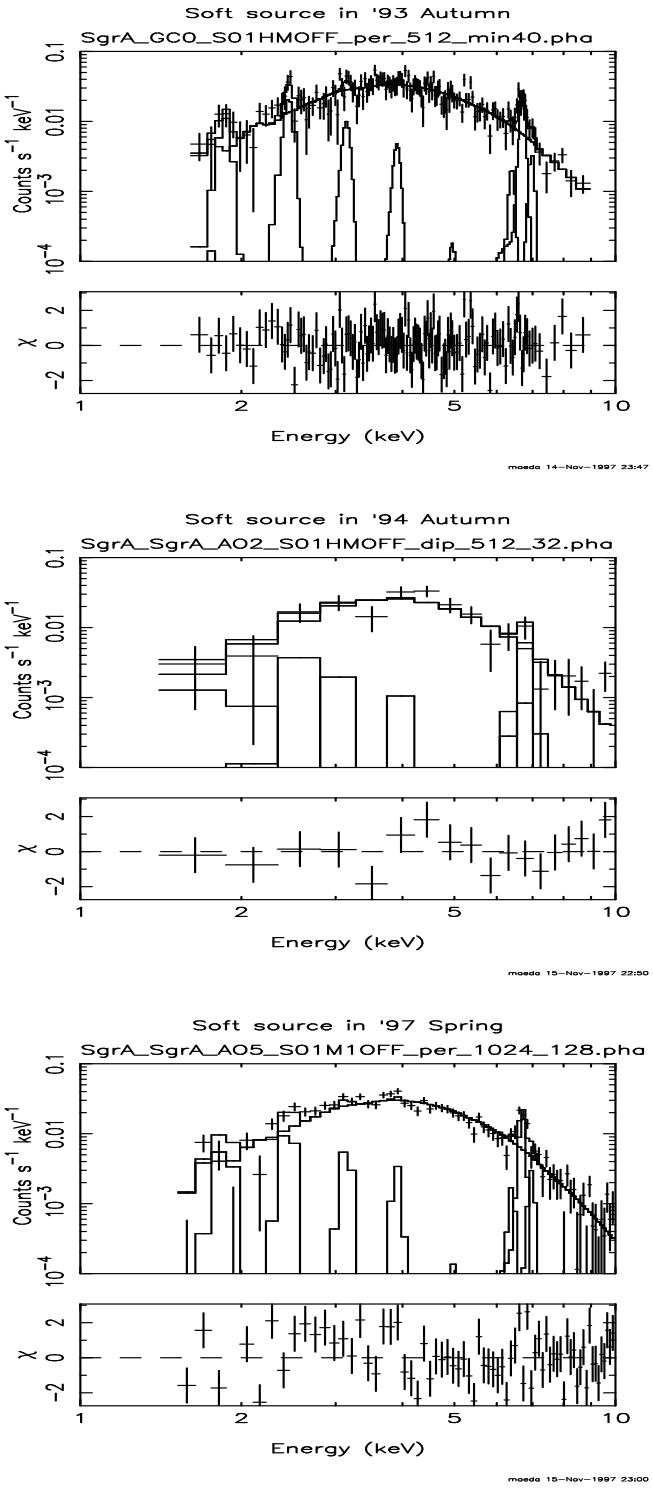

Figure 6.10: The SIS spectra of the soft source. Top, middle and bottom panels show the spectra obtained with the '93 autumn, '94 autumn and '97 spring observations, respectively. Error bars are 1 σ. The solid line corresponds to the best-fit value with the multi-line fits as summarized in tables 6.8 & 6.10. Fit residuals are shown at the bottom of each panel.

Table 6.8: Results of the multi-line fits to the SIS spectrum of the soft source in '93 autumn

——Continuum——			
$N_{\rm H}$ (H cm^{-2})			8.1(6.9–9.4)$\times 10^{22}$
kT (keV)			9.5(6.0–20.3)
Normalization[a]			8.7(7.3–11.4)$\times 10^{-3}$
——Emission lines——			
(Element)	(Line name)	(Line center(keV))	(Line flux(photons s^{-1} cm^{-2}))
Si	He-like Kα	1.86(fix[b])	1.7(0.7–2.7)$\times 10^{-5}$
S	He-like Kα	2.45(fix[b])	3.8(2.2–5.4)$\times 10^{-5}$
Ar	He-like Kα	3.14(fix[b])	1.6(0.1–3.0)$\times 10^{-5}$
Ca	He-like Kα	3.90(fix[b])	$<2.2\times 10^{-5}$
Fe	Neutral Kα	6.4(fix[b])	$<3.4\times 10^{-5}$
	He-like Kα	6.7(fix[b])	1.3(1.0–1.7)$\times 10^{-4}$
	H-like Kα	6.97(fix[b])	$<5.6\times 10^{-5}$
——X-ray flux & luminosity——			
$F_{\rm x}$(2–10 keV) (erg s^{-1} cm^{-2})			1.9×10^{-11}
$L_{\rm x}$(2–10 keV) (erg s^{-1})			2.9×10^{35}
χ^2(d.o.f.)			135.5(129)

The observed line flux was determined by fitting a model of 7 Gaussian lines and an absorbed thermal bremsstrahlung to the data in 1.5 - 10 keV band. Line width is fixed to zero because of the limited statistics. Errors are 90% level.

a: $3.02 \times 10^{-15} \int n_{\rm e} n_{\rm i} dV \ / \ (4\pi D^2)$, where $n_{\rm e}$ is the electron density (cm^{-3}), $n_{\rm i}$ is the ion density (cm^{-3}), and D is the distance to the source (cm). $n_{\rm e} = 1.08 \times n_{\rm i}$.

b: Line energy is fixed to the theoretically predicted value because of the limited statistics.

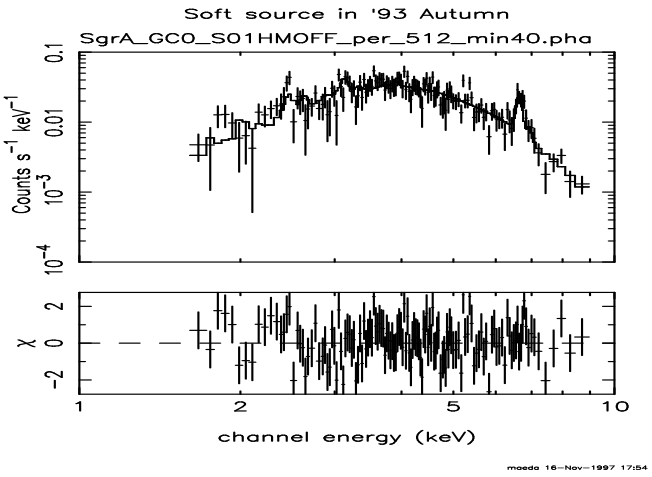

Figure 6.11: Results of the NEI plasma model fits to the soft source spectrum obtained with the '93 autumn observations. By the solid lines, we show the best-fit values obtained with the single-component NEI plasma model listed in table 6.9. Fit residuals are shown at the bottom of the panel. Error bars are 1σ.

Table 6.9: Best-fit results of the single-component NEI plasma model fit('93 autumn)

$N_{\rm H}$ (H cm^{-2})	$8.3(7.2\text{–}9.4)\times10^{22}$
kT (keV)	11.9(7.5–23.5)
$\log n_{\rm e}t$(cm^{-3} s)	10.9(10.7–11.0)
Z	0.51(0.32–0.68)
Normalization^a	2.2(1.9–2.7)
χ^2(d.o.f.)	152.4(134)

Errors are 90% level.

a: $10^{-12}\int n_{\rm H}^2 dV/(4\pi D^2)$.

Table 6.10: Fluxes of the three observation

Observation date	Global Norm.[a]	$\mathrm{Flux}_{2-10\mathrm{keV}}$(erg s^{-1} cm^{-2})	χ^2(d.o.f.)
'93 autumn	$1.00(\pm 0.04)$	$1.92(\pm 0.08)\times 10^{-11}$	135.5(138)
'94 autumn	$0.78(\pm 0.11)$[b]	$1.50(\pm 0.21)\times 10^{-11}$	15.95(17)
'97 spring[c]	$0.99(\pm 0.03)$	$1.90(\pm 0.06)\times 10^{-11}$	136.1(71)

Errors are 90% level. All the errors include only the statistical errors. The systematic errors would be larger than the statistical ones.

a: Normalized by the best-fit parameters given in table 6.8.

b: The systematic decrease of the detection-efficiency in the '94 autumn observations was estimated to be roughly 15% of the other two observations using equation D.1 in appendix D. Note that the best-fit value listed in this table does not include this systematic decrease.

c: The '97 spring data obtained with the 4CCD-mode showed the worse energy resolution and the smaller effective area than that with 1CCD because of the radiation damage (see appendix D), which grew up with the passing time since the *ASCA* launch. In this analysis, since we concentrated to research the spectral similarity among the three observations, we preferred the data with the more similar energy resolution and detection-efficiency of the first observations performed in '93 autumn. Therefore we used only the SIS data obtained with the 1CCD-mode for the '97 spring observations (cf. appendix D).

Chapter 7

Discussion

7.1 Brief Summary of Observational Results

In chapters 4–6, we analyzed the *ASCA* data and reported its results. Then we discuss about high energy phenomena in this chapter. However the results given in chapters 4 & 5 may be felt fairly complex. Therefore we briefly summarize the results in chapters 4 & 5 before discussing.

SIS results in the Galactic Center Region

We performed the mapping covering one square degree in the Galactic Center region with *ASCA*.

- We have detected the Kα-lines from helium-like and hydrogen-like ions of silicon, sulphur, argon, calcium, and iron over $1^\circ \times 1^\circ$ (figure 4.3). For each element, the fluxes of the Kα-lines from helium-like ions are more powerful than those from hydrogen-like ions. The iron Kα-lines from highly ionized ions is significantly broadened (figure 4.4). The S He-like and Fe He-like lines have a bright spot around Sgr A* (figure 4.9). The Fe He-like line is symmetrically extending along the Galactic plane on either side of Sgr A*, while the spatial distribution of the He-like sulphur is highly asymmetric (figure 4.9). The flux-ratio and the equivalent widths of the sulphur and iron K-lines from helium-like and hydrogen-like ions are roughly constant from field to field.

- A significant 6.4-keV iron line due to the fluorescence from neutral irons or ions below Fe XVII is present over $1^\circ \times 1^\circ$. There are two bright regions in the 6.4-keV line, which are well correlated with the dense molecular clouds.

GIS results around the Galactic Center Region

We performed the Chris-cross mapping toward about ten degrees away from the Galactic Center region with *ASCA*.

- We have detected the broad iron Kα-line with the center energy of about 6.6 keV from each observed field (figure 5.6). We can also reproduce these iron lines with the 6.4- and 6.7-keV lines. The iron 6.4-keV shows the high surface brightness and large equivalent width in the fields including the giant molecular clouds (figures 5.7 & 5.8). The equivalent widths of the iron 6.7-keV line are roughly constant from field to field (figure 5.8). The surface brightness of the iron 6.7-keV line becomes a peak at the Galactic center and smoothly decreases along and perpendicular to the Galactic plane (figure 5.7).

- We have also detected the Kα-lines from helium-like ions from silicon, sulphur, argon and calcium (figure 5.10). All the surface brightness of these four lines have a peak at the Galactic center (figure 5.11). These four Kα-lines show the monotonous decrease of the surface brightness from the Galactic center along and perpendicular to the Galactic plane with the various decreasing scale. Only the silicon Kα-line has a second peak around $|b| = 1^\circ$ along the direction perpendicular to the Galactic plane. The equivalent width of the silicon Kα-line is nearly constant from field to field (figure 5.12). The equivalent widths of the sulphur, argon and calcium are also nearly constant along the Galactic plane, but decrease perpendicular to the Galactic plane.

- The flux-ratios of the silicon to the sulphur Kα-line normalized by that of the iron Kα-line in the GC-series fields is estimated to be similar to those in the GP-series fields, but smaller than those in the GB-series fields (figures 5.14 & 5.15).

7.1.1 Classification of the Diffuse X-ray Emission

In section 5.4.2, we determined the scale lengths of the surface brightness of the iron 6.7-keV line by the double exponential-decay model. We then classify the diffuse emission to two components based on the scale lengths of the iron 6.7-keV line. The one component has the lower scale lengths of $0^\circ.42$ and $0^\circ.19$ along the longitudinal and latitudinal directions, respectively (hereafter "the Galactic Center emission"). The Galactic Center emission dominates in the inner $\sim 1^\circ$ and $\sim 0^\circ.5$ regions along the longitudinal and latitudinal directions, respectively. The other component has the larger scale lengths, which is called "the Galactic ridge emission".

7.2 The Galactic Center Emission

The fields dominated by the Galactic Center emission correspond to the GC-series fields. Then we discuss this emission mainly using the SIS results reported in chapter 4. In chapter 4, we confirmed the presence of a thin thermal plasma (hereafter "the Galactic Center plasma") with the distinct Kα-lines from highly ionized ions of the various elements. We also found the molecular clouds with the fluorescent iron 6.4-keV line (hereafter "the X-ray reflection nebula"). We separately discuss them in the following sections.

7.2.1 The Galactic Center Plasma

As shown in figure 4.6, the H-like/He-like flux-ratio of the iron Kα-line is roughly constant. The temperature inferred from the H-like/He-like flux-ratio of iron is to be about $10^{8.0}$ K (≈ 9 keV) assuming the plasma model in ionization-equilibrium ([68]). For a high temperature plasma of $kT \sim 9$ keV in ionization equilibrium, silicon, sulphur, and argon atoms (lighter elements) are expected to be fully ionized. If we assume the single temperature plasma model in non-ionization-equilibrium, the H-like/He-like flux-ratios of these lighter elements become larger than that of heavier one (iron) ([64]). However, the H-like/He-like flux-ratios of these lighter elements obtained from the averaged spectra are smaller than that of the iron (figure 7.1), which means that a single temperature plasma model either in ionization equilibrium or non-equilibrium is unsuitable for the Galactic Center plasma. The presence of intense lines from helium-like ions of these elements thus suggests that

the Galactic Center plasma consists of at least two different components. Then we separately discuss the Kα-lines of lighter (silicon, sulphur, argon and calcium) and heavier(iron) elements.

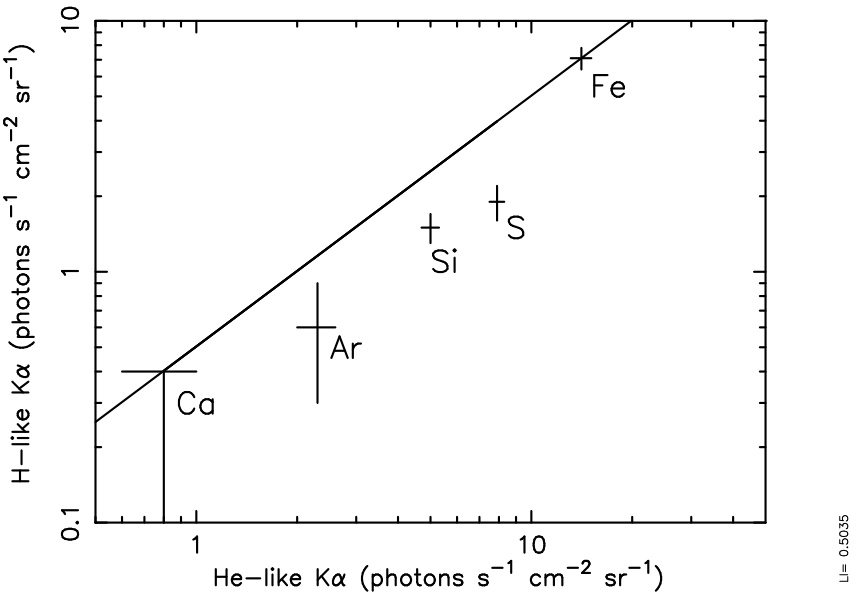

Figure 7.1: Correlations between averaged surface brightness of Kα-lines from He-like and H-like ions for each element, respectively. The solid lines means the line-ratios of the iron line. See also table 4.1. Error bars are 90%.

Kα-Lines from Highly Ionized Ions of the Lighter Elements

Long et al. (1981 [60]) carried out the survey of the Large Magellanic Cloud (LMC) with the imaging X-ray telescope aboard the *Einstein* Observatory. They found most of X-rays in the 0.15–4.5 keV band come from four X-ray binaries and a few tens supernova remnants. We found that most of the X-rays near the Galactic Center come from the three X-ray binaries and diffuse emission (figure 4.1). A superposition of the supernova remnants is a candidate of the Kα-lines of the lighter elements in the Galactic Center emission.

Hayashi (1997 [30]) performed the systematic study of the bright supernova remnants in the LMC with *ASCA*. He found intense Kα-lines from the helium-like ions of magnesium, silicon, sulphur, argon and calcium from the spectra of

the supernova remnants in the LMC, though the flux and equivalent width vary depending on their ages and types. He also detected Kα-lines from the hydrogen-like ions of these elements but with much fainter flux than those from the helium-like ions. These characteristics of Kα-lines are also seen in the spectra of the Galactic supernova remnants (cf. [48]; [103]). The small H-like/He-like flux-ratios of the Kα-lines of each lighter element in the Galactic Center plasma give support to the supernova scenario (figure 4.6). Note that there is no supernova remnant which exhibits a intense iron Kα-line from helium-like and hydrogen-like ions. The supernova remnants are not a major contributor to the iron K-lines.

Long et al. (1981 [60]) detected the 26 supernova remnants and 15 candidates in the LMC. The integrated luminosity of these 41 sources were estimated to be about 2×10^{38} erg s^{-1} (0.15–4.5 keV). We assumed that a supernova remnant has a thin thermal spectrum ([90]) of the solar abundance ([3]) with the temperature of 1 keV. After modifying with $N_{\rm H} = 2\times10^{21}$ cm^{-2}, which is appropriate for sources in the LMC, we converted this integrated luminosity into the 2–4 keV band. The luminosity in the 2–4 keV band is calculated to be 1×10^{37} erg s^{-1}.

The 2–4 keV flux observed in the 1 square degree of the Galactic center region is 1.9×10^{-11} erg s^{-1} cm^{-2} (table 4.1). The luminosities in the 2–4 keV band corrected with the interstellar absorptions of 6×10^{22} and 1×10^{23} H cm^{-2} are calculated to be 6.1×10^{36} and 1.2×10^{37} erg s^{-1}, respectively, at the distance of 8.5 kpc. Although the luminosity in the 2–4 keV band largely depends on the interstellar absorption, these luminosities are comparable to that of the integrated luminosity of the supernova remnants in the LMC. Therefore the 10$\sim$100 supernova remnants would be contained in the 1 square degree of the Galactic center region. A typical kinematic energy of 10^{51} erg is released by a type-Ia supernova explosion ([30]). Assuming the type-Ia explosion, the hot gas of 10–100 M$_\odot$ with the kinematic energy of 10^{52-53} erg is being supplied into the interstellar medium in the Galactic Center

The total stellar mass in the LMC is $\sim1\times10^{10}$ M$_\odot$ ([1]), while that in the inner 100 pc region from the Galactic Center is $\sim1\times10^{9}$ M$_\odot$ ([24] and reference therein). Since the LMC and Galactic Center roughly have the comparable number (10$\sim$100) of supernova remnants, a supernova rate per stellar mass in the Galactic Center is more than that in the LMC (roughly 10-times).

The two regions in the S He-like Kα-line, i.e., around ($l_{\rm II}$,$b_{\rm II}$) = (0.15, $-$0.11)

near Radio Arc and around (−0.20, −0.23) are bright (figure 4.9). These regions have roughly 0°.1 diameters, which is equivalent to 15 pc at 8.5 kpc. Since this size is typical for a supernova remnant with the age of 10^3–10^4 yr, it is conceivable that these two regions are candidates of supernova remnants. Note that these two regions show no peaks at the Fe He-like Kα-line, which demands another contributor for this line.

One of the most important discoveries of the *ASCA* Galactic plane survey is the X-ray detections from several supernova remnants from the Galactic plane (cf. [48]). All the supernova remnants except for G347.5−0.5, were found to exhibit the Kα-lines from the highly ionized ions. These supernova remnants were found to show not only shell-like structures but also central-filled ones. The lacking of the shell-like structure in the narrow band image at the He-like sulphur Kα-line (figure 4.9) may be consistent with the supernova-remnant origin.

As shown in figure 4.6, the H-like/He-like flux-ratio of the sulphur Kα-line is roughly constant from field to field. The equivalent widths of the Si He-like and S He-like Kα-lines are also roughly constant. Since the line flux and equivalent width of supernova remnants vary depending on their ages and types ([30]), the uniformity of the line flux-ratio and equivalent width would be a case of nearly isotropic supernova explosions. We conclude that a superposition of supernova remnants is the origin of Kα-lines of the lighter elements.

Iron Kα-Lines from Highly Ionized Ions

The GIS continuum in the 3.5–9 keV band can be described by a thermal bremsstrahlung spectrum with kT ∼10–30 keV (figure 5.9). The result is roughly consistent with $kT \sim 10$ keV obtained from the *Ginga* observation with a wider energy band ([51]; [108]). The temperature derived from the H-like/He-like flux-ratio of the iron Kα-line is about 9 keV with the assumption of ionization equilibrium, which roughly coincides with that derived from the GIS continuum. We conclude that the continuum will mainly come from the plasma emitting the iron Kα-lines. Thus the contributor of the iron Kα-line from highly ionized ions must reproduce the continuum emission.

From the GIS analysis, we derived the iron 6.7-keV line to be the scale lengths of about 0°.42 and 0°.19 along and perpendicular to the Galactic plane, respec-

tively (table 5.2). From the narrow energy-band map of SIS, the iron He-like line is symmetrically extending along the Galactic plane on either side of Sgr A*. Becklin & Neugebauer (1968 [8]) performed the near-infrared observations, which are dominates by the light of late-type giants and supergiants. They found the surface brightness distribution is aligned with the Galactic plane and has a minor axis ratio of about 0.5 on scales of $\sim$0.3 degree. These distribution of the near-infrared light is similar to that of the iron 6.7-keV(He-like) line.

Thus the possible origin of the iron Kα-lines from the highly ionized ions would be an integrated emission of faint point sources, which have a intense He-like and H-like line in their spectra (figure 4.3 & table 4.1).

The cataclysmic variable (CV; white dwarf binary) is known to exhibit these intense iron lines. For example, the equivalent widths of EX Hya were found to be 354 eV for the Fe He-like Kα-line and 141 eV for the H-like ([22]), which extremely resemble those seen in the Galactic Center emission : 390$\pm$30 eV for the iron He-like and 200$\pm$20 eV for the iron H-like (table 4.1). AO Psc also shows the similar equivalent width of 238^{+82}_{52} eV and 78^{+39}_{52} eV for the Fe He-like and H-like Kα-lines, respectively ([31]). Ishida (1992 [37]) found that the temperature of CVs determined by continuum emission is 10–40 keV, which is similar to that of the Galactic Center plasma.

He also found the flux of the iron Kα-lines from EX Hya to be 6×10^{-4} photons s^{-1} cm^{-2}. Assuming the distance of 100 pc to EX Hya, the absorption-uncorrected luminosity of these two lines from the $\sim$1 square degree field of the Galactic Center is corresponding to about 10^5 of that from EX Hya. The stellar mass density near the Sun is found to be $\sim$0.15 $M_\odot$ pc^{-3} ([1]), while that in the inner 100 pc region from the Galactic center was $\sim2\times10^2$ $M_\odot$ pc^{-3} ([24] and reference therein). Therefore the stellar mass density of the Galactic Center becomes about 10^3 of that in the solar neighborhood. If we assume the 10^5 CVs in the Galactic Center, the number of CVs in the inner 100 pc region from the Sun was estimated to be $\sim10^2$ with the assumption of a uniform number-density per stellar mass in the Galaxy. However, only one or a few CVs have been detected from the inner 100 pc region in the hard X-ray band ([37]). When the number density of CV in the Galactic Center is roughly one hundred times as high as that in the solar neighborhood, the iron Kα-lines observed in the Galactic Center field would be explained by a superposition of 10^5 CVs.

In section 5.2, we performed the source findings. The detection-limits of the 3–10 keV band will be roughly 0.01 counts s^{-1} GIS^{-1} (see section 5.2). Assuming the spectral shape of a 10 keV thermal bremsstrahlung with $N_H = 6\times10^{22}$ H cm^{-2}, the detection-limit of 0.01 counts s^{-1} GIS^{-1} in the 3–10 keV band is equivalent to an absorption-uncorrected flux of 1×10^{-12} erg s^{-1} cm^{-2} and an absorption-corrected luminosity of 1×10^{34} erg s^{-1} at the distance of 8.5 kpc. The typical CV luminosity in the 3–10keV band is about 10^{31-32} erg s^{-1} ([37]), which is much lower than the detection-limit. The SIS field of view covers about 22 arcmin (55 pc) square degree. Therefore about 10^{3-4} CVs are included in each SIS field of view. The constant H-like/He-like flux-ratio of iron Kα-lines (figure 4.6) is explained by the averaging of the spectra of 10^{3-4} CVs. The mean separation of each CV was the order of 10 arcsec. The smooth distribution in the narrow energy-band maps of the Fe He-like Kα-line is also consistent with the superposition of the large numbers of CVs.

Type-Ia supernova progenitors are widely believed to be mass-accreting white dwarfs (including CVs), growing toward Chandrasekhar's limit. Thus the high supernova rate in the Galactic Center may be explained by the high number-density of CV.

Note that the CVs often exhibits the iron 6.4-keV line with a comparable flux of the iron Kα-lines(6.7 and 6.97 keV) from the highly ionized ions ([31] for AO Psc; [38] for AM Her; [76] for FO Aqr). Both the three Kα-lines including the 6.4-keV line, would be explained by CVs except for the extremely bright region, for example Sgr B2 (figure 4.10).

The CV spectra usually include no intense Kα-lines from helium-like ions of the silicon, sulphur, argon and calcium. The equivalent widths of Kα-lines from helium-like ions of these elements seen in the CV spectra also become smaller than those from hydrogen-like ions (cf. [22]), while those from helium-like ions seen in the Galactic Center emission become about four-times larger than those from hydrogen-like ions. Since the diffuse X-ray spectra can not be fully explained by a superposition of the CV spectra, this supports the supernova remnants scenario for Kα-lines from the lighter elements.

Using the Ginga satellite, Yamauchi et al. (1990 [108]) have already found the iron Kα-line with an elliptical shape of 1 $\times$ 1.8 deg. (FWHM) and tilting angle of about 20 deg. The mapping observation near the Galactic Center is limited within this region (chapter 4). The large-scale mapping around the Galactic Center region

is not sensitive to the tilting angle of the diffuse X-ray emission due to the limited direction of the mapping (chapter 5). Therefore we can not give further constraint on the tilting angle of the Galactic Center plasma.

As Yamauchi et al. (1990 [108]) noted, the surface brightness of normal stars shows no tilted elliptical structure ([24] and reference therein). Since the spatial distribution of CVs would be similar to that of normal stars, it would be difficult to reconcile the tilted elliptical structure with the superposition of CVs. If the iron-line distribution smoothly extends with the tilted angle of 20° outside the GC-series fields, another origin would be required. Since no other known X-ray object would be the major contributor, we further consider a hot interstellar medium (hot gas) as a main contributor of the iron Kα-lines from highly ionized ions in the overall Galactic Center plasma.

The electron density and the thermal energy of the hot gas can be estimated from the observed emission measure derived by continuum (figure 5.9). For the extended region outside Sgr A, estimations are made for a disk-shaped configuration around the Galactic center with a radius of 0°.42 and a height of 0°.19. The estimated electron density n_e and the total thermal energy of electrons are roughly 0.1 electrons cm^{-3} and 10^{53} erg. The total gas mass is 10^3 $M_\odot$.

Such a high temperature gas as observed cannot be bound by the Galactic gravity, hence the hot gas will expand. Morris (1994 [73]) reported that the magnetic field is on the order of mGauss or greater, far greater than elsewhere in the Galaxy. Then the gas expansion speed across the magnetic field would be largely reduced, while not along the field line. For simplicity, we assume the expansion speed to be the sound velocity, because detailed study require information of rather complicated magnetic field strength and configuration. With the sound speed ($\sim$1600 km s^{-1} for $kT = 10$ keV), it takes $\sim$40000 years for the hot gas to expand over 0.4 degree ($\sim$ 60 pc). This may be considered as the age of the hot gas.

The time scale of ionization equilibrium is approximately $3\times10^4 n_e^{-1}$ years, where n_e(cm^{-3}) is the density of electrons. Since the estimated age is $\sim$40000 years, the hot gas is near ionization equilibrium, which is consistent with the coincidence between the temperature derived from the continuum and that from the H-like/He-like iron-flux ratio with the assumption of ionization equilibrium. The time scale for ions and electrons to reach collisional equilibrium is approximately $3\times10^6 n_e^{-1}$ years for $kT \sim 10$ keV. The hot gas is still far from collisional equi-

librium. It is therefore possible that ions carry more than an order of magnitude larger amount of energy (i.e., higher in temperature) than electrons. Thus, the total energy of the hot gas could be as large as 10^{54} erg.

In fact, there is observational evidence that the energy of ions is much higher than that of electrons. As noticeable in figure 4.4, there exist three Kα-lines of iron, the 6.4-keV fluorescent line and the Kα-lines from helium-like ($\sim$ 6.7 keV) and hydrogen-like ions ($\sim$ 6.97 keV). While the 6.4-keV line is narrow, consistent with fluorescence of cool matter (see later section), the other two lines are both significantly broadened. The observed line width $\sigma \sim 80$ eV corresponds to a velocity dispersion of iron ions of $\sim$ 3600 km s^{-1}. Broadening of other lower-energy lines is less certain because of decreasing energy resolution. This velocity may be due mostly to bulk motion (probably expansion) of the hot gas, otherwise the temperature is extremely high ($kT \sim 3$ MeV). Indeed, it can be shown that the total energy of ions is at least an order of magnitude more than that of electrons, assuming that ions of various species are near collisional equilibrium.

The symmetric distribution of the iron helium-like Kα-line on both sides of the Galactic center favor the idea that the whole hot gas has a single origin at the Galactic center. Then, the required rate of energy generation is 10^{41-42} erg s^{-1} which is comparable to that of a low luminosity active Galactic nucleus (AGN).

Suppose an energetic outburst at the Galactic center generates a hot plasma by shock heating, the temperature of the plasma will decrease as the plasma expands. However, as discussed above, most of the energy will be carried by ions on the relevant time scale. The apparent constancy of the electron temperature observed over the whole region may be due to continuous energy supply from ions to electrons, compensating the adiabatic cooling of electrons in the course of expansion. A hot gas due to an energetic outburst at the Galactic center is another candidate of the main contributor of the iron Kα-lines from highly ionized ions.

The Bright Region around Sgr A*

We found a most bright region around Sgr A* in the narrow-band image of the iron He-like Kα-line (figure 4.9), while we found no peak around Sgr A* in that of the iron 6.4-keV line (figure 4.10). For the bright region in Sgr A, we made the spectra after subtracting the background spectrum in the surrounding region, which was

named as the soft-source spectra in chapter 6. We confirmed no significant 6.4-keV line from this spectrum. As we have already noted, the CVs often exhibits the iron 6.4-keV line with a comparable flux of the iron Kα-lines(6.7 and 6.97 keV). The iron Kα-line in this bright region would be not a superposition of CVs. We then consider a hot gas as a major contributor of the bright iron Kα-line in Sgr A.

In section 6.5, we applied the NEI plasma model to the spectrum of this bright region, which is corresponding to the soft source spectrum. The continuum and iron Kα-line were reproduced by this model, while the silicon and sulphur Kα-lines were not reproduced (figure 6.11). We infer that the non-reproduced silicon and sulphur Kα-lines may be due to supernova remnant(s). The continuum associated with the reproduced iron Kα-line is found to exhibit the high temperature about 10 keV. Note that there is no hot gas with the 10-keV continuum and the iron He-like Kα-line in the Galaxy. Also there is no candidate of a supermassive blackhole candidate in the Galaxy except for Sgr A*. Since the peak position of the bright region coincides with that of Sgr A*, this hot gas may generate at the Galactic center by recent nuclear activity. The electron density and the thermal energy of this component can be estimated from the observed emission measure (table 6.8). Assuming a spherical shape with a radius of 2 pc, the electron density, the total mass and the thermal energy of electrons are estimated to be about 5 electrons cm^{-3}, 5 $M_{\odot}$ and 2×10^{50} erg, respectively.

7.2.2 The X-ray Reflection Nebula

There are two bright regions in the 6.4-keV line (figure 4.10). The brightest lies near the prominent molecular cloud, Sgr B2. From the follow-up deep-exposure observation in the Sgr B2 region, we found that the 6.4 keV distribution shown in Plate II is shifted systematically from the radio distribution by about $2'$ to the direction of the Galactic center. The other bright region is located between Sgr A and the Radio Arc. A dense molecular cloud is recently found in this region, too ([57]; [105]). Remarkably, the equivalent width of the 6.4-keV line is as large as $\sim$1 keV at Sgr B2 (figure 4.11) only in the spectra remaining the intense thermal continuum due to the plasma in the Sgr B2 region. This large equivalent width is only expected from an X-ray illuminated neutral cloud. The 6.4-keV line is emitted as a consequence of K-shell photo-ionization of iron atoms, and at the same time

a fraction of the incident X-rays on the cloud are reflected by Thomson scattering (for numerical results of the equivalent width , see [36], also see [5] for the iron line flux). Recently, Murakami et al. (1998 [77]) applied the precise subtraction of the thermal continuum to the GIS data and found the equivalent width of the 6.4-keV line and the iron K-absorption edge (7.1 keV) to be about $\sim$3 keV and $\sim 10^{24}$ H cm^{-2}, respectively. In fact, both the large equivalent width of the 6.4-keV line and the observed continuum which is very flat and drops sharply above the iron K-absorption edge (7.1 keV) are explained very well by a model comprising the reflection, photo absorption and fluorescent iron line emission. The X-ray source(s) responsible for the 6.4-keV line should be located on the Galactic center side of the Sgr B2 cloud, because this side of the cloud is brighter in the 6.4-keV line.

The absorption-corrected flux of the 6.4-keV line near the Sgr B2 region (in the circle of $\sim 3.5'$ radius) is 1.7×10^{-4} photons cm^{-2} s^{-1}. The required incident flux on the Sgr B2 cloud for producing this line intensity is given as a function of the column density and elemental abundances of the Sgr B2 cloud.

We assume that the total mass of the Sgr B2 cloud to be 2×10^6 $M_\odot$ ([58]) with cosmic abundances of elements ([1]), and the radius to be $\sim 3.5'$ ($\sim$ 7 pc). Then the column density of the Sgr B2 cloud is estimated to be 4×10^{23} H cm^{-2}. The required incident flux also depends weakly on the spectrum of the incident X-rays. We thus assume the spectrum to be a power-law of a photon index of 1.7, typical values for AGN and Galactic X-ray binaries.

One possible source is the existing Galactic Center plasma. However, the integrated X-ray flux is found to be far insufficient, by more than a factor of ten, to account for the observed 6.4-keV line intensity. Another possibility is nearby bright discrete sources. In fact, a X-ray binary candidate, 1E 1743.1$-$2843, lies only about 0.4 degrees from Sgr B2. During the present observation, its luminosity was $\sim 2 \times 10^{36}$ erg s^{-1} after correction for the measured absorption ([61]). Whereas, the time-averaged luminosity required to account for the observed 6.4-keV line is $\sim 10^{38}$ erg s^{-1} which is near the Eddington limit of an accreting neutron star. The other bright region in the 6.4-keV line near the Radio Arc also requires equally luminous X-ray source(s) in its neighborhood. In view of small duty ratios of bright transients, this possibility is rather unlikely.

A more straightforward idea would be that the incident X-rays on these molecular clouds come from a single origin. The most probable site is the Galactic

Center. For a source at the Galactic center, the luminosity required to account for the 6.4-keV line from Sgr B2 is 2×10^{39} erg s^{-1}, which exceeds those of the brightest X-ray binaries by a large factor.

Since the present X-ray luminosity of Sgr A*, is much less than 10^{36} erg s^{-1} (for detail, see section 7.3), we can consider two possibilities;

- The nuclear source is obscured by a high column of gas.
- The nuclear source was $\sim 10^4$ times more luminous ~300 years ago, the light travel time for 90 pc to Sgr B2, than it is today.

The first one is essentially the same as considered for Seyfert 2 galaxies in the unified scheme of AGNs. From the radio spectrum of Sgr A*, Beckert et al. (1996 [7]) reported that the local column density of Sgr A* is not larger than 2×10^{22} cm^{-2}. This value is far too small to obscure the source. Together with the absence of any bright IR source at Sgr A*, the hidden AGN scenario is excluded.

The second possibility considers a scenario that the Galactic center exhibited intermittent activities in the past. In fact, as noted in chapter 4, the region around Sgr A* is markedly brighter than the surrounding region, which suggests that it is due to a more recent nuclear activity. It is also possible that the observed 6.4-keV line emission is produced by X-rays from the Sgr A region. While the Sgr A region has an X-ray luminosity of $\sim 3 \times 10^{35}$ erg s^{-1} at present, it could have been much more luminous $\sim$ 300 years ago. If we assume, for simplicity, that the total gas mass remains constant during expansion, the X-ray luminosity scales as l^{-3}, where l is the linear size of the hot gas. Hence, when it was ~1/10 the present size, the luminosity could be as high as 10^{39} erg s^{-1}.

Phinney (1989 [84]) reported that, if there is a black hole with mass of $10^6 M_\odot$, this would be activated by a tidally capture of stars. The mean time between captures is probably 10^4 - 10^5 year. Therefore, it is conceivable that our predicted most recent activity about 300 years ago is due to the last tidal capture of a star.

It is to be noted that no other giant molecular clouds are bright in the 6.4-keV line. For instance, Sgr C (on the other side of the center) is at a similar distance from the center to Sgr B2 but is not distinctly bright in the 6.4 keV line. It may imply that the X-ray beam from the center is not isotropic, due possibly to blocking by dust at some directions.

The 6.4 keV line extending more broadly in latitude than the molecular cloud layer, but with much reduced brightness level. We suggest this weak 6.4 keV line would not be from molecular clouds but would be from thin cool (less than 10^5 K) gas prevailing more broadly across the plane and/or the superposition of CVs.

7.3 Present Activities of the Galactic Center Sgr A*

Another piece of important information, possibly related to the nuclear activity, is obtained from the monitoring observations of the Sgr A plasma.

Many X-ray observations near to the Galactic center Sgr A* have been carried out. To compare them with our Galactic center observations, we applied a simple assumption that Sgr A* has a 10 keV thermal bremsstrahlung with $N_{\rm H} = 1\times10^{23}$ cm^{-2} (see section 6.5.4), and converted the reported X-ray fluxes into the 3–10 keV band fluxes. The Spacelab-2 observations in 1985 July–August gave a 3–10 keV flux 3×10^{-11} erg s^{-1} cm^{-2} ([94]). The SPARTAN observation, made about 6 weeks earlier than the Spacelab-2 mission, detected no significant flux with an upper limit of 1×10^{-11} erg s^{-1} cm^{-2} ([45]). In 1990 March and April, Syunyaev et al. (1991 [100]) reported a source within $1'$ of the nucleus, whose 3–10 keV fluxes corresponds to 10×10^{-11} erg s^{-1} cm^{-2} and 16×10^{-11} erg s^{-1} cm^{-2}, respectively. In 1991 September–October, the emission from this region was at the same level in the 3–10 keV band. Therefore, the previous observations suggested a long-term time variability of Sgr A* with the 3–10 keV flux ranging (1–16) $\times10^{-11}$ erg s^{-1} cm^{-2}. On the other hand, with *ASCA*, we found that the bright region around Sgr A* (soft source) exhibited no significant time variability during the three observations at a flux level less than 2×10^{-11} erg s^{-1} cm^{-2} (see section 6.5.4).

Since two variable hard X-ray sources (A 1742−289 and AX J1745.6−2901) are in a close vicinity of Sgr A*(only $\sim 1'.5$), we are cautious that the previous non-imaging observations of Sgr A*, if not all, might have been contaminated by these sources. Then, the repeated *ASCA* monitoring observations should be a first research for the hard X-ray activity of Sgr A* itself with less contamination. Therefore we discuss the present X-ray activity of Sgr A* by comparing to the active Galactic nuclei(AGNs).

As is given in figure 6.2, the peak position of the soft source coincided with the Galactic center Sgr A* and exhibited a diffuse structure. We can estimate the upper limit of the X-ray flux $F_{\rm x,SgrA*}$ of Sgr A* to be the X-ray flux of the soft source, i.e.

$$F_{\rm x,SgrA*} < 2 \times 10^{-11} \text{erg s}^{-1} \text{ cm}^{-2} \ (2 - 10\text{keV}). \tag{7.1}$$

The X-ray luminosity $L_{\rm x,SgrA*}$ at the distance of 8.5 kpc corrected with the interstellar absorption of $8{\times}10^{22}$ H cm^{-2} (table 6.8) is given by

$$L_{\rm x,SgrA*} \lesssim 10^{35} \text{erg s}^{-1} \text{ cm}^{-2} \ (2 - 10\text{keV}). \tag{7.2}$$

One of the most important discoveries of the early days of X-ray astrophysics was that X-rays are commonly found from AGNs and that a large fraction of radiation-energy from AGNs is radiated in the X-ray band ([20]), whose X-ray luminosities largely exceed the Eddington luminosity 10^{38} erg s^{-1} of a stellar-mass ($\sim$1 $M_\odot$) black hole. For example, the Seyfert galaxy, which is famous for AGN, exhibits the X-ray luminosity of 10^{41-43} erg s^{-1}. The upper limit of the X-ray luminosity from Sgr A* is much less than the Eddington luminosity 10^{38} erg s^{-1} of a stellar-mass ($\sim$ 1 $M_\odot$) black hole. We confirmed that the present activity of Sgr A* is much quieter than that of AGNs.

As is discussed in 6.5.4, we also detected no flux variations larger than its flux-level ($2{\times}10^{-11}$ erg s^{-1} cm^{-2}) from the soft source with various time scale. Therefore, we found no flux variability with the various time scale from Sgr A*. On the contrary, the *Ariel 5* sky survey made clear that significant fraction of the Seyfert 1 showed a large amplitude ($\delta I/I > 1$) variability on time scales of days ([66]). Recent reanalysis of the EXOSAT results ([26]) revealed that $\sim$ 40% of AGN in a hard X-ray selected sample, show variability on a time scale of less than one day. On longer time scale (typically weeks to months) 97% of the same sample showed significant variability. Since we found neither luminous X-rays nor X-ray flux-variability from Sgr A*, we did not found any direct evidence for the similarity between Sgr A* and AGNs. While we suggested that the Galactic center exhibited past intermittent activities in section 7.2.2, we can conclude that Sgr A* is quiescent, at least, during the past several years.

7.4 The Galactic Ridge Emission

We also detected the Galactic ridge emission extending up to 10 degree from the Galactic Center with GIS (chapter 5). The ridge emission along the Galactic plane (hereafter "the on-plane emission") have been already discussed in detail by Kaneda (1997 [43]). We then discuss mainly about the ridge emission perpendicular to the Galactic plane (hereafter "the off-plane emission") where the GB-series fields are included.

The equivalent widths of He-like Kα-lines of the silicon, sulphur, argon, calcium and iron of the on-plane emission are confirmed to be roughly constant (figure 5.12). The correlation of the flux-ratio of the silicon to the sulphur He-like Kα-line normalized by the iron, implies that the emissivity-ratio of the silicon to the sulphur Kα-line normalized by that of the iron Kα-line is roughly constant for the on-plane emission. Although the luminosity varies from field to field, we straightforwardly interpret that the emissivity ratios among the Kα-lines of the silicon, sulphur and iron are roughly uniform on the Galactic plane.

On the contrary to the on-plane emission, the equivalent widths of the sulphur and argon Kα-lines in the off-plane field ($|b| > 2^\circ$) show the smaller values than the equivalent width in the Galactic Center and on-plane (figure 5.12), while that of the silicon Kα-line is roughly constant in all the fields.

Since the on-plane emission has a scale height of about 100 pc ([109];[43]), the off-plane emission is inferred to include the on-plane emission integrated along the line of sight. The small equivalent widths of the sulphur and argon Kα-lines in the off-plane field imply that the off-plane emission is not explained only by the integrated on-plane emission. Then we consider one more component: a thin thermal plasma with a high emissivity of the Si He-like Kα-line in the Galactic bulge region (hereafter "the Galactic bulge emission"), which extends around the Galactic Center with a larger scale height than that of the on-plane emission (figure 7.2).

The silicon helium-like Kα-line shows the highest emissivity at the temperature kT of about 0.9 keV assuming an ionization-equilibrium in this plasma ([68]). Therefore we consider the thin thermal plasma with the temperature of 0.9 keV in the Galactic bulge. The volume emissivity ε (photons s^{-1} cm^{-3} keV^{-1}) for the thermal bremsstrahlung from a plasma with a temperature kT is roughly written

by,

$$\varepsilon \propto E^{-1} \exp(-E/kT) \tag{7.3}$$

with the photon energy E. In the off-plane field, the on-plane emission including the silicon, sulphur, argon, calcium and iron Kα-lines largely decreases its flux, while the bulge emission mainly including the silicon Kα-line shows less decrease because of the different scale heights. Then the equivalent widths of the low energy Kα-lines of sulphur and argon become small by the continuum emission of the bulge emission, while the equivalent width of the iron Kα-line is not largely affected by this continuum emission because the energy (6.7 keV) of the iron Kα-line is much higher than 0.9 keV. The superposition of the on-plane and bulge emission is consistent with the observed equivalent widths.

We plotted the correlations of the flux-ratio of the silicon to the sulphur He-like Kα-line normalized by the iron in figures 5.14 & 5.15. When the Galactic bulge emission has a high emissivity of the silicon Kα-line, the correlation in the off-plane field would shift to the direction of the upper left. This shift is seen in figures 5.14 & 5.15. We then conclude that the off-plane emission has two components: the on-plane and bulge emission.

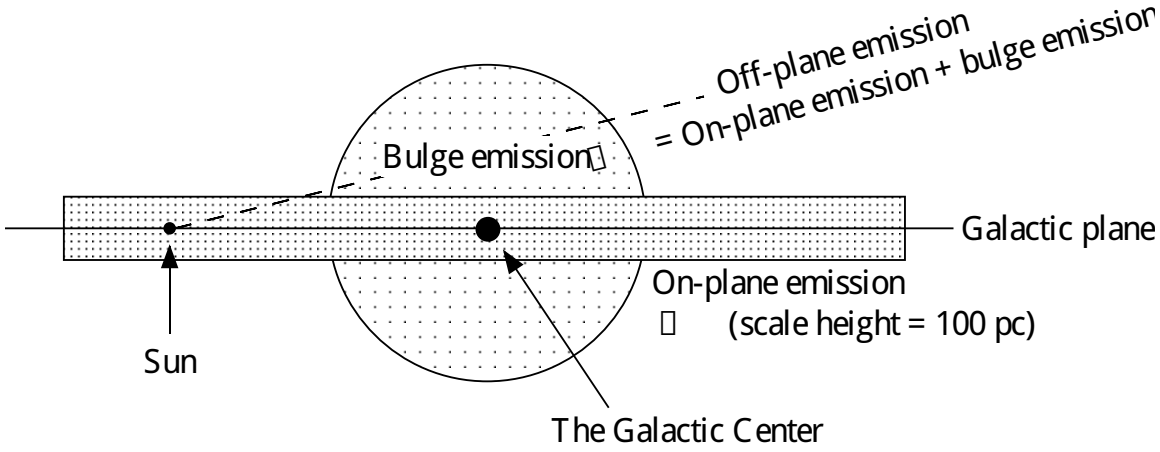

Figure 7.2: A schematical view to show a relation among the on-plane, off-plane and bulge emission.

7.4.1 Origin of the Galactic Bulge Emission

Snowden et al. (1997 [96]) detected the diffuse soft X-ray emission from the Galactic bulge with the radial extent of $\sim$5.6 kpc. The X-ray emission has a scale height of 1.9 kpc, where the typical temperature is estimated to be $\sim$0.34 keV using the soft X-ray color. We detected the diffuse Galactic bulge emission with the higher scale height of $\gg$ 100 pc. Therefore the Galactic bulge emission corresponds to the the diffuse soft X-ray emission from the Galactic bulge. We detected the highly ionized silicon Kα-line from the Galactic bulge emission. This gives firm evidence for the presence of thin thermal hot gas in the Galactic bulge.

In section 7.2.1, we can suggest the possibility of the presence of the hot gas with the temperature of $\sim$10 keV. As pointed out in Yamauchi and Koyama (1993 [109]), the temperature of 10 keV is higher than that bounded by the Galactic gravity. Although the magnetic field is on the order of mGauss or greater, Morris (1994 [73]) suggested that the direction of the magnetic field is perpendicular to the Galactic plane in the inner 100 pc from the Galactic center. Therefore the hot gas in the Galactic Center may escape perpendicular to the Galactic plane and arrive at the Galactic bulge region. This would be one possibility for the origin of the Galactic bulge emission, although further quantative examination is needed.

Appendix A

SIS Background Spectrum for the Diffuse X-ray Emission

The raw diffuse X-ray spectra includes the SIS backgrounds, which consist of the internal and the cosmic X-ray components. In our analysis performed in chapter 4, we separately subtracted these two components. The "night-earth" data are believed to represent the internal background(here after IBG) due to the cosmic particles. Dr. K. Gendreau kindly supplied us the "night-earth" data taken by chip-1 of SIS0(so called S0C1). Since we assumed that the IBG of each chip is the same, we applied this night-earth spectrum to each chip.

Observed spectra also included the cosmic X-ray background, so called CXB, which is believed to originate from the extragalactic object. The CXB is expected to be absorbed in the Galaxy before reaching the Sun. The absorption to the direction of the Galactic Center exhibits the typical absorption column of $\sim 10^{23}$ H cm^{-2}(optical depth $\tau = 1$ at 3–4 keV) (cf. [91]). Therefore the low energy part of CXB varies from field to field due to the Galactic absorption. We estimated the simple model reproducing the CXB spectrum of SIS using the high-latitude observations. The used high-latitude spectrum was a superposition of 3 high-latitude fields without any obvious sources and with a total exposure of about 120 ks, which was released by GSFC/NASA. We show the raw high-latitude spectrum including the internal background in figure A.1.

After subtracting the above intrinsic background, the high-latitude spectrum was found to be approximated by a thermal bremsstrahlung with the temperature of 14 keV. In our spectral fitting, we reproduced the CXB component using this

thermal-bremsstrahlung model modified with a variable Galactic absorption. We set the variable Galactic absorption to the same value of the absorption column to the Galactic diffuse emission.

We simultaneously show the averaged diffuse X-ray spectrum observed in the Galactic Center region in figure A.1, which is also includes both the intrinsic and cosmic X-ray backgrounds. As is shown in figure A.1, the count rate in the $\sim$2–7 keV band obtained in the Galactic Center region is about 10 times brighter than that in the high-latitude observation. Consequently, our results of the spectral analysis have little dependence of the uncertainty of the background subtraction.

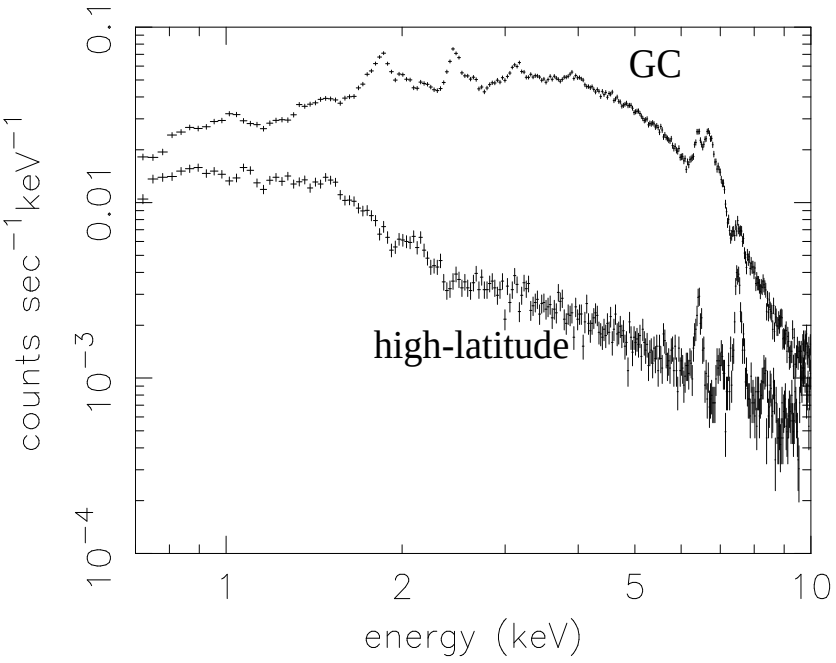

Figure A.1: The SIS spectrum of the high-latitude observation, which includes the intrinsic background. For comparison, we simultaneously plot the averaged SIS spectrum observed in the Galactic Center("GC") region, which includes both the intrinsic and cosmic X-ray backgrounds. Error bars are 1σ level.

Appendix B

GIS Background Spectrum for the Diffuse X-ray Emission

The GIS background consists of the non-X-ray and the cosmic X-ray components. In our analysis, we separately subtracted these two backgrounds. In figure B.1, we show the "night-earth" spectrum. The "night-earth" data are believed to represent the non-X-ray background(hereafter NXB) due to the cosmic particles. Therefore, we used the "night-earth" data for the non-X-ray background. Ishisaki et al.([40]) analyzed the night-earth data observed from June 1993 to June 1995, which amount to 1,400 ks. They found the long-term increase of NXB. They also found that the flux of NXB is normalized by,

$$\text{norm. factor} = 0.9983 + 2.1255 \times 10^{-9} \times (\text{ASCATIME} - 45878400), \quad \text{(B.1)}$$

where ASCATIME represents the time in second from 00 : 00 : 00(UT) on 1 January 1993. We used the night-earth data taken from May 28 1993 to Feb 8 1994, which were created by Drs. Ishisaki & Ebisawa and supplied by GSFC/NASA. We applied the background-subtraction normalized with equation B.1. They([40]) also researched the reproducibility of NXB where they used the data in the 0.7–7 keV energy band within radius of $\sim$ 20 arcmin from the optical axis. They found the reproducibility for the NXB data(10–40 ksec integration) to be $\sim$ 15% error(rms) for the NXB rejection of COR $<$ 6 GeV c^{-1}, which is the same criteria of our data screening. Therefore we applied the 15% systematic error(1 σ) to the NXB data used for background-subtraction.

Observed spectra also included the cosmic X-ray background(CXB). The CXB is expected to be absorbed in the Galaxy before reaching the Sun. The absorption

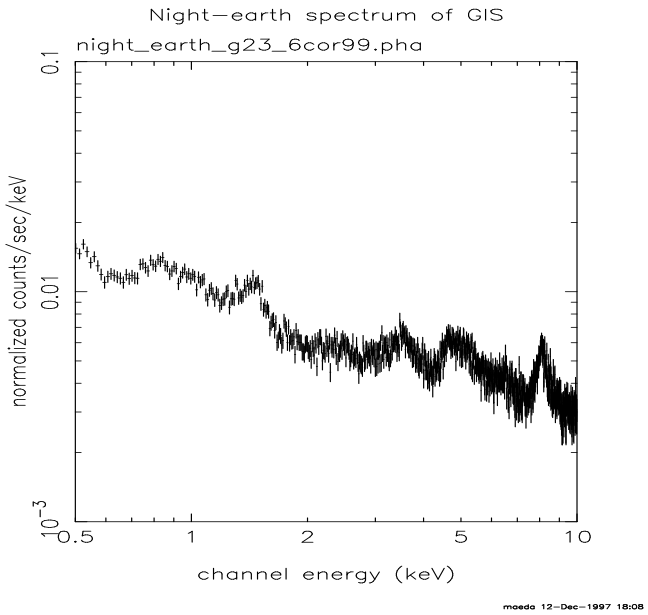

Figure B.1: The night-earth spectrum of GIS taken from the circular region of $17'.5$ radii.

to the direction of the Galactic Center exhibits the typical absorption column of $\sim 10^{23}$ H cm^{-2}(optical depth $\tau = 1$ at 3–4 keV) ([91]). On the contrary, the absorption to the direction of the Galactic bulge, which is several degrees away from the Galactic plane, exhibits the smaller value of $\leq 10^{22}$ H cm^{-2}($\tau = 1$ at $<$1–2 keV). Therefore the CXB varies from field to field due to the Galactic absorption.

We estimated the simple model reproducing the CXB spectrum of GIS using the high-latitude observations, which have the small Galactic absorption column of $\leq 10^{21}$ H cm^{-2}(cf. [39], [35]). The used CXB spectrum was a superposition of 15 blank sky fields observed during the *ASCA* early phase (May 93 – Mar 94), which was released by GSFC/NASA. The CXB spectrum was approximated by a power-low model with the photon index $\Gamma = 1.48$. In our spectral fitting, we reproduced the CXB component using this power-law model modified with a variable Galactic absorption. For each field, we set the variable Galactic absorption to the same value of the absorption to the Galactic diffuse emission unless otherwise mentioned. Consequently, the systematic error of NXB was included in our spectral analysis, while the systematic error of CXB was not included. Note that, generally speaking, the NXB and CXB dominate below and above $\sim$5 keV, respectively.

Appendix C

K-lines Obtained by GIS

Table C.1: Best-fit parameters of the iron-broad-line model for the GIS spectra

Field	Field center		——— The iron K-line ———				
	l_{II}[a]	b_{II}[a]	Line energy[b]	Line width[c]	SB[d]	EW[e]	χ^2/d.o.f
GC0	−0.013	0.004	6.57±0.01	191±21	38.1±1.87	924±50	102.2/64
GC1	0.330	0.217	6.60±0.04	238±51	8.46±0.95	838±105	63.92/64
GC2	0.514	−0.082	6.53±0.02	213±26	19.9±1.24	1240±91	84.79/64
GC3	0.170	−0.293	6.60±0.02	223±32	14.3±1.08	856±71	102.3/64
GC4	−0.169	−0.499	6.65±0.05	203±65	6.24±0.95	639±105	69.49/64
GC5	−0.265	−0.147	6.64±0.02	155±31	18.5±1.21	736±52	88.66/64
GC6	−0.534	0.094	6.57±0.03	159±40	10.7±0.96	697±68	69.23/64
GC7	−0.193	0.308	6.61±0.04	240±51	7.79±0.87	885±111	70.14/64
GP−2	−1.810	−0.080	6.63±0.08	193±107	2.46±0.61	636±172	78.18/64
GP−3	−2.310	−0.076	6.66±0.08	216±113	2.13±0.50	867±225	57.72/64
GP−4	−2.813	−0.075	6.68±0.10	209±170	1.78±0.53	802±264	69.70/64
GP−5	−3.304	0.007	6.61±0.08	0(<232)	1.81±0.54	890±294	62.02/64
GP−6	−3.805	0.006	6.70±0.07	0(<273)	1.40±0.36	722±201	67.25/64
GP−7	−4.305	0.006	6.69±0.09	165(<330)	1.68±0.51	834±279	73.96/64
GP−8	−4.803	0.007	6.76±0.08	0(<186)	1.71±0.49	320±95	81.80/64
GP−12	−6.805	0.006	6.64±0.12	193(<463)	1.45±0.64	448±212	54.37/64
GP−13	−7.307	0.006	6.62±0.10	225±153	1.63±0.49	1053±356	61.97/64
GP−14	−7.802	0.008	6.61±0.10	194(<388)	1.61±0.56	984±389	76.21/64
GP+1	0.998	0.003	6.60±0.06	240±79	7.38±1.16	840±145	91.74/64
GP+2	1.495	0.009	6.63±0.05	60(<193)	2.97±0.65	446±100	59.96/64
GP+6	3.495	0.007	6.54±0.08	201±118	1.94±0.50	1206±356	78.66/64
GP+7	3.994	0.010	6.66±0.07	107(<232)	1.42±0.39	990±293	42.89/64
GB−1	0.006	−0.841	6.57±0.04	129(<258)	3.02±0.46	434±69	56.36/64
GB−2	0.005	−1.258	6.64±0.07	184±120	1.54±0.35	491±117	56.37/64
GB−3	0.007	−1.674	6.71±0.06	140(< 280)	1.23±0.27	954±225	61.76/64
GB−4	−0.007	−2.070	6.58±0.08	309±128	1.40±0.30	1250±298	66.23/64
GB−5	−0.006	−2.486	6.65±0.07	188(<376)	1.23±0.28	1144±288	53.93/64
GB−6	−0.004	−2.898	6.56±0.11	163(<392)	0.56±0.26	552±280	65.74/64
GB−7	−0.010	−4.990	6.60(fix)	200(fix)	0.32±0.15	1754±905	45.09/66
GB−8	−0.006	−6.989	6.60(fix)	200(fix)	0.09(< 0.24)	1001(<2680)	46.93/66
GB−9	0.007	−9.006	6.60(fix)	200(fix)	0.05(<0.19)	1302(<5568)	47.07/66

All the errors are single-parameter 90% confidence limits.

a : (degree).

b : (keV).

c : (eV).

d : Surface brightness (photon s^{-1} cm^{-2} sr^{-1}).

e : Equivalent width (eV).

Table C.2: Best-fit parameters of the double iron-line model for the GIS spectra

Field	Field center		– The 6.4-keV line –		– The 6.7-keV line –	
	l_{II}[a]	b_{II}[a]	SB[b]	EW[c]	SB[b]	EW[c]
GC0	−0.013	0.004	15.8±1.6	362±37	20.2±1.6	492±41
GC1	0.330	0.217	2.76±0.72	254±68	4.57±0.77	450±78
GC2	0.514	−0.082	10.8±1.0	633±64	7.39±1.02	450±65
GC3	0.170	−0.293	5.03±0.87	278±49	7.74±0.91	457±56
GC4	−0.169	−0.499	1.54±0.75	148±73	4.04±0.81	413±84
GC5	−0.265	−0.147	4.63±1.00	173±38	13.2±1.10	524±45
GC6	−0.534	0.094	4.92±0.82	310±53	5.73±0.85	379±58
GC7	−0.193	0.308	2.47±0.67	256±71	4.19±0.70	461±80
GP−2	−1.810	−0.080	0.68±0.49	161±119	1.54±0.52	399±137
GP−3	−2.310	−0.076	0.45±0.37	164±136	1.34±0.40	533±163
GP−4	−2.813	−0.075	0.32±0.41	130±169	1.17±0.45	514±201
GP−5	−3.304	0.007	0.51(< 1.0)	240(<510)	1.39±0.60	719±329
GP−6	−3.805	0.006	0.18(<0.56)	85(<269)	1.30±0.43	682±233
GP−7	−4.305	0.006	0.20(<0.60)	91(<272)	1.30±0.44	635±225
GP−8	−4.803	0.007	0.00(<0.45)	0(<71)	1.63±0.48	295±90
GP−12	−6.805	0.006	0.37(< 0.80)	102(<223)	0.93±0.45	288±142
GP−13	−7.307	0.006	0.54±0.37	309±220	0.85±0.38	538±251
GP−14	−7.802	0.008	0.51±0.38	279±217	0.95±0.41	584±258
GP+1	0.998	0.003	2.34±0.86	243±91	3.96±0.91	448±105
GP+2	1.495	0.009	0.83±0.57	112±78	2.36±0.60	371±96
GP+6	3.495	0.007	0.93±0.42	537±251	0.85±0.43	542±284
GP+7	3.994	0.010	0.27(<0.62)	168(<385)	1.16±0.38	827±279
GB−1	0.006	−0.841	1.31±0.39	179±54	1.77±0.40	266±61
GB−2	0.005	−1.258	0.37±0.28	105±80	1.02±0.29	330±95
GB−3	0.007	−1.674	0.12(<0.35)	82(<237)	1.00±0.25	758±198
GB−4	−0.007	−2.070	0.42±0.20	317±153	0.61±0.21	518±178
GB−5	−0.006	−2.486	0.25±0.22	200±178	0.84±0.24	769±222
GB−6	−0.004	−2.898	0.25±0.21	234±201	0.29±0.22	307±231
GB−7	−0.010	−4.990	0.09(<0.21)	420(<1138)	0.18±0.16	1061±956
GB−8[d]	−0.006	−6.989	0.06(<0.12)	548(<1081)	0.05(<0.13)	747(<1595)
GB−9[d]	0.007	−9.006	0.05(<0.11)	1281(<3132)	0.03(<0.12)	992(<4055)

Due to the limited energy resolution, we fixed to the line energy to 6.4 keV and 6.7 keV, respectively. Both line widths were fixed to zero. All the errors are single-parameter 90% confidence limits. The electron temperature (kT), normalization, absorption column ($N_{\rm H}$) are separately shown in table C.3.

a : (degree).

b : Surface brightness (photon s^{-1} cm^{-2} sr^{-1}).

c : Equivalent width (eV).

d : We did not detect any significant iron line. We separately decided the upper limits of the two iron lines with a model of one Gaussian line and an absorbed thermal bremsstrahlung to the data in 3.5–9 keV band. The best-fit kT, $N_{\rm H}$ and χ^2 values were decided in the fitting for the 6.4-keV line.

Table C.3: (Continued)

Field	Field center		Continuum			
	l_{II}	b_{II}	kT^a	Norm.^{b}	$N_H{}^c$	χ^2/d.o.f
GC0	−0.013	0.004	$20.6^{+7.3}_{-4.8}$	$2.4^{+0.2}_{-0.1}$	4.4±0.9	106.9/65
GC1	0.330	0.217	$20.7^{+21.3}_{-8.3}$	$0.58^{+0.08}_{-0.05}$	$3.2^{+1.8}_{-1.6}$	69.00/65
GC2	0.514	−0.082	$23.5^{+20.2}_{-8.3}$	$0.99^{+0.12}_{-0.06}$	$7.6^{+1.5}_{-1.4}$	88.52/65
GC3	0.170	−0.293	$19.6^{+10.8}_{-5.7}$	$0.96^{+0.08}_{-0.07}$	$3.2^{+1.2}_{-1.2}$	111.0/65
GC4	−0.169	−0.499	54.3(>22.1)	$0.52^{+0.16}_{-0.04}$	$0.7^{+1.7}_{-0.7}$	71.57/65
GC5	−0.265	−0.147	$21.8^{+9.9}_{-5.7}$	$1.44^{+0.12}_{-0.08}$	$4.3^{+1.0}_{-1.0}$	88.72/65
GC6	−0.534	0.094	114^{+86}_{-75}	$0.99^{+0.17}_{-0.13}$	$4.6^{+1.4}_{-1.0}$	68.88/65
GC7	−0.193	0.308	44.6(>20.6)	$0.48^{+0.14}_{-0.03}$	$1.7^{+1.7}_{-1.5}$	77.79/65
GP−2	−1.810	−0.080	$9.4^{+13.2}_{-3.7}$	$0.28^{+0.13}_{-0.07}$	$3.9^{+2.9}_{-2.8}$	78.56/65
GP−3	−2.310	−0.076	$10.3^{+19.7}_{-4.7}$	$0.16^{+0.10}_{-0.03}$	$1.6^{+3.0}_{-1.6}$	59.36/65
GP−4	−2.813	−0.075	$10.0^{+35.8}_{-5.1}$	$0.15^{+0.13}_{-0.04}$	$2.2^{+3.9}_{-2.2}$	70.42/65
GP−5	−3.304	0.007	$11.5^{+25.8}_{-7.3}$	$0.12^{+0.16}_{-0.01}$	0.0(<5.4)	63.23/65
GP−6	−3.805	0.006	$6.6^{+14.8}_{-3.0}$	$0.17^{+0.20}_{-0.07}$	3.5(<8.0)	66.69/65
GP−7	−4.305	0.006	$9.0^{+6.9}_{-3.4}$	$0.14^{+0.06}_{-0.02}$	0.0(<2.1)	74.26/65
GP−8	−4.803	0.007	$3.3^{+0.7}_{-0.5}$	$1.3^{+0.6}_{-0.4}$	$6.7^{+2.3}_{-2.2}$	83.70/65
GP−12	−6.805	0.006	$4.7^{+2.4}_{-1.3}$	$0.43^{+0.29}_{-0.16}$	$5.0^{+3.1}_{-3.0}$	54.76/65
GP−13	−7.307	0.006	$8.7^{+11.8}_{-4.8}$	$0.11^{+0.14}_{-0.02}$	0.5(<4.7)	63.24/65
GP−14	−7.802	0.008	$5.2^{+9.6}_{-2.3}$	$0.20^{+0.31}_{-0.10}$	$7.2^{+5.3}_{-4.7}$	76.86/65
GP+1	0.998	0.003	$8.9^{+5.5}_{-2.4}$	$0.65^{+0.20}_{-0.13}$	$3.7^{+2.1}_{-2.1}$	94.95/65
GP+2	1.495	0.009	$3.1^{+0.6}_{-0.4}$	$1.8^{+0.7}_{-0.5}$	$6.8^{+2.0}_{-1.9}$	59.38/65
GP+6	3.495	0.007	$6.0^{+8.9}_{-2.9}$	$0.15^{+0.23}_{-0.05}$	1.8(<6.9)	78.98/65
GP+7	3.994	0.010	$3.1^{+2.3}_{-1.0}$	$0.36^{+0.58}_{-0.20}$	$5.1^{+5.0}_{-4.5}$	42.45/65
GB−1	0.006	−0.841	$7.7^{+2.3}_{-1.5}$	$0.53^{+0.11}_{-0.08}$	$3.3^{+1.4}_{-1.3}$	57.18/65
GB−2	0.005	−1.258	$4.1^{+1.2}_{-0.8}$	$0.48^{+0.19}_{-0.13}$	$3.9^{+2.0}_{-2.0}$	56.82/65
GB−3	0.007	−1.674	$4.6^{+1.1}_{-1.3}$	$0.16^{+0.10}_{-0.02}$	0.0(<2.5)	62.77/65
GB−4	−0.007	−2.070	$6.5^{+2.3}_{-1.9}$	$0.10^{+0.04}_{-0.01}$	0.0(<1.7)	69.01/65
GB−5	−0.006	−2.486	$4.5^{+4.5}_{-1.7}$	$0.15^{+0.20}_{-0.07}$	2.9(<7.1)	53.62/65
GB−6	−0.004	−2.898	$5.2^{+8.5}_{-2.3}$	$0.11^{+0.17}_{-0.05}$	2.5(<7.1)	65.63/65
GB−7	−0.010	−4.990	$1.6^{+2.6}_{-0.6}$	$0.35^{+3.00}_{-0.33}$	8.5(<19.5)	45.21/65
GB−8	−0.006	−6.989	$0.89^{+0.51}_{-0.24}$	$5.2^{+78.0}_{-5.0}$	21±15	47.07/66
GB−9	0.007	−9.006	$1.6^{+27.3}_{-1.2}$	$0.054^{+1.149}_{-0.051}$	1.3(<12.5)	46.83/66

a : (keV).

b : ($3.02 \times 10^{-15} \int n_e n_i dV$ / ($4\pi D^2$), where n_e is the electron density (cm^{-3}), n_i is the ion density (cm^{-3}), and D is the distance to the source (cm). $n_e = 1.08 \times n_i$.).

c : (10^{22} H cm^{-2})

Table C.4: Summary of the K-lines in the 1.15–4.5 keV band of the GIS spectra

Field	Field center		Line energy(keV)				
	$l_{II}{}^a$	$b_{II}{}^a$	Mg	Si	S	Ar	Ca
GC0	−0.013	0.004	1.28±0.03	1.81±0.01	2.39±0.01	3.02±0.03	3.79±0.06
GC1	0.330	0.217	1.29±0.08	1.81±0.01	2.39±0.02	3.11±0.08	3.68±0.11
GC2	0.514	−0.082	1.35±0.02	1.73±0.02	2.38±0.05	3.14(fix)	3.90(fix)
GC3	0.170	−0.293	1.25±0.03	1.81±0.02	2.41±0.01	3.06±0.03	3.83±0.07
GC4	−0.169	−0.499	1.35(fix)	1.81±0.04	2.45±0.04	3.01±0.17	3.90(fix)
GC5	−0.265	−0.147	1.25±0.04	1.80±0.02	2.40±0.02	3.06±0.08	3.79±0.13
GC6	−0.534	0.094	1.31±0.03	1.81±0.04	2.41±0.05	3.14(fix)	3.90(fix)
GC7	−0.193	0.308	1.24±0.04	1.82±0.02	2.45±0.04	3.27±0.21	3.90(fix)
GP−2	−1.810	−0.080	1.27±0.04	1.78±0.03	2.44±0.06	3.13±0.07	3.85±0.26
GP−3	−2.310	−0.076	1.22±0.06	1.79±0.05	2.40±0.05	2.98±0.16	3.96±0.14
GP−4	−2.813	−0.075	1.35(fix)	1.86±0.08	2.51±0.18	3.14±0.19	3.90(fix)
GP−5	−3.304	0.007	1.35(fix)	1.86±0.07	2.48±0.08	3.36±0.38	3.90(fix)
GP−6	−3.805	0.006	1.35(fix)	1.83±0.04	2.37±0.05	3.04±0.08	3.90(fix)
GP−7	−4.305	0.006	1.24±0.06	1.82±0.04	2.49±0.06	3.02±0.10	3.90(fix)
GP−8	−4.803	0.007	1.19±0.12	1.97±0.06	2.42±0.05	3.01±0.12	3.98±0.12
GP−12	−6.805	0.006	1.35(fix)	1.86±0.06	2.45(fix)	3.14(fix)	3.90(fix)
GP−13	−7.307	0.006	1.31±0.05	1.85±0.03	2.38±0.05	3.14(fix)	3.90(fix)
GP−14	−7.802	0.008	1.31±0.04	1.81±0.07	2.45(fix)	3.09±0.24	3.90(fix)
GP+1	0.998	0.003	1.35(fix)	1.73±0.07	2.45(fix)	3.14(fix)	3.90(fix)
GP+2	1.495	0.009	1.35(fix)	1.74±0.04	2.45(fix)	3.21±0.09	3.90(fix)
GP+6	3.495	0.007	1.35(fix)	1.69±0.05	2.45±0.05	3.16±0.23	3.90(fix)
GP+7	3.994	0.010	1.35(fix)	1.82±0.07	2.38±0.07	3.23±0.17	3.95±0.15
GB−1	0.006	−0.841	1.24±0.04	1.83±0.01	2.42±0.02	3.01±0.08	3.90(fix)
GB−2	0.005	−1.258	1.30±0.02	1.85±0.01	2.43±0.03	3.14(fix)	3.90(fix)
GB−3	0.007	−1.674	1.30±0.02	1.83±0.01	2.43±0.05	3.14(fix)	3.90(fix)
GB−4	−0.007	−2.070	1.28±0.02	1.82±0.02	2.42±0.08	3.14(fix)	3.90(fix)
GB−5	−0.006	−2.486	1.27±0.02	1.82±0.02	2.38±0.11	3.14(fix)	3.90(fix)
GB−6	−0.004	−2.898	1.30±0.04	1.83±0.04	2.47±0.13	3.05±0.11	3.90(fix)
GB−7	−0.010	−4.990	1.27±0.03	1.84±0.04	2.45(fix)	3.14(fix)	3.90(fix)
GB−8	−0.006	−6.989	1.30±0.03	1.84±0.04	2.47±0.09	3.14(fix)	3.90(fix)
GB−9	0.007	−9.006	1.35(fix)	1.87(fix)	2.45(fix)	3.14(fix)	3.90(fix)

All the line widths are fixed to zero. All the errors are single-parameter 90% confidence limits. The surface brightness and equivalent widths are separately shown in tables C.5 and C.6.

a : (degree).

Table C.5: (Continued)

Field	Field center		Surface brightness (photon s^{-1} cm^{-2} sr^{-1})				
	l_{II}	b_{II}	Mg	Si	S	Ar	Ca
GC0	−0.013	0.004	2.49±0.49	6.69±0.64	13.5±1.14	6.40±1.08	3.42±1.07
GC1	0.330	0.217	1.34±0.47	4.68±0.50	4.75±0.70	1.55±0.58	0.92±0.56
GC2	0.514	−0.082	3.07±0.34	2.94±0.36	1.50±0.57	0.00(<0.54)	0.15±0.57
GC3	0.170	−0.293	2.45±0.55	3.52±0.47	8.37±0.77	3.85±0.67	1.76±0.63
GC4	−0.169	−0.499	0.76±0.50	1.96±0.58	2.81±0.72	0.98±0.64	0.56(<1.13)
GC5	−0.265	−0.147	2.51±0.59	4.58±0.53	7.57±0.83	2.30±0.74	1.08±0.73
GC6	−0.534	0.094	2.38±0.34	1.46±0.33	1.40±0.54	0.47(<0.99)	0.00(<0.30)
GC7	−0.193	0.308	2.03±0.64	2.30±0.44	2.62±0.58	0.90±0.51	0.13(<0.60)
GP−2	−1.810	−0.080	1.37±0.41	1.45±0.36	1.14±0.44	1.03±0.42	0.40±0.38
GP−3	−2.310	−0.076	1.35±0.81	0.75±0.30	1.00±0.38	0.73±0.33	0.43±0.29
GP−4	−2.813	−0.075	0.00(<0.23)	0.63±0.34	0.50±0.37	0.46±0.34	0.12(<0.43)
GP−5	−3.304	0.007	0.70±0.45	0.85±0.44	1.17±0.53	0.56±0.46	0.06(<0.48)
GP−6	−3.805	0.006	0.27(<0.60)	1.07±0.32	1.34±0.43	0.88±0.34	0.00(<0.15)
GP−7	−4.305	0.006	1.97±0.86	1.48±0.44	1.16±0.43	0.86±0.38	0.37±0.32
GP−8	−4.803	0.007	1.53(<2.83)	1.63±0.56	2.31±0.73	1.10±0.62	0.74±0.53
GP−12	−6.805	0.006	0.00(<0.26)	1.01±0.37	0.00(<0.34)	0.33(<0.72)	0.30(<0.66)
GP−13	−7.307	0.006	1.11±0.33	1.68±0.34	1.21±0.40	0.15(<0.47)	0.00(<0.26)
GP−14	−7.802	0.008	1.32±0.31	0.61±0.26	0.00(<0.21)	0.33±0.29	0.00(<0.21)
GP+1	0.998	0.003	0.00(<0.35)	2.86±0.79	0.30(<1.10)	0.41(<1.11)	0.00(<0.48)
GP+2	1.495	0.009	0.00(<0.55)	2.02±0.59	0.29(<0.93)	1.20±0.59	0.20(<0.73)
GP+6	3.495	0.007	0.93±0.48	1.28±0.41	1.43±0.42	0.54±0.34	0.27(<0.57)
GP+7	3.994	0.010	0.49±0.38	0.76±0.34	0.89±0.41	0.54±0.32	0.42±0.29
GB−1	0.006	−0.841	2.68±0.58	3.90±0.38	2.88±0.44	1.04±0.36	0.00(<0.23)
GB−2	0.005	−1.258	3.18±0.58	4.97±0.41	2.12±0.38	0.59±0.29	0.17(<0.41)
GB−3	0.007	−1.674	3.85±0.57	3.52±0.39	0.87±0.32	0.07(<0.30)	0.00(<0.15)
GB−4	−0.007	−2.070	3.70±0.48	1.93±0.29	0.38±0.23	0.22±0.17	0.10(<0.24)
GB−5	−0.006	−2.486	3.30±0.48	1.57±0.28	0.37±0.28	0.00(<0.06)	0.00(<0.06)
GB−6	−0.004	−2.898	1.59±0.43	0.82±0.27	0.28±0.23	0.29±0.19	0.08(<0.23)
GB−7	−0.010	−4.990	1.23±0.30	0.47±0.16	0.03(<0.17)	0.00(<0.09)	0.07(<0.18)
GB−8	−0.006	−6.989	1.22±0.29	0.50±0.18	0.20±0.16	0.00(<0.08)	0.08(<0.19)
GB−9	0.007	−9.006	0.00(<0.28)	0.05±0.13	0.20±0.11	0.18±0.09	0.10±0.08

Table C.6: (Continued)

Field	Field center		Equivalent width(eV)					χ^2/d.o.f
	l_{II}	b_{II}	Mg	Si	S	Ar	Ca	
GC0	−0.013	0.004	431±148	163±17	196±18	85±15	48±15	76.59/68
GC1	0.330	0.217	144±113	219±26	197±31	71±27	47±29	69.57/68
GC2	0.514	−0.082	1673±373	283±37	70±28	0±22	7(<32)	116.1/70
GC3	0.170	−0.293	366±144	125±18	227±24	107±21	56±21	78.63/68
GC4	−0.169	−0.499	40±27	65±20	97±26	39±26	29(<59)	65.54/70
GC5	−0.265	−0.147	328±215	126±15	152±18	46±15	24±16	79.63/68
GC6	−0.534	0.094	824±118	95±22	59±23	18±21	0(<13)	93.05/70
GC7	−0.193	0.308	264±145	104±22	108±26	44±26	8(<36)	59.71/69
GP−2	−1.810	−0.080	250±101	138±38	105±44	108±47	50(<100)	67.33/68
GP−3	−2.310	−0.076	247±217	74±32	106±43	92±44	74±52	62.86/68
GP−4	−2.813	−0.075	0(<26)	65±37	60±48	67±53	22±59	79.98/70
GP−5	−3.304	0.007	114±80	111±65	167±87	100±91	13(<103)	77.23/70
GP−6	−3.805	0.006	35(<88)	124±42	178±61	143±59	0(<32)	59.82/70
GP−7	−4.305	0.006	109±41	104±35	117±47	110±52	69±62	61.89/69
GP−8	−4.803	0.007	114(<1072)	51±19	75±25	44±26	44±32	57.82/68
GP−12	−6.805	0.006	0(<22)	67±26	0(<25)	30(<66)	35±43	71.68/72
GP−13	−7.307	0.006	197±64	197±48	151±57	25(<80)	0(<61)	56.42/70
GP−14	−7.802	0.008	482±122	128±59	0(<45)	79±74	0(<63)	87.76/70
GP+1	0.998	0.003	0(<8)	60±17	8(<30)	15±26	0(<24)	88.94/72
GP+2	1.495	0.009	0(<16)	51±16	9(<28)	46±23	9(<34)	65.08/71
GP+6	3.495	0.007	74±42	124±46	206±69	103±72	67(<146)	88.14/70
GP+7	3.994	0.010	47±38	78±38	113±57	97±60	94±69	38.39/69
GB−1	0.006	−0.841	88±24	114±12	102±16	46±16	0(<14)	72.47/69
GB−2	0.005	−1.258	57±11	149±14	97±18	41±21	17(<42)	74.51/70
GB−3	0.007	−1.674	82±13	136±17	59±23	8(<35)	0(<30)	91.22/70
GB−4	−0.007	−2.070	95±13	95±15	33±20	34±27	27(<54)	86.46/70
GB−5	−0.006	−2.486	115±18	100±19	39±28	0(<11)	0(<16)	75.72/70
GB−6	−0.004	−2.898	68±20	64±24	38±34	62±43	31(<89)	70.41/69
GB−7	−0.010	−4.990	136±39	110±45	12(<77)	0(<78)	122(<287)	44.64/71
GB−8	−0.006	−6.989	280±110	232±121	187±173	0(<154)	276(<657)	60.15/70
GB−9	0.007	−9.006	0(<44)	23±66	292±187	991±551	2189(<4031)	77.43/73

Appendix D

Radiation Damage of SIS

D.1 RDD Defect

In this section, we introduce the RDD defect by citing Dotani et al. (1997 [17]). They discovered the RDD defect. The RDD defect causes further degradation of the CCD performance in addition to the non-uniform CTI. The RDD results from the increase of the dark current due to the radiation damage. The increase of the dark current is very different from pixel to pixel, although the dark current does not show a large variation on a global scale within a chip. On-board data processing assigns only a single dark level for 16x16 pixels due to a limited computer resources. Thus, the pixel-to-pixel variations of the dark current cannot be corrected for on board. This excess variation is called the RDD (Residual Dark Distribution) and causes various defects on the SIS performance, such as a degradation of the energy resolution, a decrease of the detection-efficiency, and so on. They found that these SIS degradations are partially corrected using the RDD map created by the FRAME-mode data.

D.2 Selection Criteria of the Frame Data

According to the suggestion by Dotani et al. (1997 [17]), we chose the frame data in the following criteria.

- The present author has the access right to the frame data.

- Since the RDD defect depends on the passing time from the launch, the frame data are obtained in a few months (if possible in less than one month from the observations).
- Since the RDD defect will depend on the temperature of the SIS detector, the frame data are obtained under the similar temperature of the observations if possible.
- Since the RDD defect also depends on the exposure per one frame, the frame data is obtained using the same mode during the observation.
- Since the RDD defect also depends on the CCD chip of SIS, the frame data of the same chip is available.

The used frame maps were listed in tables D.1 & D.2.

Table D.1: Number of the frame data for the RDD correction, which was applied to the data in the '97 spring observations obtained with the 4CCD-mode.

Chip ID[a]	Main targets			Total
	ρ Oph core	Sgr A	Sgr A offset	
S0C0	1	1	0	2
S0C1	1	2	0	3
S0C2	1	2	0	3
S0C3	1	2	0	3
S1C0	1	1	1	3
S1C1	1	1	1	3
S1C2	1	1	1	3
S1C3	1	1	1	3

a: SmCn, where n is the number of the SIS detector and m is the chip number.

D.3 Result of the RDD Correction

After we created the RDD maps from these frame data, we corrected the RDD defect for the '97-spring Sgr-A observation according to the method given by Dotani et al. (1997 [17]).

D.3.1 Grade & Spectra

In the '97 spring Sgr A observation, we used the 4CCD-FAINT-mode(0123/2301) for bit-rate HIGH and 1CCD-FAINT(2222/0000) for MEDIUM, respectively. Therefore, we can directly compare the performance of each mode if we used the S0C0 & S1C2 chips, which covered the Galactic center Sgr A. After we subtracted hot & flickering pixels from these two chips, we made histograms of the event rates for each grade, which were plotted in figure D.1. We created the spectra using only the events with 0–4 grade, which were shown in figure D.2. As shown in figure D.1 & D.2, both the event rates for each grade and the spectra with 0–4 grades had no essential difference between the RDD-non-corrected and RDD-corrected data obtained with the 1CCD-mode. We confirmed the RDD defect does not contribute both to the energy resolution and to the decrease of the detection-efficiency in the case of 1CCD-mode. On the contrary, the 4CCD-mode data show the different grade distribution from the 1CCD-mode (figure D.1). We could correct only a part of the grade distribution even if RDD-corrected. Therefore the total count rates of the 4CCD-mode spectra given in figure D.2 show the smaller value than that of 1CCD-mode(only about 80% level of that for the 1CCD-mode if RDD-corrected). The Kα-lines from helium-like ions from silicon(1.86 keV) and sulphur(2.45 keV) atoms in the RDD-corrected 4CCD-mode spectra seem to become shaper than that in RDD-non-corrected but duller than that with the 1CCD-mode. Even if we performed the RDD correction, we confirmed that the energy resolution of the 4CCD-mode become worse than that of the 1CCD-mode. We could not completely restore the degradation of the energy resolution and the decrease of the detection-efficiency in the case of 4CCD-mode.

D.4 Systematic Errors of the Detection-Efficiency

In this thesis, we used the SIS data including the standard grade values of 0, 2, 3 & 4. In order to research the decrease of the SIS detection-efficiency obtained with the 4CCD-mode, we again extracted the spectra with the grade values of 0, 2, 3 & 4. The count rates detected in the energy range of 1–10 keV were summarized in table D.3. As is shown in table D.3, the count rates with the 1CCD-mode have null-dependence of the RDD correction. On the contrary, the count rates with the

4CCD-mode have the values of 40% and 70% of the 1CCD-mode before and after the RDD correction, respectively. For comparison, we simultaneously listed in table D.3 the count rate detected by S0C1 & S1C3 with the GP−1 observation (defined in section 3) performed in '93 autumn, which is corresponding to only about 0.6 year later since the *ASCA* launch. The GP−1 observations were performed with the 4CCD-mode(0123/0123) for bit-rate HIGH and 1CCD(1111/3333) for MEDIUM, which is the similar mode-assignment of the '97 spring Sgr A observations. Because the bright X-ray source "the Great Annihilator 1E 1740.7−2942" is locate near the center of S0C1 & S1C3, the count rates of S0C1 & S1C3 in the GP−1 observations show the high count rate, which exceeded 1 counts s^{-1} $chip^{-1}$. In the GP−1 observations, each count rate with the 4CCD-mode before the RDD correction has nearly the same value($\sim$95%) of the 1CCD-mode.

As the 1CCD-mode data have null-dependence of the RDD correction, we assumed that the detection-efficiency of the 1CCD-mode had not been changed yet. Under this assumption, the ratio of the count rates(4CCD/1CCD) represented the decreasing rate of the detection-efficiency for the 4CCD-mode data. The ratios of the count rates(4CCD/1CCD) were given in table D.3 and plotted in figure D.3. We found that the decreasing rate $c(t)$ of the detection-efficiency for the 4CCD-mode data were roughly interpolated by a linear function of the passing year t from the *ASCA* launch given by,

$$c(t) = 1 - 0.14 \times (\frac{t}{1\mathrm{yr}}). \tag{D.1}$$

We concluded that the detection-efficiency for the 4CCD-mode before the RDD correction has the systematic decrease roughly given by equation D.1. The systematic decrease for the RDD-corrected 4CCD-mode data was inferred to be about half for the RDD-non-corrected. Note that all the errors of the flux given in the text of this thesis did not include this systematic decrease of the detection-efficiency. For the data obtained with the 4CCD-BRIGHT-mode data, we could restore only the energy resolution with the RDD correction. Since we can not correct the grade distribution, the systematic decrease was defined by the equation D.1 both before and after the RDD correction.

Table D.2: Same as table D.1 but for 1CCD-mode.

Chip ID.	Main target
	Sgr A
S0C0	4
S1C2	4

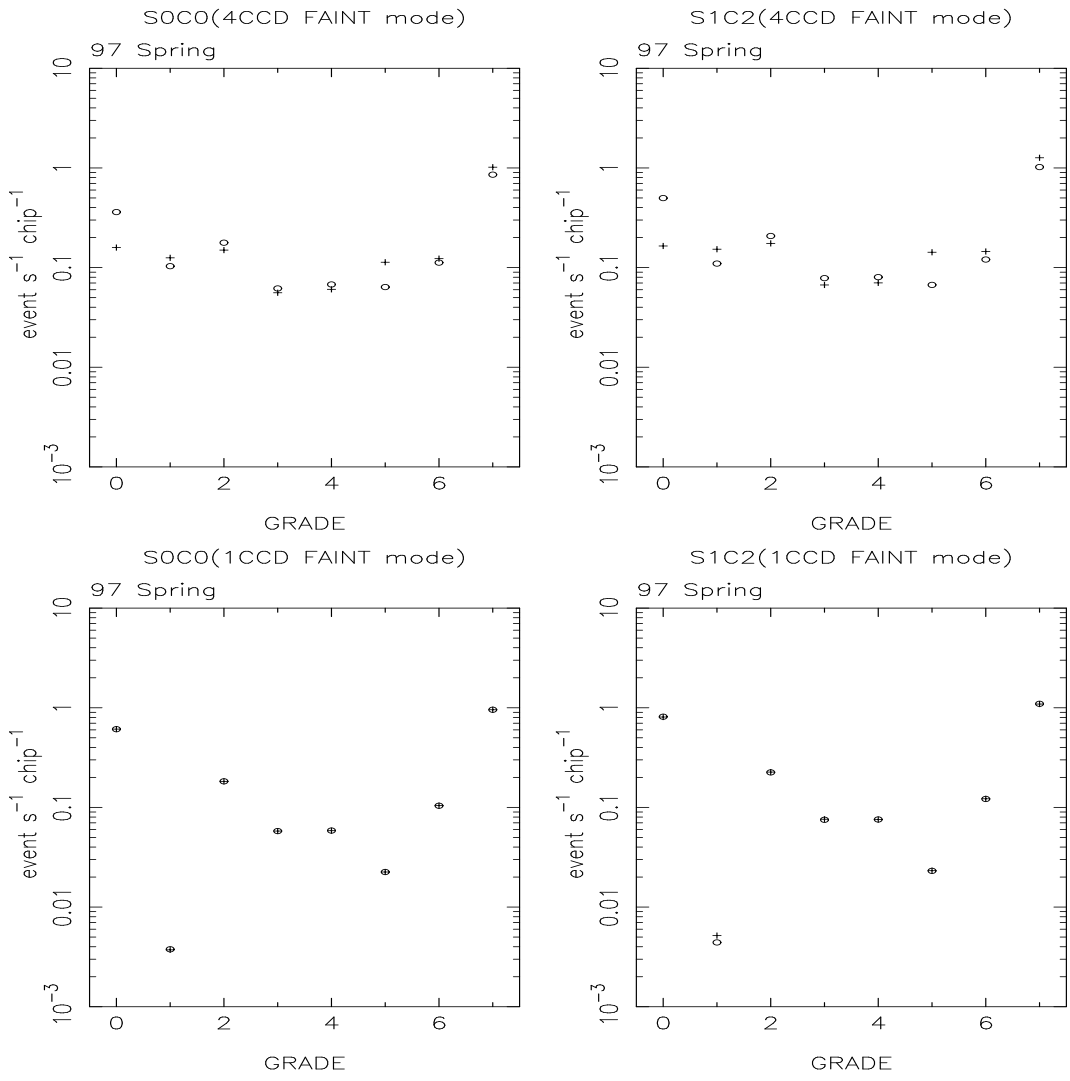

Figure D.1: Grade distributions of the SIS event rate in the '97 spring Sgr A observation. The event rate for 4 and 1CCD-mode are shown in top and bottom panels, respectively. Left and right panels are extracted from the data of S0C0 and S1C2 chips, respectively. The circle and cross give the cases for the corrected and non-corrected events for RDD, respectively.

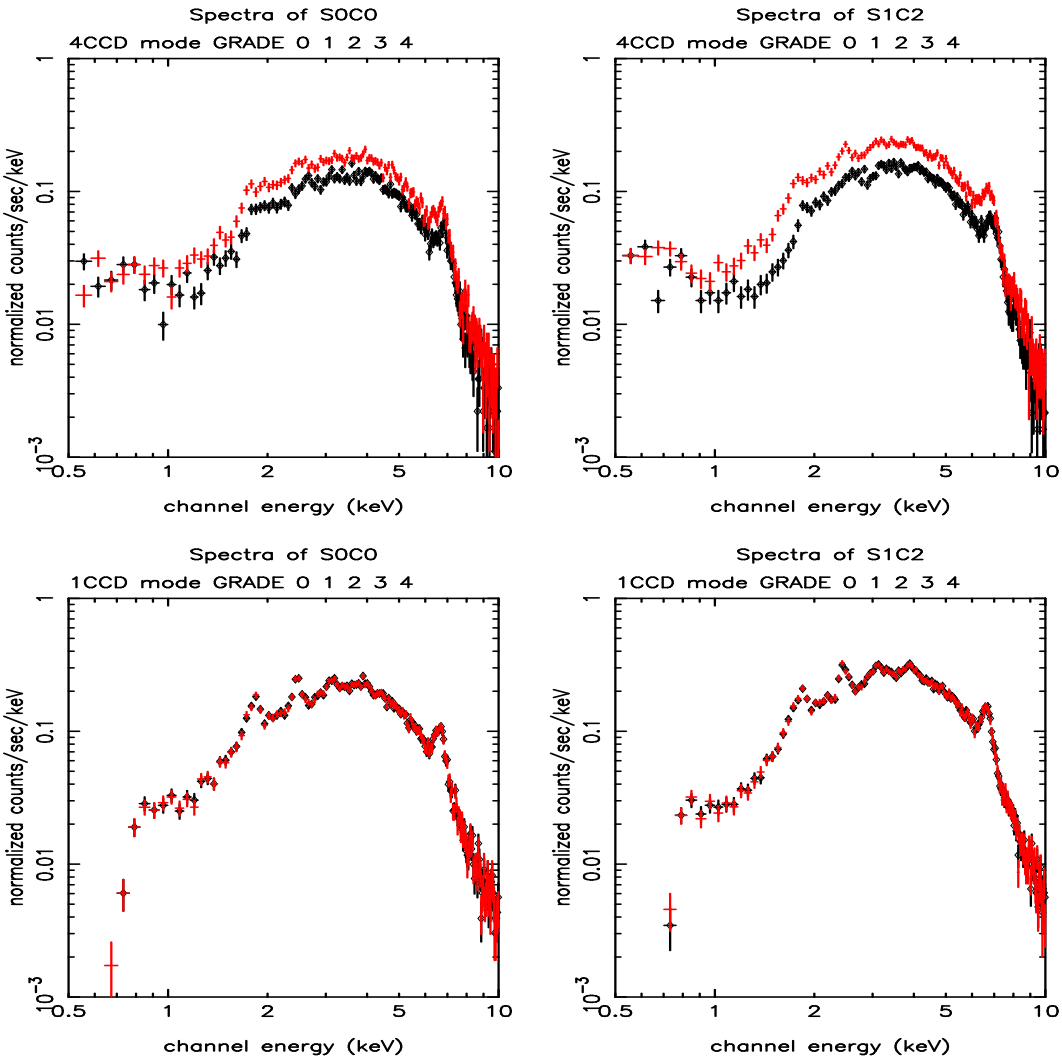

Figure D.2: SIS spectra obtained in the '97 Sgr A observation. The spectra obtained with 4 and 1CCD-mode are shown in top and bottom panels, respectively. Left and right panels are extracted from the data of S0C0 and S1C2 chips, respectively. In each panel, we simultaneously plot the spectra with(faint black) and without(black) the RDD correction. Error bars are 1σ.

Table D.3: SIS count rates (counts s^{-1} $chip^{-1}$) detected in the 1–10 keV band.

	1CCD-mode		4CCD-mode	
	RDD-corrected	RDD-non-corrected	RDD-corrected	RDD-non-corrected
	———'93 autumn ———			
S0C1	–	1.60	–	1.59(0.97)
S1C3	–	1.32	–	1.21(0.92)
	———'97 spring ———			
S0C0	0.89(1.00)	0.89	0.64(0.72)	0.41(0.46)
S1C2	1.17(1.00)	1.17	0.83(0.71)	0.46(0.40)

The value given in parenthesis shows the ratio normalized by the count rate for the RDD-non-corrected 1CCD-mode data.

Figure D.3: Plot of the ratio of the count rate(4CCD/1CCD)

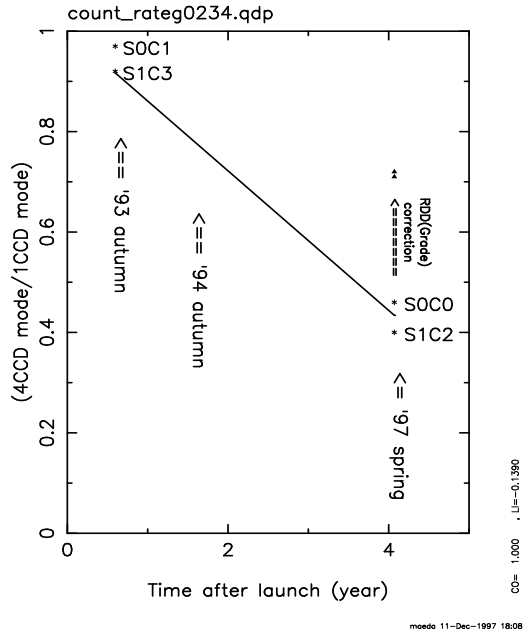

The ratio is listed in table D.3. The asterisk and triangle are the ratios for the RDD-non-corrected and RDD-corrected, respectively. The solid line shows the linear function which interpolates the ratios for the RDD-non-corrected.

Appendix E

Radio Map of the Molecular Clouds

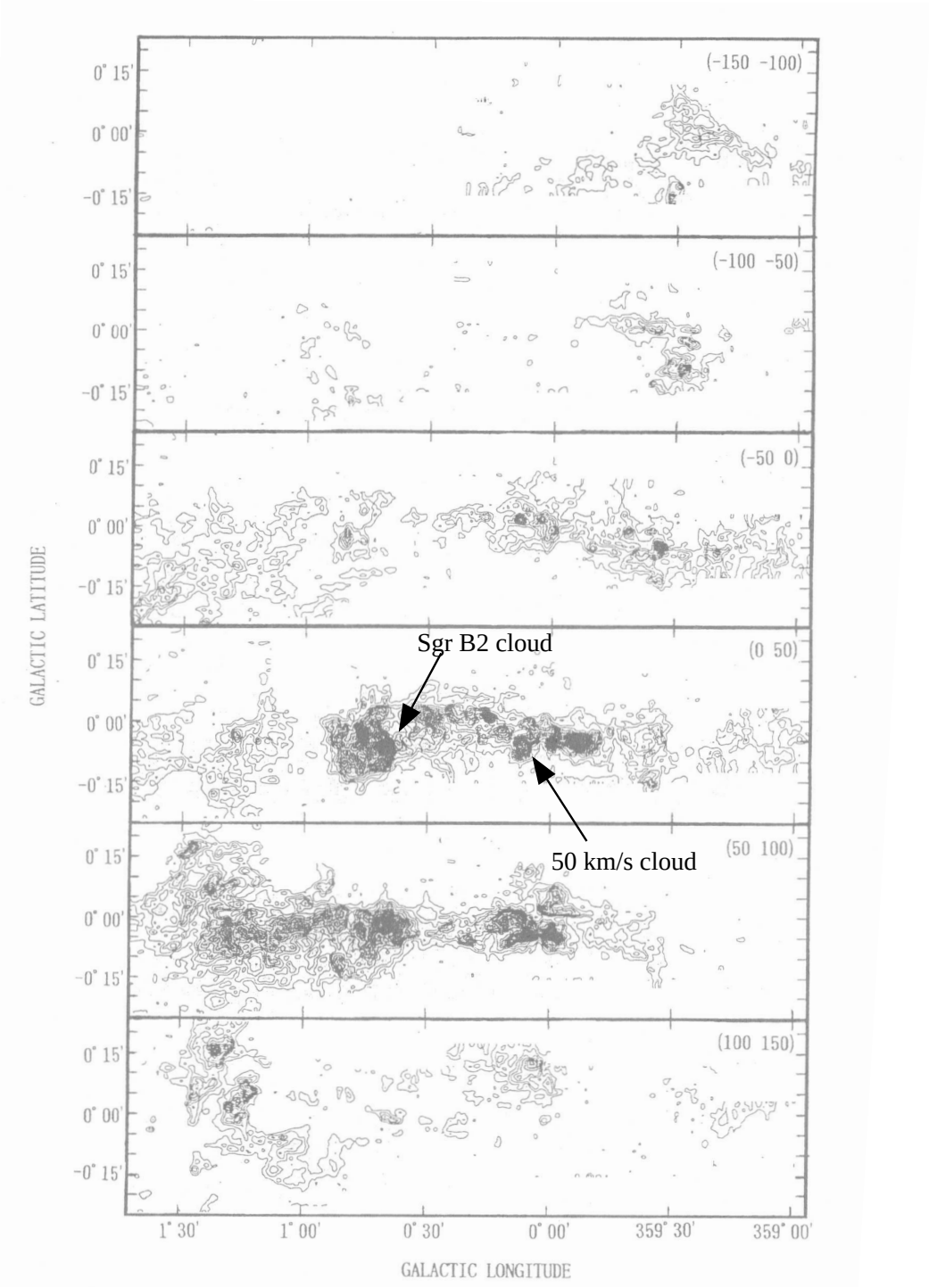

Figure E.1: Velocity-averaged maps of CS $J = 1 \rightarrow 0$ emission between -150 and 150 km s^{-1}, which cover a $150' \times 40'$ ($l \times b$) region in the Galactic Center (Tsuboi et al. 1997 [105]). The averages are taken over 50 km s^{-1} bins. The contour interval is linear. CS $J = 1 \rightarrow 0$ is a good tracer of high density molecular clouds with the typical hydrogen density $n_{\rm H} \geq 10^4$ cm^{-3}. The typical excitation temperature of CS is 30–80 K.

Bibliography

[1] Allen, C. W., 1973, Astrophysical Quantities 3rd edition (London: Athlone)

[2] Allen, W. H., et al. 1993, Physical Review D, 48, 466

[3] Anders, E., & Grevesse, N. 1989, Geochimica et Cosmochimica Acta, 53, 197

[4] Augusteijn, T., Greiner, J., Kouvekitou, C., Vanparadijs, J., Lidman, C., Blanco, P., Fishman, G. J., Briggs, M. S., Kommers, J., et al., 1997, ApJ, 486, 1013

[5] Awaki H. 1990, Doctor Thesis, Nagoya University

[6] Bally, J., Stark, A. A., Wilson, R. W. 1988, ApJ, 324, 223.

[7] Beckert, T., Duschl, W. J., Mezger, P. G., & Zylka, R., 1996, A&A, 307, 450

[8] Becklin, E. E., & Neugebauer, G., 1968, ApJ, 151, 145

[9] Becklin, E. E., Gatley, I., & Werner, M. W. 1982, ApJ 258, 134

[10] Blitz, L., Binney, J., Lo, K. Y., Bally, J., & Ho, P. P., 1993, Nature, 361, 417

[11] Branduardi G., Ives J. C., Sanford P. W., Brinkman, A. C., Maraschi L. 1976, MNRAS 175, 47

[12] Brown, R. L., & Liszt, H. S., 1984, Ann. Rev. Astron. Astrophys. 22, 223

[13] Buckley, J. H., et al., 1997, astro-ph/9706178

[14] Burke, B. E., Mountain, R. W., Daniels, P. J., Dolat, V. S. , & Cooper, M. J. 1994, IEEE Trans. Nucl. Sci. 41, 375

[15] Cruddacs, R. G., Fritz, G., Shulman, S., Friedman, H., McKee, J., & Johnson, M. 1978, ApJL 222, L95

[16] Davies R. D., Walsh D., Browne I. W. A., Edwards M. R., Noble R. G. 1976, Nature 261, 476

[17] Dotani, T., Yamashita, A., Ezuka, H., Takahashi, K., Crew, G., Mukai, K., & the SIS team 1997, *ASCA* news No. 5, 14

[18] Eckart, A., Genzel, R., Hofmann, R., Sams, B. J., & Tacconi-Garman, L., E., 1993, ApJ, 407L, 77

[19] Eckart, A., & Genzel, R. 1997, MNRAS 284, 576

[20] Elvis, M., Maccacaro, T., Wilson, A. S., Ward, M. J., Penston, M. V., et al. 1978, MNRAS, 183, 129

[21] Eyles C. J., Skinner G. K., Willmore A. P., Rosenberg F. D. 1975, Nature 257, 291

[22] Fujimoto, R., & Ishida, M. 1997, ApJ, 474, 774

[23] Garmire, G. P., & Nugent, J. J. 1981, BAAS, 13, 786

[24] Genzel, R., Hollenbach, D., & Towns, C. H. 1994, Rep. Prog. Phys. 57, 417

[25] Genzel, R., & Towns, C. H., 1987, Ann. Rev. Astron. Astrophys. 25, 377

[26] Grandi, P., Tagliaferri, G., Giommi, P., Barr, P., & Paslumbo, G., 1992 ApJS, 82, 93

[27] Hayakawa, S. 1970, Progr. Theor. Phys. 43, 1224

[28] Hayakawa, S., Kato, T., Nagase, F., Yamashita, K., Murakami, T., & Tanaka, Y. 1977, ApJ, 213, L109

[29] Hasinger, G., Burg, R., Giacconi, R., Hartner, G., Schmidt, M., Trümper,J., & Zamorani, G. 1993, A&A, 275, 1

[30] Hayashi, I., 1997, Doctor Thesis, Kyoto University

[31] Hellier, C., Mukai, K., Ishida, M., & Fujimoto, R., 1996, MNRAS, 280, 877

[32] Hughes, J. P., Hayashi, I., Helfand, D., Hwang, U., Itoh, M., Kirsher, R., Koyama, K., Markert, T., Tsunemi, H., & Woo, J., 1995, ApJ 444, L81

[33] van de Hulst H.C. 1957, Light Scattering by Small Particles (Dover, New York) p85

[34] Hunter, S. D., Bertsch, D. L., Catelli, J. R., Dame, T. M., Digel, S. W., Dingus, B. L., Esposito, J. A., Fichtel, C. E., Hartman, R. C., et al., 1997, ApJ, 481, 205

[35] Ikebe, Y., 1995, Ph.D. Thesis, University of Tokyo

[36] Inoue. H., 1984, Space Sci. Rev. 40, 317

[37] Ishida, M., 1992, Ph.D. Thesis, University of Tokyo

[38] Ishida, M., Matsuzaki, K., Fujimoto, R., Mukai, K., & Osborne, J., 1997, MNRAS, 287, 651

[39] Ishisaki, Y. 1996, Ph.D. Thesis, University of Tokyo

[40] Ishisaki, Y., Ueda, Y., Kubo, H. Ikebe, Y., Makishima, K., & the GIS team 1996, *ASCA* news No. 4, 25

[41] Janesick, J., Elliott, T., and Garmire, G., 1985, Proc. X-ray Instrumentation in Astronomy, SPIE 597, 364

[42] Johnson, W. N., III, & Haymes, R. C., 1973, ApJ, 184, 103

[43] Kaneda, H. 1997, Ph.D. Thesis, University of Tokyo

[44] Kaneda, H., Makishima, K., Yamauchi, S., Koyama, K., Matsuzaki, K., & Yamasaki, N. Y. 1997, ApJ 491, 638

[45] Kawai, N., Fenimore, E. E., Middleditch, J., Cruddace, R. G., Fritz G. G., Snyder W. A., Ulmer M. P. 1988, ApJ 330, 130

[46] Kellogg, E., Gursky, H., Murray, S., Tananbaum, H., & Giacconi, R. 1971, ApJL 169, L99

[47] Kennea J. A., & Skinner G. K. 1996, PASJ 48, L117

[48] Kinugasa, K. et al. 1997a, PASJ, submitted, (G352.7–0.1)

[49] Kinugasa, K. 1998, Ph.D. Thesis, University of Osaka

[50] Koyama, K., Makishima, K., Tanaka, Y., & Tsunemi, H. 1986, PASJ 38, 121

[51] Koyama, K. Awaki, H. Kunieda, H. Takano, S. Tawara, Y. Yamauchi, S. Hatsukade, I., & Nagase, F. 1989, Nature 339, 603

[52] Koyama, K., Maeda, Y., Sonobe, T., Takeshima, T., Tanaka, Y., Yamauchi, S. 1996, PASJ 48, 249(Paper I)

[53] Koyama, K., Kinugasa, K., Matsuzaki, K., Sugizaki, M., Nishiuchi, M., Torii, K., Yamauchi, S., & Aschenvbach, B. 1997, PASJ, 49, L7

[54] Lacy, J. H., Achtermann, J. M., & Serabyn,E. 1991, ApJ 380L, L71

[55] Lewin, W. H. G, Hoffman, J. A., Doty, J., Hearn, D. R., Clark, G. W., Jernigan, J. G., Li, F. K., McClintock, J.E., Richardson, J. 1976, MNRAS 177, 83

[56] Leventhal, M., MacCallum, C. J., Huters, A. F.. & Stang, P. D., 1980, ApJ, 240, 338

[57] Lindqvist, M., Sandqvist, A., Winnberg, A., Johansson, L. E. B., Nyman, L. -Å. 1995, A&AS, 113, 257

[58] Lis D. C., & Carlstrom J. E. 1994, ApJ, 424, 189

[59] Lo, K. Y., & Claussen, M. J. 1983, Nature 306, 647

[60] Long, K. S., Helfand, D. J., & Grabelsky, D. A., 1981, ApJ 248, 925

[61] Maeda, Y., Koyama, K., & *ASCA* team, 1994, in the proceedings of "New Horizon of X-Ray Astronomy" eds, F. Makino and T. Ohashi (University Academy Press, Tokyo), p497

[62] Maeda, Y., Koyama, K., Sakano, M., Takeshima, Y., & Yamauchi, S. 1996, PASJ 48, 417(Paper II)

[63] Makishima, K., Tashiro, M., Ebisawa, K., Ezawa, H., Fukazawa, Y., Gunji, S., Hirayama, M., Idesawa, E., Ikebe, Y. et al., 1996, PASJ, 48, 171

[64] Masai, K. 1984, A&AS, 98, 367

[65] Markevitch, M., Sunyaev, R., A., & Pavlinsky, M., 1993, Nature, 364, 40

[66] Marshall, N., Warwick, R. S., & Pounds, K. A., 1981, MNRAS, 194, 987

[67] Matsuzaki, K. 1998, Ph.D. Thesis, University of Tokyo

[68] Mewe, R., Gronenschild, E. H. B. M., & Van den Oord, G. H. J. 1985. A&AS, 62, 197

[69] Mitsuda, K., Inoue, H., Koyama, K., Makishima, K., Matsuoka, M., Ogawara, Y., Shibazaki, N., Suzuki, K., Tanaka, Y., & Hirano, T. 1984 PASJ, 36, 741

[70] Mitsuda, K., Inoue, H., Nakamura, N., & Tanaka, Y. 1989, PASJ, 41, 97

[71] Mitsuda K., Takeshima T., Kii T., & Kawai N. 1990, ApJ 353, 480

[72] Morris, M., Polish, N., Zuckerman, B., & Kaifu, N., 1983, AJ 88, 1228

[73] Morris, M. 1994, in Ringberg Conference "The Nuclei of Normal Galaxies", Kluwer Academic Publishers (the Netherlands), eds Genzel and Harris, 185-198

[74] Morris,M., & Serabyn,E. 1996, Ann. Rev. Astron. Astrophys. 34, 645

[75] Morrison, R., & McCammon, D. 1983, ApJ, 270, 119

[76] Mukai, K., Ishida, M., & Osborne, J. P., 1994, PASJ 46, L87

[77] Murakami, H. et al. 1998, private communication

[78] Nishiuchi, M., Asai, K., Dotani, T., Kouveliotou, C., Koyama, K., Inoue, I., Maeda, Y., Mitsuda, K. et al. 1997 in Proc. IAU Symposium 188, The Hot Universe, ed K. Koyama, M. Itoh, S. Kitamoto, in press

[79] Ohashi, T., Ebisawa, K., Fukazawa, Y., Hiyoshi, K., Horii, M., Ikebe, Y., Ikeda, H., Inoue, H. et al. 1996, PASJ 48, 157

[80] Oka, T., Hasegawa, T., Hayashi, M., Handa, T., & Sakamoto, S., 1997, ApJ, submitted

[81] Oort, J. H., 1977, Ann. Rev. Astron. Astrophys. 15, 295

[82] Paczyński B. 1971, ARA&A 9, 183

[83] Park,S., Finley, J. P., Snowden, S. L., & Dame, T. M. 1997, ApJ, 476, L77

[84] Phinney, E. S. 1989, IAU colloquium 136 " The Center of the Galaxy" eds M. Morris, 543

[85] Predehl, P., & Trümper, T. 1994, A&A 290, L29

[86] Predehl P., & Schmitt J. H. M. M. 1995, A&A 293, 889

[87] Proctor, R. J., Skinner, G. K., & Willmore, A. P. 1978, MNRAS, 185, 745

[88] Purcell, W. R., Grabelsky, D. A., Ulmer, M. P., Johnson, W. N., Kinzer, R. L., Kurfess, J. D., Strickman, M. S., & Jung, G. V., 1993, ApJ, 413L, 85

[89] Purcell, W. R., Cheng, L. -X., Dixon, D. D., Kinzer, R. L., Kurfess, J. D., Leventhal, M., Saunders, M. A., Skibo, J. G., Smith, D. M., & Tueller, J., 1997, ApJ, 491, 725

[90] Raymond, J. C., & Smith, B. W., 1977, ApJS, 35, 419

[91] Sakano, M., Nishiuchi, M., Maeda, Y., Koyama, K., & Yokogawa, J. 1997, in Proc. IAU Symposium 184, The Central Regions of the Galaxy and Galaxies", ed. Y.Sofue, in press

[92] Serlemitsos, P. J., Jolota, L., Soong, Y., Kunieda, H., Tawara, Y., Tsusaka, Y., Suzuki, H., Sakima, Y. et al. 1995 PASJ, 47, 105

[93] Schöenfelder, V., in Proc. IAU Symposium 188, The Hot Universe, ed K. Koyama, M. Itoh, S. Kitamoto, in press

[94] Skinner G. K., Willmore A. P., Eyles C. J., Bertram D., Church M. J., Harper P. K. S., Herring J. R. H., Peden J. C. M. et al. 1987, Nature, 330, 544

[95] Snowden, S. L., Freyberg, M. J., Plucinsky, P. P., Schmitt, J. H. M. M., Trüemper, J., Voges, W., Egger, R., McCammon, D., & Sanders, W. T. 1995, ApJ, 454, 643

[96] Snowden, S. L., Egger, R., Freyberg, M. J., McCammon, D., Plucinsky, P. P., Sanders, W. T., Schmitt, J. H. M. M., Trüemper, J., & Voges, W. 1997, ApJ, 485, 125

[97] Stark, A. A., & Bania, T. M., 1986, ApJ 306, L17

[98] Sugizaki, M., Nagase, F., Torii, K., Kinugasa, K., Asanuma, T., Matsuzaki, K., Koyama, K., & Yamauchi, S. 1997, PASJ, 49, L25

[99] Sutton, E. C., Danchi, W. C., Jaminet, P. A., & Masson, C. R. 1990, ApJ, 348, 503

[100] Syunyaev R., Pavlinskii M., Gil'fanov M., Churazov.E., Grebenev S., Markevich M., Dekhanov I. Yamburenko N., & Babalyan G. 1991, *Sov.Astron.* 17, L42

[101] Sunyaev, R., A., Markevitch, M., & Pavlinsky, M., 1993, ApJ, 407, 606

[102] Tanaka, Y., Inoue, H., & Holt, S. S. 1994, PASJ 46, L37

[103] Torii, K. et al. 1997, IAU Circ.6678; Kinugasa, K. et al. 1997b, ApJ, 495, L435 (152 sec pulsar)

[104] Torii, K. 1998, Ph.D. Thesis, University of Osaka

[105] Tsuboi, M., Handa, T., & Ukita, N. 1997, ApJS, submitted

[106] Ueno, S., 1997, Doctor Thesis, Kyoto University

[107] Yamasaki, N. Y., Ohashi, T., Takahara, F., Yamauchi, S., Koyama, K., Kamae, T., Kaneda, H., Makishima, K., Sekimoto, Y., et al., 1997, ApJ, 481, 821

[108] Yamauchi, S., Kawada, M., Koyama, K., Kunieda, H., Tawara, Y., & Hatsukade, I. 1990, ApJ, 365, 532

[109] Yamauchi, & Koyama 1993, ApJ, 404, 620

[110] Yamauchi, & Koyama 1995, PASJ, 47, 439

[111] Warwick, R. S., Turner, M. J. L., Watson, M. G., & Willingale, R, 1985, Nature, 317, 218

[112] Watson, M. G., Willingale, R., Grindlay, J.E., & Hertz, P. 1981, ApJ, 250, 142

[113] Whyte, C. A., & Eggleton, P. 1980, MNRAS 190, 801

[114] Wilson, A. M., Carppenter G. F., Eyles C. J., Skinner G. K., & Willmore, A. P. 1977, ApJL 215, L111

[115] Worrall, D. M., Marshall, F. E., Boldt, E. A., & Swank, J. H. 1982, ApJ, 255, 111

[116] Wright, MCH., Genzel, R., Güsten, R., & Jaffe, D. T. 1987, 1987, AIP Conf. Proc. No.155, The Galactic Center. New York, ed Backer DC., 133P

Acknowledgments

I would like to appreciate Prof. K. Koyama for his continuous guidance and encouragement throughout 5 years of my graduate course.

I am deeply grateful to Mr. T. Sonobe and Prof. Y. Tanaka. I owed very much to them for the data analysis and discussion.

I would express my thanks to Prof. S. Yamauchi and all the members of the Galactic plane survey project team for their valuable comments and encouragement. Drs. K. Gendreau and H. Kaneda kindly supplied us the useful data of the *ASCA* observation.

I also thank Dr. T. Oka, Prof's T. Hasegawa , M. Tsuboi and their Co-investigators for their useful discussions and for providing me with the radio data before publication.

I wish to thank all the members of the cosmic-ray laboratory in Kyoto University for their encouragement, technical advice and discussions. Also, I would like to thank Drs. H. Awaki, and T. Tsuru for their guidance and encouragement. Dr. Ozaki and Mr. Sakano kindly prepared several figures and softwares.

I thank all the members of the *ASCA* team for their support of this study. All the observational data were obtained by the members of the *ASCA* team. I am indebted to the staff of the *ASCA* Guest Observers Facility. My analysis was mainly performed using the FTOOLS and XANADU packages, which were provided by GSFC/NASA. This research has made by using the HEASARC database, SkyView service (GSFC/NASA), the NASA Astrophysics Data System abstract service and the IPAC/NASA extra galactic database (NED). I am also grateful to the XRT-*ASCA* simulation team who has enabled me to create the appropriate response file utilized in the present thesis. Some figures were created using the IDL & DISPLAY45 software packages.

I was financially supported by the Japan Society for the Promotion of Science. I was also financially supported by the Hayakawa Satio Foundation to attend the Galactic Center Workshop in Chile. I also thank Dr. K. Ebisawa, his family, Drs. Y. Ogasaka and T. Takeshima for the hospitality of my visit to GSFC/NASA in U.S.A..

Plate I: Mosaic X-ray images on the Galactic Center observed with the SIS detector. (right) An X-ray image in the 0.7–10 keV band with the peak at the Galactic Center (Sgr A). (left) An narrow-band image the fluorescent iron line at 6.4 keV; a northern bright spot (upper-left) is located near the giant molecular cloud (Sgr B), and another (middle) near the Radio Arc appears to be associated with a new molecular clouds. The solid lines represent the Galactic plane.

Plate II: The 6.4 keV line image near Sgr B2, overlaid with the CH_3CN lines ([6]).

Plate III: GIS mosaic images in the 0.7–3 keV(left) and 3–10 keV(right) bands of the Chris-cross mapping. The color levels are logarithmically spaced. All the images were smoothed with the Gaussian function of 1 $\sigma = 3$ pixels ≈ 0.75 arcmin. Correlation of the non-uniform efficiency over the detector field was made on the images. The non-X-ray background (NXB) was subtracted while the cosmic X-ray background (CXB) is included (see the details for NXB and CXB are described in appendix B).